ISSN 2671-7255 (print)
ISSN 2671-7263 (online)

http://www.jees.kr

JEES

Journal of Electromagnetic Engineering and Science

Volume 20, No. 3
July 2020

KIEES

Journal of Electromagnetic Engineering and Science Volume 20, No.3 July 2020 KIEES

JEES
Journal of
Electromagnetic Engineering
and Science

Jul. 2020
Vol. 20 No. 3

ISSN 2671-7255 (Print)
ISSN 2671-7263 (Online)

Aims and Scope

The Journal of Electromagnetic Engineering and Science (**JEES**) is an official English-language journal of the Korean Institute of Electromagnetic and Science (**KIEES**). This journal was launched in 2001 and has been published quarterly since 2003. It is currently registered with the National Research Foundation of Korea and also indexed in Scopus, CrossRef, EBSCO, DOI/Crossref, Google Scholar, and Web of Science Core Collection as Science Citation Index Expanded (SCIE) journal. The objective of **JEES** is to publish academic as well as industrial research results and discoveries in electromagnetic engineering and science. The particular scope of the journal includes electromagnetic field theory and its applications; high frequency components, circuits, and systems; antennas; electromagnetic wave environments; and relevant industrial developments. In addition to the regular stream of contributed papers, the journal occasionally publishes special issues on specific topics of current interest, to promote a focused coverage of the selected topics. In addition, **JEES** regularly posts invited review papers by leading researchers in the relevant fields, which will provide an overview of various subjects from their own perspectives. The editors of **JEES** are aware of the importance of rapid publication for the delivery of new research results to its readers with minimum delay, and fully recognize the need for a short turnaround time. Manuscripts submitted to **JEES** take about 3–5 months from the initial submission to publication. This rapid process applies to all three types of manuscripts that **JEES** publishes: regular papers, letters, and invited papers. The publication of submitted manuscripts is subject to blind peer review, and the final decision by the Editor-in-Chief is regularly made based on three reviews from experts in the relevant area. This journal actively promotes research in electromagnetic wave-related engineering and sciences, and its ultimate aim is to benefit the global electromagnetic engineering and science community.

Subscription Information

JEES is published quarterly in January, April, July, and October. Full text PDF files are available at the official website (http://www.jees.kr).

The annual subscription rates for this journal are USD 230 for institutional members, USD 55 for regular members, USD 37 for associate members, and USD 28 for student members.

Published by
The Korean Institute of
Electromagnetic Engineering and Science

#706 Totoo Valley, 217 Saechang-ro, Yongsan-gu, Seoul, 04376, Korea
Tel : +82-2-337-9666 / 332-9665
Fax : +82-2-6390-7550
http://www.kiees.or.kr
E-mail : kees@kiees.or.kr

Printed July 25, 2020
Published July 31, 2020

Printed by
Guhmok Publishing Company
Tel : +82-2-2277-3324
Fax : +82-2-2277-3390
E-mail : guhmok@guhmok.com

KOFST
This journal was supported by the Korean Federation of Science and Technology Societies Grant funded by the Korean Government (Ministry of Education).

JEES
Journal of
Electromagnetic Engineering
and Science

Jul. 2020
Vol. 20 No. 3

ISSN 2671-7255 (Print)
ISSN 2671-7263 (Online)

REGULAR PAPERS

This journal was supported by the Korean Federation of Science and Technology Societies Grant funded by the Korean Government (Ministry of Education).

JOURNAL OF ELECTROMAGNETIC ENGINEERING AND SCIENCE, VOL. 20, NO. 3, 159~163, JUL. 2020

https://doi.org/10.26866/jees.2020.20.3.159
ISSN 2671-7263 (Online) · ISSN 2671-7255 (Print)

A Mode-Matching Solution for TE-Backscattering from an Arbitrary 2D Rectangular Groove in a PEC

Mehdi Bozorgi*

Abstract

In this paper, the simple yet effective mode-matching technique is utilized to compute TE-backscattering from a 2D filled rectangular groove in an infinite perfect electric conductor (PEC). The tangential magnetic fields inside and outside of the groove are represented as the sums of infinite series of cosine harmonics (half-range Fourier cosine series). By applying the continuity of the tangential magnetic field, these modes are matched on the groove to obtain the series coefficients by solving a system of linear equations. For this purpose, some oscillatory logarithmic singular integrals involving Hankel and trigonometric functions are solved numerically, starting by removing the logarithmic singularity via integration by parts. In the following, the new well-behaved highly oscillatory integrals are computed using efficient methods, and several comparisons are made to demonstrate the validity and ability of the presented procedure.

Key Words: Highly Oscillatory Singular Integral, Modal Expansion, TE-Backscattering, 2D Filled Rectangular Groove.

I. INTRODUCTION

Electromagnetic wave scattering from a groove has received attention due to its broad applicability and easy realization in radar cross-section and non-destructive testing applications [1, 2]. An analytical solution for a narrow groove is given in the literature [3], and the finite element and hybrid numerical techniques have been investigated to simulate scattering from an arbitrary shape groove [4, 5]. To study scattering from a large crack, a Fourier transform was proposed in [6], and, for narrow and wide rectangular cracks, a complex direct integral equation solver (DIES) was proposed to solve a singular integral equation by a collocation method based on Chebyshev polynomials [2]. From the base modal technique, other techniques were developed to efficiently calculate electromagnetic waves backscattered from grooves [7–10], which considered some simplifications and assumptions to avoid solving complicated singular integrals. Morgan and Schwering [7] used the physical optic approximation to model equivalent electric current distributions on the groove and considered two synthetic waveguide walls in upper space; this creates significant error for narrow grooves but is somewhat accurate for wide apertures. As reported in [8], the constructed integral equation in the spectral domain is converted to a system of linear algebraic equations to compute the unknown Rayleigh function. To improve the computational efficiency of this technique, a model-based parameter estimation technique based on a curve-fitting model was employed. In [9], by applying Fourier transform techniques to a 2D groove, the singularity of the constructed integral could be analytically removed and an exact expression for the far-field scattering obtained by stationary phase approximation. Cho [10] also employed the overlapping T-block method to obtain an accurate closed-form expression for far-field scattered waves.

In this paper, an approach based on the usual mode-mat-

Manuscript received May 11, 2019 ; Revised June 16, 2019 ; Accepted September 11, 2019. (ID No. 20190511-033J)
Department of Electrical Engineering, Faculty of Engineering, Arak University, Arak, Iran.
*Corresponding Author: Mehdi Bozorgi (e-mail: M-Bozorgi@araku.ac.ir)

ching methodology is developed, without the limiting assumptions made in [7] and away from the complex expressions presented in [2]. It is used to obtain the equivalent magnetic current on the groove, which can create the scattered fields. At first, the fields are represented as a sum of infinite harmonic modes in the open rectangular cavity. Applying the equivalence principle, an unknown equivalent magnetic current is simulated over the groove, which is then calculated. Mode-by-mode field matching across the groove then leads to an infinite system of linear equations. While allowing sufficient accuracy, the infinite sums are truncated to obtain the expansion coefficients. To expand the tangential magnetic field in the upper half-space outside the groove, a highly oscillatory singular integral should be solved. There are some quadrature techniques to calculate singular logarithmic integrals [11, 12], most of which assume that the singular integral contains a logarithmic singular part and functions with slow variations. However, if a singular integral includes trigonometric and Bessel functions simultaneously with large arguments, the number of quadrature nodes must increase significantly and, therefore, the simulation time increases immensely. For this reason, advanced techniques have been developed to compute a highly oscillatory integral quickly. Here, in the first stage, the singularity is eliminated through integration by parts; the remaining oscillatory integrals can then be calculated quickly with sufficient precision using the efficient methods in [13–15]. This solution is valid for narrow and wide grooves, with the advantages of accuracy and acceptable time consumption, particularly for the wide grooves.

II. FORMULATION

Assume a TE electromagnetic plane wave,

$$H_z^i = \vec{z}e^{jk_1((x-\frac{W}{2})\cos\varphi_0 + y\sin\varphi_0)} \quad \varphi_0 \in (0,\pi). \tag{1}$$

where k_1 is the free space propagation constant and φ_0 is the incidence angle. As shown in Fig. 1, the wave illuminates a dielectric-filled 2D rectangular groove with ε_2 and μ_2.

The tangential magnetic field inside the groove is expanded by cosine basis functions to satisfy Maxwell's equations [7].

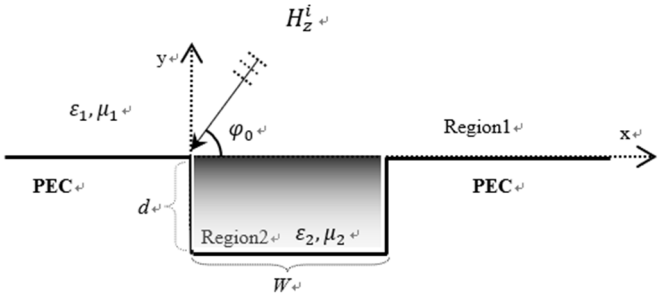

Fig. 1. The geometry of the rectangular groove and TE-mode incident wave.

Thus, the x-component of the electric field inside the groove can be obtained as follows:

$$E_x(x,y) = \frac{\partial H_z(x,y)}{\partial y} = \sum_{p=0}^{\infty} A_p k_p \cos\left(\frac{p\pi x}{W}\right) \times \sin\left(k_p(y+d)\right) \tag{2}$$

where $k_p = \sqrt{k_2^2 - \left(\frac{p\pi}{w}\right)^2}$ and A_p are unknown series coefficients that should be calculated. By invoking the equivalence principle on the groove, the magnetic current $\vec{M}$ at $y = 0$ is calculated to be

$$\vec{M}(x) = \left[E_x(x)\vec{x} + E_y(x)\vec{y}\right] \times \vec{y} = E_x(x)\vec{z} = \vec{z}\sum_{p=0}^{\infty} A_p k_p \cos\left(\frac{p\pi x}{W}\right)\sin(k_p d) \tag{3}$$

Considering Green's functions in two regions (Region1, free space; Region2, groove), the tangential magnetic fields resulting from the magnetic current $M_z(x)$ are obtained as follows [2]:

$$H_z^{Region1}(x) = -\frac{k_1 y_1}{2}\sum_{p=0}^{\infty} A_p k_p \sin(k_p d) \times \int_0^W \cos\left(\frac{p\pi x'}{W}\right) H_0^{(2)}(k_1\ |x-x'\ |)dx' \tag{4}$$

and

$$H_z^{Region2}(x) = \frac{jk_2 y_2}{W}\sum_{p=0}^{\infty} A_p k_p \sin(k_p d) \times \sum_{n=0}^{\infty} \frac{\varepsilon_n}{k_n \tan(k_n d)} \cos\left(\frac{n\pi x}{W}\right)\int_0^W \cos\left(\frac{n\pi x'}{W}\right)\cos\left(\frac{p\pi x'}{W}\right)dx' \tag{5}$$

where y_1 and y_2 are the intrinsic admittances for Region1 and Region2, respectively; $k_n = \sqrt{k_2^2 - (\frac{n\pi}{w})^2}$; $H_0^{(2)}(.)$ is the zeroth-order Hankel function of the second kind; and $\varepsilon_n = 1$ if $n = 0$ and $\varepsilon_n = 2$ otherwise. By imposing the continuity of the tangential magnetic field on both sides of the groove $(y = 0)$, we have

$$2e^{jk_1\left(x-\frac{W}{2}\right)\cos\varphi_0} + H_z^{Region1}(x) = H_z^{Region2}(x). \tag{6}$$

Substituting (4)–(5) into (6) and simplifying, we construct the following equation:

$$2e^{jk_1\left(x-\frac{W}{2}\right)\cos\varphi_0} - \frac{k_1 y_1}{2}\sum_{p=0}^{\infty} A_p k_p \sin(k_p d)\ \ Q_p(x) = -jk_2 y_2 \sum_{p=0}^{\infty} A_p \cos(k_p d)\cos\left(\frac{p\pi x}{W}\right) \tag{7}$$

where the function $Q_p(x)$ is defined as

$$Q_p(x) = \int_0^W \cos\ \left(\frac{p\pi x'}{W}\right) H_0^{(2)}(k_1\ |x-x'\ |)dx'. \tag{8}$$

In Eq. (7), to utilize the mode-matching technique, the function $Q_p(x)$ and the function $\exp\left(jk_1\left(x-\frac{W}{2}\right)\right)\cos\varphi_0$ should

be expanded using half-range Fourier cosine series, i.e.,

$$Q_p(x) = \sum_{k=0}^{\infty} q_{pk} \cos\left(\frac{k\pi x}{W}\right) \tag{9}$$

and

$$2e^{jk_1\left(x-\frac{W}{2}\right)\cos\varphi_0} = \sum_{p=0}^{\infty} b_p \cos\left(\frac{p\pi x}{W}\right). \tag{10}$$

The coefficients b_p in (10) can be easily calculated analytically as

$$b_p = \varepsilon_p \alpha \frac{(-1)^p e^{\alpha/2} - e^{-\alpha/2}}{(p\pi)^2 + \alpha^2} \tag{11}$$

where $\alpha = jk_1 W \cos\varphi_0$ and ε_p is like ε_n in (5). The coefficients q_{pk} in (9) can also be computed as

$$q_{pk} = \frac{\varepsilon_p}{W} \int_0^W \int_0^W \cos\left(\frac{k\pi x}{W}\right) \cos\left(\frac{p\pi x'}{W}\right) \times H_0^{(2)}(k_1 |x - x'|) dx' dx \tag{12}$$

The integral in (12)—the so-called highly oscillatory singular integral—cannot be computed easily. It should, however, be noted that, when the values of *k*, *p*, and *W* increase, we need a large number of quadrature nodes to maintain accuracy, and the computing time increases enormously. Some rapid methods have been reported in [13–15] to calculate these integrals numerically. To solve the integral specified in (12), let us first focus on the following highly oscillatory integral:

$$q_{pk} = \frac{\varepsilon_p}{W} \int_0^W \cos\left(\frac{k\pi x}{W}\right) Q_p(x) dx \tag{13}$$

Introducing the variable $\xi = \frac{2}{W}x - 1$ in interval [-1, 1], the integral (13) is split up into two cosine and sine integrals:

$$q_{pk} = \begin{cases} \frac{\varepsilon_p}{2}(-1)^{\frac{k}{2}} \int_{-1}^{1} \cos\left(\frac{k\pi}{2}\xi\right) Q_p(\xi) d\xi & k: even \\ \frac{\varepsilon_p}{2}(-1)^{\frac{k+1}{2}} \int_{-1}^{1} \sin\left(\frac{k\pi}{2}\xi\right) Q_p(\xi) d\xi & k: odd \end{cases} \tag{14}$$

Here, we assume $Q_p(\xi)$ is a function with a removable singularity part. A quadrature-based Legendre polynomials technique is used to evaluate the highly oscillatory integrals in (14) [13]. Therefore, the above integrals can be calculated via the following integral:

$$\int_{-1}^{1} e^{\frac{jk\pi}{2}\xi} Q_p(\xi) d\xi = \sum_{m=0}^{M} j^m \left[\frac{(2m+1)^2}{m}\right]^{\frac{1}{2}} \times J_{m+\frac{1}{2}}\left(\frac{k\pi}{2}\right) \sum_{s=0}^{M} w_s P_m(\xi_s) Q_p(\xi_s) \tag{15}$$

where w_s and ξ_s are weights and abscissas (defined as the roots of the Legendre polynomial), respectively, of the $(M+1)$ point Gauss-Legendre rule [13], and $J_{m+\frac{1}{2}}(.)$ and $P_m(.)$ are a Bessel function and Legendre polynomial of degree *m*, respectively. Now, by presenting $\xi' = \frac{2}{W}x' - 1$, integral $Q_p(\xi_s)$ in (15) can be arranged in the form

$$Q_p(\xi_s) = \frac{W}{2} \int_{-1}^{1} \cos\left(\frac{p\pi}{2}(1+\xi')\right) \times H_0^{(2)}\left(\frac{k_1 W}{2}|\xi_s - \xi'|\right) d\xi' \tag{16}$$

The integral in (16) contains the highly oscillatory and logarithmic functions (Henkel and cosine function). In computing $Q_p(\xi_s)$, regular approaches generally do not lead to a proper result. At this point, to eliminate the logarithmic singularity of the zeroth-order Hankel function of the second kind at $\xi' = \xi_s$, direct integration by parts is suggested. The integral in (16) is written in the following form:

$$\begin{aligned} Q_p(\xi_s) = &-\frac{W}{2} \times \\ &\left[(\xi_s - \xi')\cos\left(\frac{p\pi}{2}(1+\xi')\right) H_0^{(2)}\left(\frac{k_1 W}{2}|\xi_s - \xi'|\right)\right]_{-1}^{1} \\ &-\frac{p\pi W}{4} \int_{-1}^{1} \sin\left(\frac{p\pi}{2}(1+\xi')\right)(\xi_s - \xi') \\ &\times H_0^{(2)}\left(\frac{k_1 W}{2}|\xi_s - \xi'|\right) d\xi' + \frac{k_1 W^2}{4} \times \\ &\int_{-1}^{1} \cos\left(\frac{p\pi}{2}(1+\xi')\right) \frac{(\xi_s - \xi')^2}{|\xi_s - \xi'|} H_1^{(2)}\left(\frac{k_1 W}{2}|\xi_s - \xi'|\right) d\xi' \end{aligned} \tag{17}$$

As seen in (17), at $\xi' = \xi_s$, the resulting integrals are not singular, but rather still consist of highly oscillatory functions. They can be computed in the same manner proposed for the integrals in (14). We can also use the rapid numerical methods developed for integrals containing Bessel and trigonometric functions [14, 15]. After calculating q_{pk} and substituting (9)–(10) into (7), Eq. (7) can finally be rearranged as follows:

$$\begin{aligned} &\sum_{p=0}^{\infty} b_p \cos\left(\frac{p\pi x}{W}\right) \\ &\quad - \sum_{k=0}^{\infty}\sum_{p=0}^{\infty} A_p \frac{k_1 y_1}{2} q_{pk} k_p \sin(k_p d) \cos\left(\frac{k\pi x}{W}\right) \\ &\quad = -\sum_{p=0}^{\infty} A_p j k_2 y_2 \cos(k_p d) \cos\left(\frac{p\pi x}{W}\right) \end{aligned} \tag{18}$$

While allowing sufficient accuracy, infinite sums in (18) are truncated at $k = K$ and $p = P$. Taking $K = P$, we obtain the following linear system of equations:

$$\begin{bmatrix} b_0 \\ b_1 \\ \vdots \\ b_p \end{bmatrix} = \begin{bmatrix} M_{00} & M_{01} & \cdots & M_{0P} \\ M_{10} & M_{11} & & M_{1P} \\ \vdots & & \ddots & \vdots \\ M_{P0} & M_{P1} & \cdots & M_{PP} \end{bmatrix} \begin{bmatrix} A_0 \\ A_1 \\ \vdots \\ A_p \end{bmatrix} \tag{19}$$

where the elements M_{pk} are given by

$$M_{pk} = \begin{cases} \frac{k_1 y_1}{2} q_{pk} k_p \sin(k_p d) - j k_2 y_2 \cos(k_p d) & , k = p \\ \frac{k_1 y_1}{2} q_{pk} k_p \sin(k_p d) & , k \neq p \end{cases} \tag{20}$$

The unknown expansion coefficients A_p are now obtained by a simple matrix inversion operation. As we know the magnetic current distribution on the aperture, the backscattered fields and the echo width are estimated as in [2]:

$$H_z^s = -\vec{z}\frac{e^{-jk_0\rho}}{\sqrt{\rho}}e^{j\frac{\pi}{4}}\frac{k_1 y_1}{2} \times \sqrt{\frac{2}{\pi k_1}}\int_0^W M_z(x')e^{jk_1 x'\cos\varphi_0}\,dx' \quad (21)$$

and

$$\sigma_{TE}^{2D} = \lim_{\rho\to\infty} 2\pi\rho\,\frac{|H_z^s|^2}{|H_z^i|^2} \quad (22)$$

III. Results

Using the above derivations, some comparisons are made to show the effectiveness and accuracy of the suggested procedure. Fig. 2 shows the equivalent magnetic current distribution over a groove with specifications define. As shown in Fig. 2, the obtained results are in good agreement with both DIES [2] and FEKO simulator—based methods of moments. In this case, for the same accuracy, the infinite series in Eq. (18) is truncated at $K = P = 15$, while we should use $N = 30$ (Chebyshev polynomials degree N) in the DIES method [2]. To simulate a 2D groove using FEKO software, we use an infinite 3D rectangular trough. To obtain the equivalent magnetic current, the x-component of the near electric field on the middle of the groove ($y = 0$) should be computed. We also utilize a one-dimension periodic boundary condition to simulate the infinite length of the groove. We set frequency $f = 29{,}979 \times 10^4$ and $\lambda = 1$ to define the required variables and the mesh sizes in wavelength. To provide a highly efficient solution, the object surfaces partially mesh through two local mesh sizes. The local mesh size on the ground plane is set at 0.3λ, while the minimum values of the triangle edge lengths for the groove surfaces are set to $0.05d\lambda$ and $0.05W\lambda$. Fig. 3 shows a comparison between several numerical techniques for predicting backscatter echo width in a wide range of groove widths. Here, a slight amount of loss was added to the filling dielectric $\varepsilon_2 = \varepsilon_0(2 - 0.01j), \mu_2 = \mu_0(1 - 0.01j)$ to remove

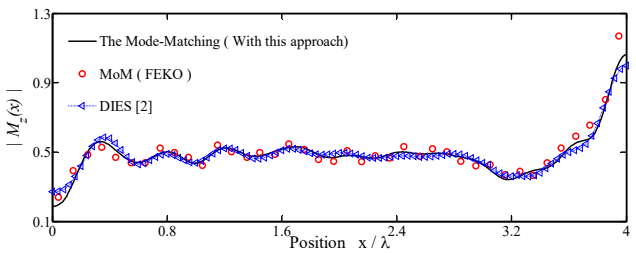

Fig. 2. The magnetic current density for a filled groove ($\varepsilon_{r2} = 2.5 - j0.2$, $\mu_{r2} = 1.8 - j0.1$, and $\varepsilon_1 = \varepsilon_0$, $\mu_1 = \mu_0$) of $W = 4\lambda$ and $d = 0.5\lambda$ at $\varphi_0 = 45°$.

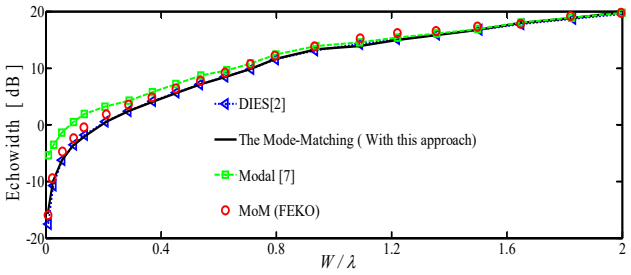

Fig. 3. TE-backscattering echo width versus the groove width for $d = 0.2\lambda$, $\varphi_0 = 90°$, $\varepsilon_1 = \varepsilon_0$, $\varepsilon_2 = 2\varepsilon_0 - 0.01i$, and $\mu_1 = \mu_2 = \mu_0$.

the resonances appearing in the echo width graph reported in [10], which happens when $\cos(k_p d)$ in (18) approaches zero.

From Fig. 3, it can be deduced that the suggested procedure is accurate for both wide and narrow grooves, whereas the modal method in [7] is only appropriate for wide grooves. Using the physical optics approximation and replacing the upper half-space with a waveguide in [7] creates many errors for narrow grooves. To compare the time consumed, we measured the simulation time of each method (for a filled groove with the specification shown below, Fig. 3). The results are presented in Table 1.

By examining the results in Table 1, we can say that, for wide grooves, the modal method presented in [7] is faster than all numerical methods. When the groove width increases, the equivalent magnetic current on the aperture becomes oscillatory. In the DIES method, we need higher-degree Chebyshev polynomials and more quadrature nodes to estimate the rough magnetic current, but it can be simulated by a lower number of harmonic cosine modes. This is why the simulation time of the proposed solution is lower than the DIES method for $W = 4\lambda$. In the previous example, we also employed the technique mentioned in [11] to calculate the double integral in Eq. (12). In this case, the simulation times for $W = 0.1\lambda$, $W = \lambda$, and $W = 4\lambda$ were measured as 5.21, 9.87, and 73.22 seconds, respectively. A comparison of the above results with the results in Table 1 demonstrates that using advanced numerical integration methods for wide grooves improves time efficiency.

Briefly, the proposed procedure uses the mode-matching

Table 1. Simulation time (in second) of the several methods measured for three groove widths

Size	FEKO[a]	Modal [7]	DIES [2]	Mode-matching (this approach)
$W = 0.1\lambda$	8	Not accurate	1.56	5.23
$W = \lambda$	25	5.07	4.58	9.14
$W = 4\lambda$	52	7.07	31.20	20.36

[a]Measured in minute.

method as seen in [7] without any restrictive assumptions. It is accurate for every groove size with acceptable time efficiency.

IV. Conclusion

In this work, a simple solution is suggested to calculate TE-backscattering from an arbitrary rectangular groove. Without limiting assumptions and complex mathematical concepts, the investigated method utilizes a numerical mode-matching methodology to obtain the equivalent magnetic current on the groove. A mode-by-mode substitution from the field expansion outside and inside of the groove for each pair of mode expansion coefficients leads to a linear system of equations. For this purpose, an efficient integration method is used to numerically calculate the constructed, highly oscillatory singular integral. The results are in good agreement with other numerical methods. By evaluating the above results, it can be concluded that this approach is accurate for cases of both narrow and wide grooves. The simulation time for several techniques was measured, and the proposed approach has acceptable time efficiency, especially for wide grooves.

References

[1] W. H. Choi, H. K. Jang, J. H. Shin, T. H., Song, J. K. Kim, and C. G. Kim, "Monostatic RCS reduction by gap-fill with epoxy/MWCNT in groove pattern," *Journal of the Korean Institute of Electromagnetic and Science*, vol. 12, no. 1, pp. 101-106, 2012.

[2] M. Bozorgi, A. Tavakoli, G. Monegato, S. H. H. Sadeghi, and R. Moini, "Backscattering from a two dimensional rectangular crack using FIE," *IEEE Transactions on Antennas And Propagation*, vol. 58, no. 2, pp. 552-564, 2009.

[3] K. Barkeshli and J. L. Volakis, "Scattering from narrow rectangular filled grooves," *IEEE Transactions on Antennas and Propagation*, vol. 39, no. 6, pp. 804-810, 1991.

[4] T. Van and A. W. Wood, "Finite element analysis of electromagnetic scattering from a cavity," *IEEE Transactions on Antennas and Propagation*, vol. 51, no. 1, pp. 130-137, 2003.

[5] S. S. Bindiganavale and J. L. Volakis, "A hybrid FE-FMM technique for electromagnetic scattering," *IEEE Transactions on Antennas and Propagation*, vol. 45, no. 1, pp. 180-181, 1997.

[6] G. Bao and W. Sun, "A fast algorithm for the electromagnetic scattering from a large cavity," *SIAM Journal on Scientific Computing*, vol. 27, no. 2, pp. 553-574, 2005.

[7] M. A. Morgan and F. K. Schwering, "Mode expansion solution for scattering by a material filled rectangular groove," *Progress in Electromagnetics Research*, vol. 18, pp. 1-17, 1998.

[8] D. C. Skigin, V. V. Veremey, and R. Mittra, "Superdirective radiation from finite gratings of rectangular grooves," *IEEE Transactions on Antennas and Propagation*, vol. 47, no. 2, pp. 376-383, 1999.

[9] T. J. Park, H. J. Eom, and K. Yoshitomi, "An analysis of transverse electric scattering from a rectangular channel in a conducting plane," *Radio Science*, vol. 28, no. 5, pp. 663-673, 1993.

[10] Y. H. Cho, "TM plane-wave scattering from finite rectangular grooves in a conducting plane using overlapping T-block method," *IEEE Transactions on Antennas and Propagation*, vol. 54, no. 2, pp. 746-749, 2006.

[11] J. A. Crow, "Quadrature of integrands with a logarithmic singularity," *Mathematics of Computation*, vol. 60, pp. 297-301, 1993.

[12] M. Carley, "Numerical quadratures for singular and hypersingular integrals in boundary element methods," *SIAM Journal on Scientific Computing*, vol. 29, no. 3, pp. 1207-1216, 2007.

[13] S. Xiang and W. Gui, "On generalized quadrature rules for fast oscillatory integrals," *Applied Mathematics and Computation*, vol. 197, no. 1, pp. 60-75, 2008.

[14] G. V. Milovanovic and M. P. Stanic, "Numerical integration of highly oscillating functions," in *Analytic Number Theory, Approximation Theory, and Special Functions*. New York, NY: Springer, 2014, pp. 613-649.

[15] G. V. Milovanovic, "Computing integrals of highly oscillatory special functions using complex integration methods and gaussian quadratures," *Dolomites Research Notes on Approximation*, vol. 10(special issue), pp. 79-96, 2017.

Mehdi Bozorgi

was born in Isfahan, Iran, on September 4, 1977. In 2018, he joined Arak University, Arak, Iran, where he is currently an Assistant Professor in the Department of Electrical Engineering. His current research interests include the scattering of electromagnetic waves, electromagnetic nondestructive testing, and optics.

JOURNAL OF ELECTROMAGNETIC ENGINEERING AND SCIENCE, VOL. 20, NO. 3, 164~168, JUL. 2020

https://doi.org/10.26866/jees.2020.20.3.164
ISSN 2671-7263 (Online) · ISSN 2671-7255 (Print)

Electrically and Frequency-Tunable Printed Inverted-F Antenna with a Perturbed Parasitic Element

Yoon-Seon Choi · Ji-Hun Hong · Jong-Myung Woo*

Abstract

This study designed an electrically and frequency-tunable printed inverted-F antenna (PIFA) with a perturbed parasitic element between the antenna and the ground plane. The resonant frequency of the proposed antenna can be changed via the short- and open-circuit operation of the parasitic element. This operation is activated using an electrical switch, which in this case is a PIN diode with an inductor and a resistor. The antenna was designed on the basis of the principles of the perturbation method, which enables control over resonant frequencies through modifications to the volume of a metal cavity. Meandered gaps were incorporated into the parasitic element for the independent operation of each PIN diode switch. The size of the PIFA's radiator is 4.8×10 mm^2, and the tunable resonant frequency at the –10 dB bandwidth is 340 MHz (17.3%).

Key Words: Printed Inverted-F Antenna, Perturbation Theory, Parasitic Elements, Frequency-Tunable Antenna.

I. Introduction

Recent developments in mobile communication technology gave rise to a bandwidth requirement of 300 MHz (11.7%) for the 3.5 GHz frequency band used for 5G technology. To meet this requirement, developers created many multiple-input, multiple-output antennas, which are mainly used in mobile communication [1, 2]. These antennas, however, need additional space for multiple ports, making it difficult to satisfy the required bandwidth with a single antenna port in a given space. This problem was overcome through the development of frequency-tunable antennas. A variant of these innovations is the two-dimensional printed inverted-F antenna (PIFA), which is widely used in electronic devices as a communication antenna [3]. It can be easily fabricated through modern printing technology and fitted into a limited space because of its low-profile structure. Another example is the frequency-tunable planar inverted-F antenna equipped with a capacitor [4–7] (see also [8]). The capacitor is located between the main radiator and a parasitic element to vary resonant frequencies, after which capacitance is modified. This design means that the space occupied by a complex feeding structure expands because the antenna is directly connected to the radiator and parasitic element. An important consideration, however, is that using different capacitance values can contribute to antenna losses.

Previously developed frequency-reconfigurable antennas are equipped with yttrium-iron-garnet elements, and their resonant frequencies are tuned by changing the magnetic field, which is controlled by a DC bias [9]. The drawback to this design is that it reduces an antenna's radiation efficiency and increases fabrication costs.

In the present study, a frequency-tunable PIFA (FTPIFA)

Manuscript received June 25, 2019 ; Revised August 5, 2019 ; Accepted March 5, 2020. (ID No. 20190625-084J)
Department of Radio and Information Communication Engineering, Chungnam National University, Daejeon, Korea.
*Corresponding Author: Jong-Myung Woo (e-mail: jmwoo@cnu.ac.kr)

comprising a perturbed parasitic element was designed, with mobile devices as reference. The size of the antenna was reduced on the basis of perturbation theory [10–12] to the radiation element. The resonant frequency of the PIFA can be tuned by changing the volume of the electric and magnetic fields.

II. Antenna Design

Fig. 1(a) and (b) show the designed PIFA with a parasitic element between the radiator and the ground plane. It was printed on a 0.8-mm thick, 50 × 100 mm² FR-4 (ε_r = 4.3, tanδ = 0.025) substrate. The size of the antenna's radiator is 24.8 × 10 mm². Because the position where a short circuit occurs ("short position" hereafter) can be tuned from switches #1 to #5 by using a copper strip, the central frequency (2,045 MHz) is based on the shorted state of switch #3.

Fig. 1(c) illustrates the new antenna structure used to change the short-circuit structure of the copper strip (Fig. 1(b)). A PIN diode (SMP1345-079LF) located between the parasitic element and the ground plane functions as a switch. It was redesigned by adding meandered gaps to the parasitic element for DC blocking and the independent operation of each switch.

The principles used to design the antenna are those underlying the perturbation method [11], through which resonant frequency can be controlled by changing the volume of a metal cavity (Fig. 2 and Eq. (1)). This method is also commonly used as reference in miniaturizing antennas.

$$\frac{\omega-\omega_o}{\omega_o} \approx \frac{\iiint_{\Delta\tau}\left(\mu|\overrightarrow{H_o}|^2-\varepsilon|\overrightarrow{E_o}|^2\right)d\tau}{\iiint_{\tau}\left(\mu|\overrightarrow{H_o}|^2+\varepsilon|\overrightarrow{E_o}|^2\right)d\tau} \quad (1)$$

where ω_o is resonant frequency; E_o, electric field; and H_o, magnetic field.

Fig. 3 presents the fabricated prototype antenna.

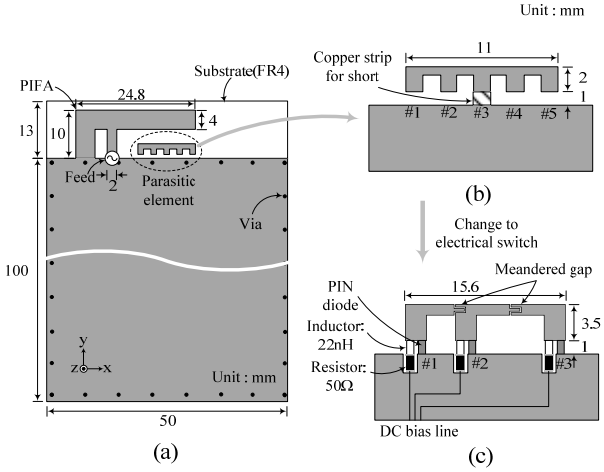

Fig. 1. (a) FTPIFA with basic perturbed parasitic element, (b) perturbed parasitic element, and (c) perturbed parasitic element with PIN diode switch.

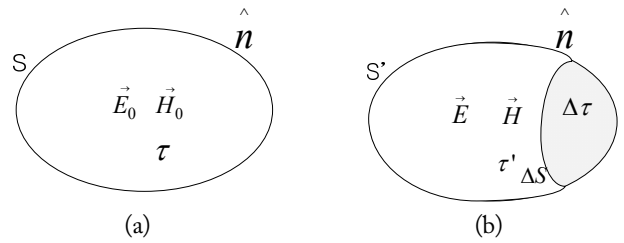

Fig. 2. Perturbation principle: (a) original metal cavity and (b) perturbed metal cavity.

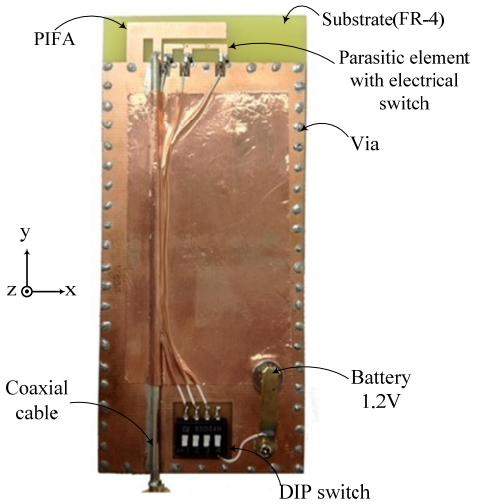

Fig. 3. Fabricated prototype antenna.

III. Simulation and Measured Results

Fig. 4 shows the FTPIFA's S_{11}, which was measured from the short-circuit operation of short positions #1 to #5 to verify changes in the resonant frequency of the antenna. Also Fig. 4 indicates that the resonant frequency decreased as the short position moved from #1 to #5 and that the central frequency (2.1 GHz) was determined when switch #3 was shorted. Because of the extent of the electric field, the magnetic energy between the antenna and the ground plane was changed by the short-circuit operation and on the basis of the perturbation principle [3]. In other words, the resonant frequency increased because of the

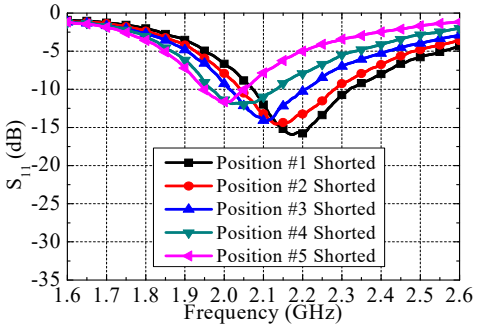

Fig. 4. Short position-based S_{11} of the FTPIFA with a perturbed parasitic element.

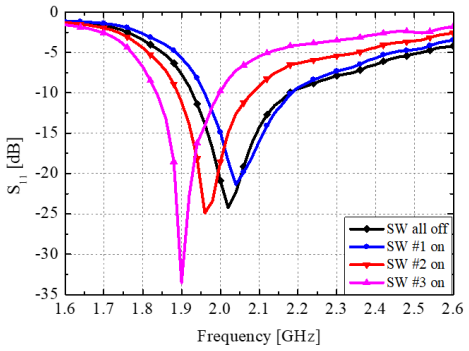

Fig. 5. Electrical switched-measured S_{11} of the FTPIFA.

reduction in the volume of the magnetic field energy near the feeding point when position #1 was shorted. Conversely, the resonant frequency decreased because of the reduction in the volume of the electric field energy at the edge of the radiated element when position #5 was shorted.

The electrical operation of the shorted position was realized by applying a DC bias to the PIN diodes. An inductor (22 nH) for AC cut-off and a meandered gap on the parasitic element for the independent operation of a switch were also used. Fig. 5 shows the S_{11} measured from the operation of switches #1 to #3, which were manipulated by turning a PIN diode on and off to determine changes in the antenna's resonant frequency. The number of switches was limited to three for equal intervals of frequency movement. When switch #1 was on, the upper frequency was resonant, but when switch #3 was on, the resonant frequency decreased given the change in the volume of the electric field energy. The measured −10 dB bandwidth covers 1.83 to 2.17 GHz, and the total tunable resonant frequency is 340 MHz (17.3%).

Fig. 6 shows the radiation patterns measured at each resonant frequency of the antenna prototype when the switches were on. The H-plane patterns of the vertical element that indicates directivity to the x-axis are shown in Fig. 6(a), and the H-plane patterns of the horizontal element overcoming a null point are displayed in Fig. 6(b). As can be seen, the designed antenna could maintain the radiation patterns of a basic inverted-F antenna, regardless of switch position.

Fig. 7 shows the simulated and measured peak gains when each switch was on. The simulated and measured average realized gains were 3.0 dBi and 3.1 dBi, respectively, pointing to a reasonably good agreement between the simulation and measurement.

Finally, Table 1 summarizes the measured total efficiency and peak gain of the designed antenna at resonant frequencies. These amounted to 88.0% and 3.44 dBi at 2.02 GHz, respectively, when all the switches were off. When the switches were activated (switched on) sequentially, the measured total efficiency was 72.0% for switch #1, 68.9% for switch #2, and 56.2% for switch #3.

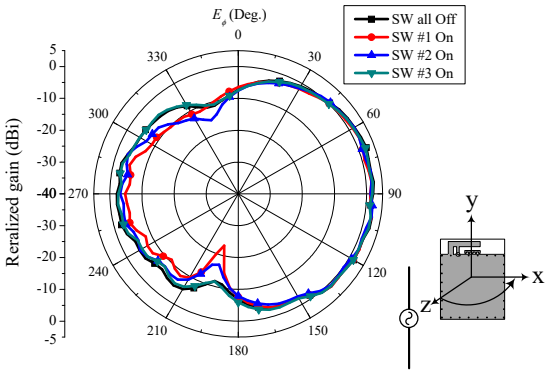

(a)

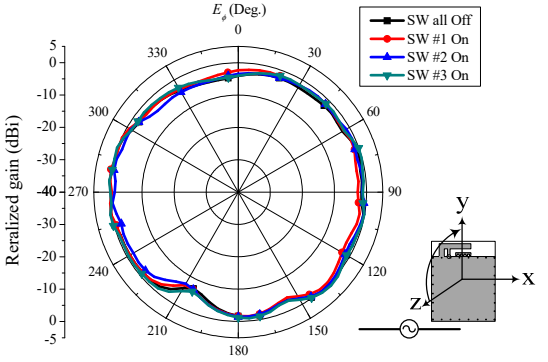

(b)

Fig. 6. Radiation patterns measured on the basis of short positions: (a) xz-plane (E_{φ}) and (b) yz-plane (E_{φ}).

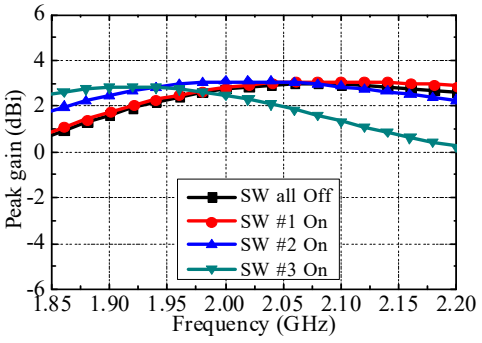

(a)

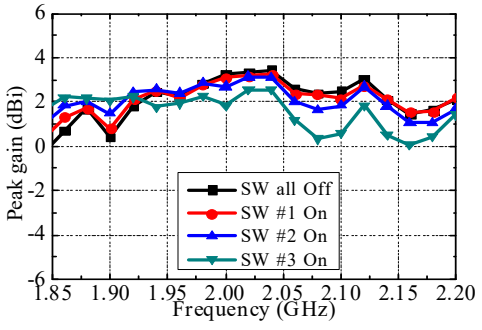

(b)

Fig. 7. Peak gains measured using an electrical switch: (a) simulation and (b) measurement.

Table 1. Total efficiency levels and peak gains of the designed antenna

	Resonant frequency (GHz)	Total efficiency (%)	Peak gain (dBi)
All switches off	2.02	88.0	3.22
Switch #1 on	2.04	72.0	2.20
Switch #2 on	1.96	68.9	2.17
Switch #3 on	1.90	56.2	1.47

IV. Conclusion

An FTPIFA with a perturbed parasitic element was developed in this study. The designed antenna could be easily modified via the short- and open-circuit operation of the parasitic element between the antenna and the ground plane. It was redesigned by incorporating a gap capacitor into the parasitic element for the independent operation of each switch. As the resonant frequency varied considerably at the end of the radiator, a non-linear interval was arranged in the parasitic element. The antenna could also maintain the radiation patterns of a basic inverted-F antenna, regardless of switch position, and could be easily changed without loading and tuning the chip element on the antenna. Therefore, it is fully applicable to 5G technology and can selectively achieve the frequency band necessitated by an allocated frequency bandwidth.

References

[1] L. Zhu, H. S. Hwang, E. Ren, and G. Yang, "High performance MIMO antenna for 5G wearable devices," in *Proceedings of 2017 IEEE International Symposium on Antennas and Propagation & USNC/URSI National Radio Science Meeting*, San Diego, CA, 2017, pp. 1869–1870.

[2] M. Abdullah, Y. L. Ban, K. Kang, M. Y. Li, and M. Amin, "Compact four-port MIMO antenna system at 3.5 GHz," in *Proceedings of 2017 IEEE 2nd Advanced Information Technology, Electronic and Automation Control Conference (IAEAC)*, Chongqing, China, 2017, pp. 656–660.

[3] H. S. Lee, J. M. Woo, and J. C. Kim, "Printed type inverted-F antenna," in *Proceedings of 1999 KEES Microwave and Electromagnetic Wave Communication Conference*, Gwangju, Korea, 1999, pp. 253–256.

[4] J. H. Lim, C. W. Song, Z. J. Jin, and T. Y. Yun, "Frequency reconfigurable planar inverted-F antenna using switchable radiator and capacitive load," *IET Microwaves, Antennas & Propagation*, vol. 7, no. 6, pp. 430–435, 2013.

[5] V. A. Nguyen, M. T. Dao, Y. T. Lim, and S. O. Park, "A compact tunable internal antenna for personal communication handsets," *IEEE Antennas and Wireless Propagation Letters*, vol. 7, pp. 569–572, 2008.

[6] L. Liu, J. Rigelsford, and R. Langley, "Tunable multiband handset antenna operating at VHF and UHF bands," *IEEE Transactions on Antennas and Propagation*, vol. 61, no. 7, pp. 3790–3796, 2013.

[7] C. A. Balanis, *Antenna Theory: Analysis and Design*, 3rd ed. Hoboken, NJ: John Wiley & Sons, 2005, pp. 197–204.

[8] J. T. Aberle, S. H. Oh, D. T. Auckland, and S. D. Rogers, "Reconfigurable antennas for wireless devices," *EEE Antennas and Propagation Magazine*, vol. 45, no. 6, pp. 148–154, 2003.

[9] D. M. Pozar and V. Sanchez, "Magnetic tuning of a microstrip antenna on a ferrite substrate," *Electronics Letters*, vol. 24, no. 12, pp. 729–731, 1988.

[10] R. F. Harrington. *Time-Harmonic Electromagnetic Fields*. New York, NY: McGraw-Hill, 1961, pp. 317–319.

[11] M. H. Song and J. M. Woo, "Miniaturisation of microstrip patch antenna using perturbation of radiating slot," *Electronics Letters*, vol. 39, no. 5, pp. 417–419, 2003.

[12] Y. R. Kim and J. M. Woo, "Electrically tunable small microstrip antenna using interdigital plate loading for telemetry sensor applications," *Electronics Letters*, vol. 48, no. 8, pp. 422–423, 2012.

Yoon-Seon Choi

received her B.S. and M.S. degrees in radiowave engineering from Chungnam National University in 2014 and 2016, respectively. She is currently working toward her Ph.D. degree at the antenna laboratory. Her main research interest is antennas.

Ji-Hun Hong

received his B.S. degree in radiowave engineering from Chungnam National University in 2018. He is currently working toward his M.S. degree at the antenna laboratory. His main research interest is antennas.

Jong-Myung Woo

received his B.Sc. degree in electronics engineering from Konkuk University in Korea and Ph.D. degree in electronics engineering from Nihon University in Japan. He is a professor of Department of Radio and Information Communications Engineering in Chungnam National University in Korea. He is mainly interested in antennas.

JOURNAL OF ELECTROMAGNETIC ENGINEERING AND SCIENCE, VOL. 20, NO. 3, 169~175, JUL. 2020

https://doi.org/10.26866/jees.2020.20.3.169
ISSN 2671-7263 (Online) · ISSN 2671-7255 (Print)

Design and Analysis of a TEM Mode Rectangular Coaxial Waveguide for Mobile 5G Millimeter Wave Antenna Module Applications

Eunyoung Park · Sangkil Kim*

Abstract

In this paper, design and analysis of a transverse electromagnetic (TEM) mode rectangular coaxial waveguide for a mobile 5G millimeter wave (mmWave) antenna module are presented. General structures of 5G radio frequency (RF) module for mobile sub-6 GHz and mmWave applications are also discussed in this paper. Thorough analysis of transmission line and waveguide structures at mmWave frequency band is essential and fundamental information to design highly integrated RF front-end modules. Theoretical design equations of the waveguide, such as impedance, loss, and radiation are presented, and the equations are verified by a full wave 3D FEM electromagnetic simulator. Impedance value of the rectangular waveguide structure was calculated using the conformal mapping method. Theoretical operation frequency bandwidth and design guide are also presented. The characteristics and analysis of the rectangular coaxial waveguide structure presented in this paper is easily scalable to other frequency bands. The proposed design equations are also applicable to various planar layer-by-layer integrated circuit (IC) or module manufacturing process.

Key Words: Millimeter-Wave, mmWave Module, RF Front-End, TEM Mode, Waveguide, 5G Communication System.

I. Introduction

In April 2019, a commercial sub-6 GHz band mobile 5G communication network service was launched in South Korea for the first time. The 5G communication features an ultra-fast data rate up to several Gbps and ultra-low latency of several ms. Various unprecedented user experiences and technologies, such as augmented reality (AR), smart factory/hospital, cloud computing, and self-driving cars, are available due to the 5G communication network [1, 2]. The next technical challenge is to implement millimeter wave (mmWave) 5G technology operating at 28 GHz or 39 GHz. This technology is able to improve data rates dramatically by fully utilizing its broad bandwidth of 800–1,000 MHz. The wavelength at the mmWave 5G frequency band is less than 10 mm, which is a comparable size to radio frequency front-end (RFFE) module chips. For this reason, the antennas for mmWave 5G communication could be implemented in the package (antenna-in-package [AiP]) [3]. The distance between the radio frequency integrated circuit (RFIC) and the antenna could be minimized, and the mmWave signals could be tightly confined within the waveguide structures.

The 5G mmWave module was designed using system-in-package (SiP) technology [4, 5]. Many functional chips and

Manuscript received January 9, 2020 ; Revised March 24, 2020 ; Accepted March 30, 2020. (ID No. 20200109-006J)
Department of Electronics Engineering, Pusan National University, Busan, Korea.
*Corresponding Author: Sangkil Kim (e-mail: ksangkil3@pusan.ac.kr)

passive components, such as power management integrated circuit (PMIC), RFIC, antenna, and SMDs, were integrated in a single package laminate, and the module was connected through a flexible RF cable. The RF cable is a critical component, as DC power, analog/digital control, and intermediate frequency (IF) signals are carried by it. Therefore, it is essential for the 5G mmWave module to design and analyze the RF cable thoroughly. This paper discusses the design requirements of the RF cable and presents a proper waveguide structure with thorough theoretical analysis.

II. 5G mmWave Module for Mobile Devices

A high-frequency module is a key component of the RFFE chain. Usually, low noise amplifiers (LNAs), power amplifiers (PAs), filters, duplexers, and antenna switches are integrated into a single chip using the SiP technology. It is an essential part of mobile wireless communication systems because it is able to integrate many IC chips made through various processes (CMOS, GaAs, or SiGe) into a single module chip. The general structure of an RF module for 5G applications is shown in Fig. 1.

The most widely used commercial sub-6 GHz band RF modules for 4G-LTE and 5G communication consist of Rx/Tx amplifiers (LNAs and PAs), an antenna tuning system, and multiplexers (Fig. 1). The antennas are not integrated within the module because they are much larger than the module chip at the sub-6 GHz frequency band (3.6 GHz). However, the operating frequency bands for 5G mmWave RFFE module are 28 GHz and 39 GHz, and their half-wavelength ($\lambda_g/2$) is less than 5 mm in the free space. It is feasible to integrate antennas and RFICs in a single package (module chip) due to an antenna size comparable to the RFICs.

The world's first commercially available 5G mmWave module chip for mobile devices also has a structure similar to Fig. 1 [6]. Antenna arrays, antenna feeding networks, mixed analog/digital signals, and RF connectors are integrated in a single package substrate. IC chips and other passive components were mounted on the other side of the antenna array. Mixed analog and digital signals, such as IF band, baseband, and mmWave RF signals, travel through the transmission lines embedded in the module or external connectors/cables. The RF cable is one of the most critical components of the 5G mmWave antenna module, as the RF cable and connector carry IF, digital control, VDD, and baseband signals. Therefore, it is necessary to analyze the structure of the cable thoroughly to design the mmWave antenna module for mobile devices.

III. A TEM Mode Waveguide for Mobile 5G mmWave Module Applications

The first step of the RF cable design for the mobile 5G mmWave module is to find a proper transmission line (or waveguide) structure. RF cables for 5G mmWave modules should support a broad frequency spectrum from DC to GHz band. VDD and digital/analog control signals range from DC to a few hundred MHz, and IF signals are located at 6–10 GHz. It is desirable to use a low-loss TEM (transverse electromagnetic) mode waveguide structure to minimize signal dispersion and achieve an ultra-wide operation frequency bandwidth (extremely high cutoff frequency). Furthermore, the capability of extending to a multi-signal line structure is also important for signal integrity. A multi-line circular coaxial structure satisfies most of the above conditions, but it is challenging to build a compact connector and stacked line structure. A rectangular coaxial structure is an appropriate structure to meet all the design considerations.

Fig. 2 shows the proposed structure of a rectangular coaxial waveguide. In the case of Fig. 2(a), each side of the waveguide is closed with a continuous metal wall. The structure shown in Fig.

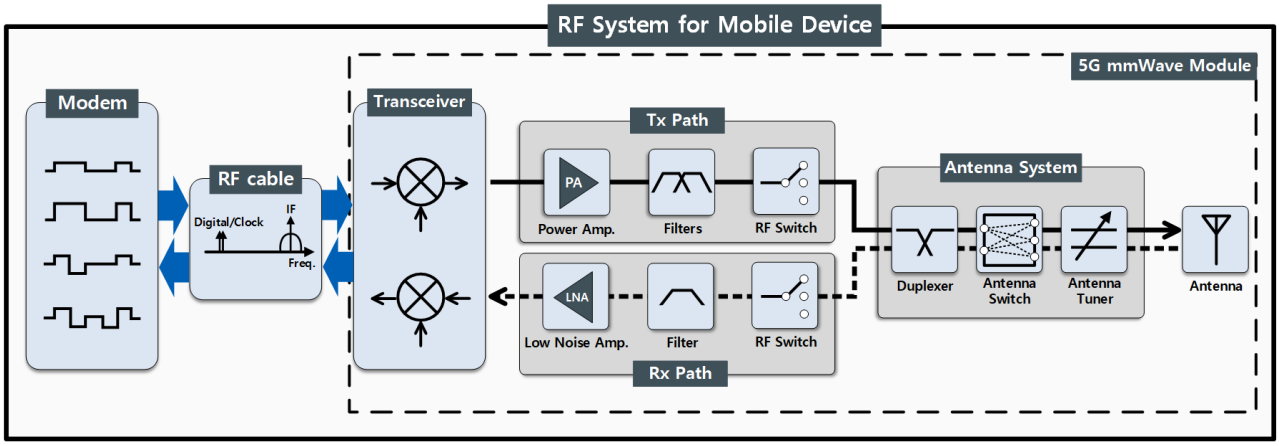

Fig. 1. The structure of a 5G mmWave antenna module for mobile devices.

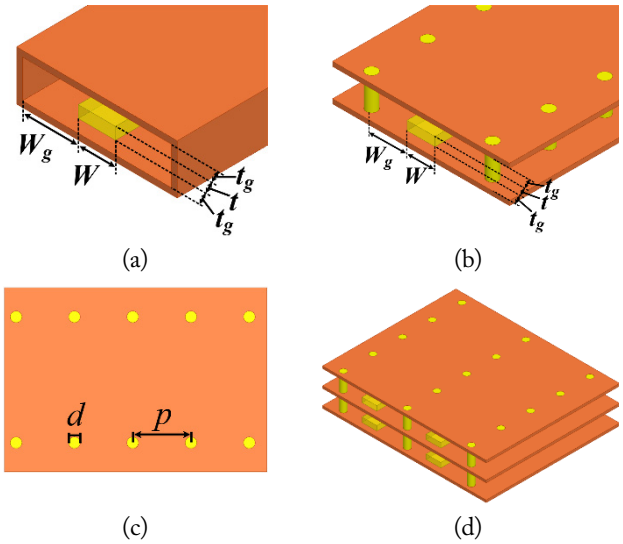

Fig. 2. (a) Rectangular coaxial waveguide with continuous side walls, (b) practical model with via walls, (c) practical model with via wall, and (d) stacked multi-line rectangular coaxial waveguide.

2(a) is a desirable structure due to complete field confinement, but it is challenging to implement a continuous metal wall on the flexible substrate. The structure using the via wall is more practical, as shown in Fig. 2(b), (c), and (d). The via pitch is a critical design parameter in this case, as it controls field leakage (radiation) from the waveguide structure and coupling between the adjacent waveguides. It is possible to achieve more than a 60-dB isolation level between the waveguides easily when each waveguide supports TEM mode waves. Fig. 2(b) and (c) show that both the left and right sides of the rectangular waveguide are closed through the via wall. It is easy and practical to extend the rectangular cable to the multi-line structure, as shown in Fig. 2(d). By sharing the via-wall or metal surface between the adjacent waveguides, the waveguides can be arranged densely without wasting space, and the electromagnetic fields can be effectively confined in the cross-section of the waveguide.

In this section, important design parameters, such as the waveguide impedance (Z_0), loss (α), cutoff frequency (f_c), and via pitch (p) of the rectangular coaxial waveguide, are discussed.

1. Impedance

The impedance of a TEM mode waveguide is expressed as follows. L and C are the inductance (L/m) and capacitance (F/m) per unit length, respectively, v_p is the phase velocity in the given waveguide structure and material, and ε_{eff} is the effective dielectric constant of the dielectric material. The characteristic impedance and phase velocity of a TEM mode waveguide can be expressed as Eqs. (1) and (2).

$$Z_0 = \sqrt{\frac{L}{C}} = \frac{1}{v_p C} \quad (\Omega) \tag{1}$$

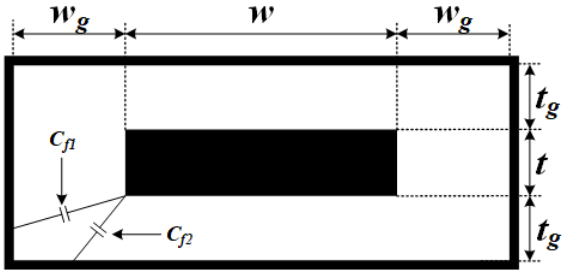

Fig. 3. Rectangular coaxial waveguide structure section and design variables.

$$v_p = 1/\sqrt{\mu \cdot \varepsilon_{eff}} \ \ (m/s) \tag{2}$$

As written in (1), C is a dominant parameter of the characteristic impedance value. Fig. 3 shows a cross-section of the rectangular coaxial waveguide. A rectangular signal line is located at the center of the waveguide. The impedance of the waveguide can be calculated by computing the total capacitance (C_t) per unit length, which is obtained through the conformal mapping of the field distribution from a cylindrical to a rectangular geometry [7]. The C_t value includes the corner capacitance values per unit length (C_{f1} and C_{f2}), in addition to the capacitance per unit length of the conventional circular coaxial waveguide [8, 9]. C_{f1} and C_{f2} can be expressed as Eqs. (3) and (4), and the resulting C_t and Z_0 are also shown in Eqs. (5) and (6).

$$C_{f1} = \frac{\varepsilon_{eff}}{\pi}\left[\log\left(\frac{w_g^2+t_g^2}{4t_g^2}\right) + \frac{2t_g}{w_g}\tan^{-1}\left(\frac{w_g}{t_g}\right)\right] \ \text{(F/m)} \tag{3}$$

$$C_{f2} = \frac{\varepsilon_{eff}}{\pi}\left[\log\left(\frac{w_g^2+t_g^2}{4w_g^2}\right) + \frac{2w_g}{t_g}\tan^{-1}\left(\frac{t_g}{w_g}\right)\right] \ \text{(F/m)} \tag{4}$$

$$C_t = 2\varepsilon_{eff}\left(\frac{w}{t_g} + \frac{t}{w_g}\right) + 4\left(C_{f1} + C_{f2}\right) \ \text{(F/m)} \tag{5}$$

$$Z_0 = \frac{\eta_0}{\sqrt{\varepsilon_{eff}}\left[2\left(\frac{w}{t_g}+\frac{t}{w_g}\right)+\frac{4}{\varepsilon_{eff}}(C_{f1}+C_{f2})\right]} \ (\Omega) \tag{6}$$

The proposed equations were verified by comparing calculated results to the computation data of the commercial full-wave 3D simulator, HFSS v17.1 (Ansys Inc., Canonsburg, PA, USA). Fig. 4 shows the impedance variation according to the value of the signal line width (w) for each rectangular coaxial waveguide in the vacuum core (Fig. 4(a)) and filled with Teflon (Fig. 4(b)). For the calculation, all the metals were set to copper ($\sigma = 5.96 \times 10^7$ Ω/m), and the electrical properties of Teflon were defined as $\varepsilon_r = 2.0$ and $\tan\delta = 0.001$. The simulated and formulated results agree well. A designed practical 50 Ω rectangular coaxial waveguide has $w_g = 68$ μm, $w = 120$ μm, $t_g = 42$ μm, and $t = 16$ μm.

2. Cutoff Frequency

A coaxial waveguide consisting of two conductors, by their nature, supports a TEM mode. The operating frequency band

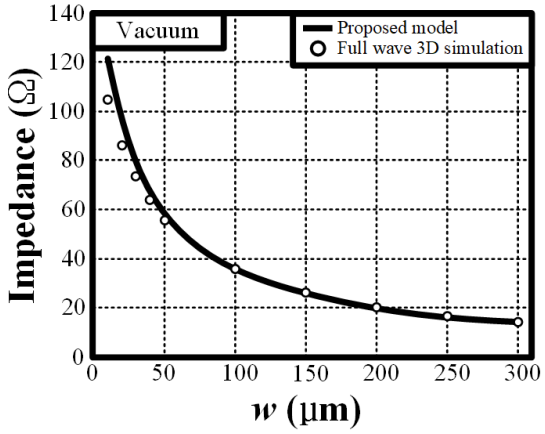

(a)

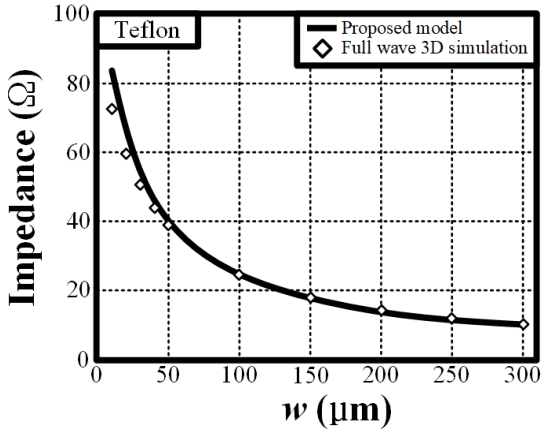

(b)

Fig. 4. Impedance change of rectangular coaxial waveguide filled by (a) vacuum and (b) Teflon.

width of a TEM mode waveguide can be defined from DC to the frequency at which any high-order wave propagation mode is excited. The first high-order mode of a square coaxial waveguide is TE_{01} or TE_{10}. The cutoff frequency (f_c) of the rectangular coaxial waveguide's TE_{10} mode can be expressed by the transcendental equation, and it can be calculated by Eqs. (7)–(9) [10]. For the TE_{01} mode, the design parameters should be modified as $t_g \rightarrow w_g$, $w \rightarrow t$, $w_g \rightarrow t_g$, and $t \rightarrow w$.

$$\cot\left(\frac{2\pi t_g f_c}{v_p}\right) - \tan\left(\frac{t\pi f_c}{v_p}\right) = \frac{B}{Y_{C1}} \tag{7}$$

$$\frac{B}{Y_{C1}} = \frac{2f_c}{v_p}(w+2w_g)\left[-\ln(4u) + \frac{1}{3}u^2 + \frac{1}{2}(1-u^2)^4\left(\frac{f_c(w+2w_g)}{v_p}\right)^2\right] \tag{8}$$

$$u = \frac{2w_g}{w+2w_g} \tag{9}$$

Because (7) and (8) are transcendental equations, it is difficult to obtain an analytical solution. In this paper, a graphical method was chosen to obtain solutions to the transcendental equations, as shown in Fig. 5. The values of the variables used were a 50-Ω waveguide designed in section A. The first high-order mode cutoff frequency of the 50-Ω rectangular coaxial waveguide was about 334 GHz. Therefore, the operating frequency bandwidth of the designed waveguide was DC to 334 GHz, which was much higher than the operation frequency of the 5G mmWave module.

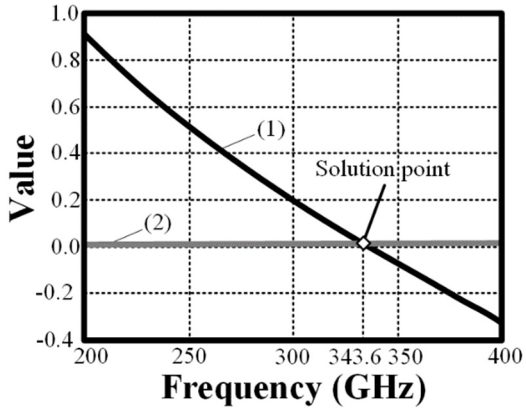

Fig. 5. Graphical analysis of high-order mode of a rectangular coaxial waveguide.

3. Loss

The total loss (α_t) of a TEM mode rectangular coaxial waveguide can be divided into three parts as, shown in (10): radiation (leakage) loss (α_l), dielectric loss (α_d), and conductor loss (α_c).

$$\alpha_t = \alpha_l + \alpha_c + \alpha_d \cong \alpha_c + \alpha_d \tag{10}$$

There is negligible radiation loss when the waveguide is closed with continuous metal walls or a fine-pitched via array. Each loss can be calculated as shown in (11) and (12) [11].

$$\alpha_d = \frac{k_0^2 \tan\delta}{2k_z} = \frac{k_0 \tan\delta}{2\sqrt{\varepsilon_r}} \tag{11}$$

$$\alpha_c = \frac{47.09R_S}{\eta Z_0}\left(1+\frac{t+2t_g}{w}\right)\frac{w}{\left[0.2794(t+2t_g)+0.7206w\right]^2} \quad \text{for } (t+2t_g)/w < 2.5$$

$$\alpha_c = \frac{59.37R_S}{\eta Z_0}\left(1+\frac{t+2t_g}{w}\right)\frac{1}{t+2t_g} \quad \text{for } 2.5 \le (t+2t_g)/w \le 4$$

$$\alpha_c = \frac{47.09R_S}{\eta Z_0}\left(1+\frac{t+2t_g}{w}\right)\frac{1}{t+2t_g} \quad \text{for } (t+2t_g)/w < 4 \tag{12}$$

R_s is the sheet resistance of the metal ($R_s = 1/(\delta_s \cdot \sigma)$), η is the intrinsic impedance $\left(\eta = \sqrt{\mu/\varepsilon}\right)$ of the medium, Z_0 is the characteristic impedance of the transmission line $\left(Z_0 = \sqrt{L/C}\right)$. Fig. 6 shows the calculated and simulated attenuation constants of a rectangular coaxial waveguide made of copper and

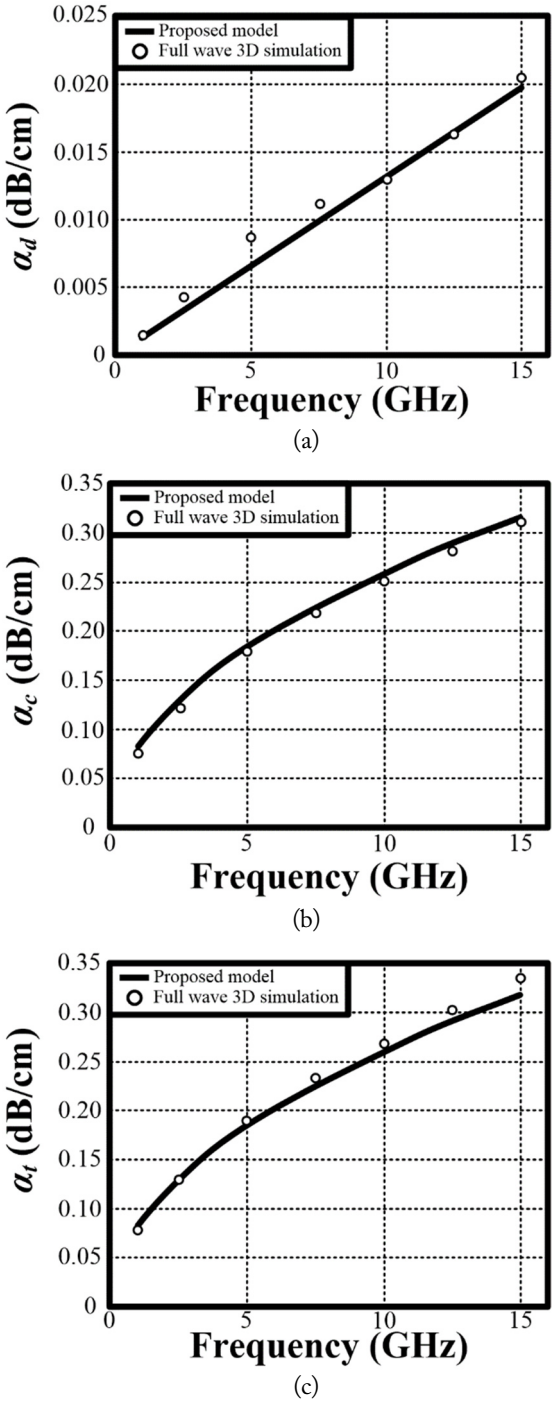

Fig. 6. Loss of rectangular coaxial waveguide composed of Teflon: (a) dielectric loss, (b) conductor loss, and (c) total loss.

Teflon. The simulated and calculated results are well matched.

4. Via Pitch

Continuous sidewalls can be considered as via arrays with zero pitch length but it is challenging to implement solid metal walls in the flexible RF or module substrate. The periodically arranged via wall shown in Fig. 2(b) and (c) is a more practical structure than the continuous metal wall. The critical design parameters are the diameter (d) and pitch (p) of the vias. The electromagnetic bandgap (EBG) should be considered because the via wall is a periodic structure [12, 13]. From (13), the first visible bandgap occurs when $n = 1$.

$$\beta_z = n\pi \tag{13}$$

$$p = \frac{\pi}{\beta_z} = \frac{\lambda_g}{2} \tag{14}$$

It is clear that the via pitch should be shorter than the half-wavelength, as shown in (14). The smallest via pitch is defined by mechanical durability and feasibility. It is desirable to set the minimum via-to-via distance of the fabrication process, but excessive via density decreases the mechanical durability of the designed rectangular coaxial waveguide. As a rule of thumb, the maximum via pitch should be less than a quarter wavelength of the guided wave, and the minimum via pitch is $\lambda_g/20$ when the design and fabrication margins are considered. It should be noted that the maximum via pitch is a hard bound because the bandgap effect should be prevented. The minimum via pitch is a soft bound that varies depending on the manufacturing capability and process. Fig. 7 graphically presents the via design guide when the via pitch (p) and diameter (d) are given. The via diameter and pitch are normalized by the guided wavelength. The upper half plane is a reasonable design area, as the via diameter cannot be larger than the via pitch.

5. Radiation

Electromagnetic radiation is strictly regulated by law for the public health. According to the FCC regulations for electromagnetic radiation (47 CFR 15.109 Radiated emission limits) [14], mobile devices are classified as Class B, as shown in Table 1. The 5G mmWave module or cable should not exceed 500 μV/m of electric field intensity (**E**) at a point 3-m away from the device under test (DUT).

Based on the given regulations and the Poynting vector theorem, the maximum allowed power leakage is obtained as follows. Because the distance (r) from the DUT is 3 m, the electromag-

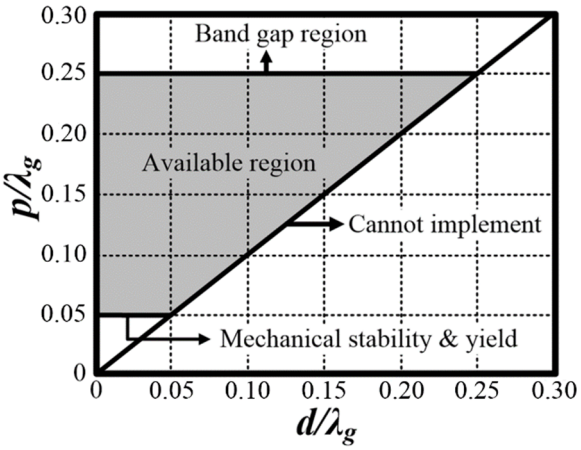

Fig. 7. Graphical analysis for the via wall design.

Table 1. FCC regulation for Class-B devices

Frequency (MHz)	E-field (μV/m)
30–88	90
88–216	150
216–960	210
>960	300

netic field having a frequency higher than 10 GHz can be considered the far field at the measurement point. It is reasonable to assume the radiated EM field is a TEM wave. In the spherical coordinates, the relationship between the electric field (**E**) and the magnetic field (**H**) intensities satisfies the following conditions.

$$\mathbf{E} = E_\theta \hat{\theta} \tag{15}$$

$$\mathbf{H} = H_\phi \hat{\phi} \tag{16}$$

$$H_\phi = E_\theta / \eta \tag{17}$$

Using Poynting's vector theorem, the total amount of radiated power (P_{rad}) can be obtained as follows [15].

$$\begin{aligned} P_{rad} &= \oiint_S (\mathbf{E} \times \mathbf{H}) \cdot d\boldsymbol{s} \\ &= \oiint_S \left(E_\theta \hat{\theta} \times H_\phi^* \hat{\phi}\right) \cdot \hat{r} ds \\ &= \oiint_S \left(E_\theta \hat{\theta} \times H_\phi^* \hat{\phi}\right) \cdot (r^2 \sin\theta) \hat{r} d\phi d\theta \\ &= \oiint_S \left(E_\theta \cdot \frac{E_\theta^*}{\eta_0}\right) \cdot (\hat{r} \cdot \hat{r}) (r^2 \sin\theta) d\phi d\theta \\ &= \frac{|E_\theta|^2}{\eta_0} \int_0^\pi \int_0^{2\pi} r^2 \sin\theta \;\; d\phi d\theta \\ &= \frac{|E_\theta|^2}{\eta_0} 4\pi r^2 \end{aligned} \tag{18}$$

where the intrinsic impedance (η_0) of the free space is 120π, the radiated E-field strength, and the total radiated power are summarized as follows.

$$|E_\theta| = \sqrt{\frac{\eta_0 P_{rad}}{4\pi r^2}} = \frac{\sqrt{30 P_{rad}}}{r} \tag{19}$$

$$P_{rad} = \frac{(r|E_\theta|)^2}{30} \;\; \text{(W)} \tag{20}$$

Therefore, in accordance with FCC regulations, the total radiated power leakage from the designed waveguide structure should not exceed 75 nW to generate an electric field ($|E_\theta|$) less than the FCC requirement of 500 μV/m at a distance of 3 m from the DUT. It should be noted that the FCC's radiation regulation can be verified at a distance of less than 3 m from the DUT by evaluating (21) at any distance.

IV. Conclusion

In this paper, the design and analysis of a TEM mode rectangular coaxial waveguide was presented. Detailed design equations for the TEM mode rectangular coaxial waveguide structure, including impedance, loss, bandwidth, vias, and radiation analysis, were also discussed. The design parameters of the 50 Ω TEM mode waveguide were presented and its electrical characteristics were thoroughly studied as a design example. The proposed TEM mode waveguide design and analysis are scalable to other applications such as beyond-5G or sub-THz applications.

This work was supported by the National Research Foundation of Korea (NRF) grant funded by the Korea government (MSIT) (No. 2020R1C1C1003362) and the Air Force Office of Scientific Research (No. FA2386-19-1-0124).

REFERENCES

[1] A. Gupta and R. K. Jha, "A survey of 5G network: architecture and emerging technologies," *IEEE Access*, vol. 3, pp. 1206-1232, 2015.

[2] M. Agiwal, A. Roy, and N. Saxena, "Next generation 5G wireless networks: a comprehensive survey," *IEEE Communications Surveys & Tutorials*, vol. 18, no. 3, pp. 1617-1655, 2016.

[3] Y. P. Zhang and D. Liu, "Antenna-on-chip and antenna-in-package solutions to highly integrated millimeter-wave devices for wireless communications," *IEEE Transactions on Antennas and Propagation*, vol. 57, no. 10, pp. 2830-2841, 2009.

[4] S. Kim and J. Kim, "Design of reconfigurable antenna feeding network using coupled-line switch for 5G Millimeter-wave communication system," *Applied Computational Electromagnetics Society Journal*, vol. 33, no. 8, pp. 861-867, 2018.

[5] M. Swaminathan, J. Kim, I. Novak, and J. P. Libous, "Power distribution networks for system-on-package: Status and challenges," *IEEE Transactions on Advanced Packaging*, vol. 27, no. 2, pp. 286-300, 2004.

[6] Qualcomm, "Qualcomm announces second generation 5G RF front-end solutions for sleeker, more efficient 5G multimode mobile devices," 2019 [Online]. Available: https://www.qualcomm.com/news/releases/2019/02/19/qualcomm-announces-second-generation-5g-rf-front-end-solutions-sleeker-more.

[7] M. Lukic, S. Rondineau, Z. Popovic, and S. Filipovic, "Modeling of realistic rectangular μ-coaxial lines," *IEEE Transactions on Microwave Theory and Techniques*, vol. 54, no. 5, pp. 2068-2076, 2006.

[8] T. S. Chen, "Determination of the capacitance, inductance, and characteristic impedance of rectangular lines," *IRE Transactions on Microwave Theory and Techniques*, vol. 8, no. 5,

pp. 510-519, 1960.
[9] J. R. Reid, E. D. Marsh, and R. T. Webster, "Micromachined rectangular-coaxial transmission lines," *IEEE Transactions on Microwave Theory and Techniques*, vol. 54, no. 8, pp. 3433-3442, 2006.
[10] L. Gruner, "Higher order modes in rectangular coaxial waveguides," *IEEE Transactions on Microwave Theory and Techniques*, vol. 15, no. 8, pp. 483-485, 1967.
[11] K. H. Lau, "Loss calculations for rectangular coaxial lines," *IEE Proceedings H-Microwaves, Antennas and Propagation*, vol. 135, no. 3, pp. 207-209, 1988.
[12] D. Deslandes and K. Wu, "Accurate modeling, wave mechanisms, and design considerations of a substrate integrated waveguide," *IEEE Transactions on Microwave Theory and Techniques*, vol. 54, no. 6, pp. 2516-2526, 2006.
[13] M. Pasian, M. Bozzi, and L. Perregrini, "A formula for radiation loss in substrate integrated waveguide," *IEEE Transactions on Microwave Theory and Techniques*, vol. 62, no. 10, pp. 2205-2213, 2014.
[14] Code of Federal Regulations, "47 CFR 15.109 - Radiated emission limits," 2010 [Online]. Available: http//www.govinfo.gov/app/details/CFR-2010-title47-vol1/CFR-2010-title47-vol1-sec15-109/summary.
[15] D. M. Pozar, *Microwave Engineering*, 3rd ed. Hoboken, NJ: John Wiley & Sons, 2005.

Eunyoung Park

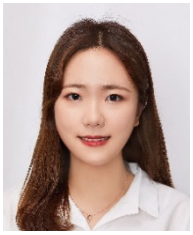

received the B.S. degree in electronics engineering at Pusan National University, Busan, South Korea, in 2020, where she is currently working toward the Ph.D. degree. Her current research interests include RF packaging and antenna modules for mmWave.

Sangkil Kim (M'18)

received the B.S. degree in Electrical and Electronic Engineering from Yonsei University, Seoul, South Korea, in 2010. He received his M.S. and Ph.D. degrees in Electrical and Computer Engineering from Georgia Institute of Technology, Atlanta, GA, USA, in 2012 and 2014, respectively. He visited King Abdullah University of Science and Technology, Thuwal, Saudi Arabia, in 2013; Centre Technologic Telecommunications Catalunya (CTTC), Barcelona, Spain, in 2013; and CNRS-LAAS, Toulouse, France, in 2013; as a visiting scholar. He worked on the world's first 5G antenna module for mobile devices at Qualcomm Inc. in 2015–2018. He is currently an Assistant Professor in the Department of Electronics Engineering, Pusan National University, Busan, South Korea. His work has been covered in 25 peer-reviewed journals, 38 international conference proceedings, and five book chapters. Dr. Kim was the recipient of the 2015 IET Microwaves, Antennas and Propagation Premium Award and the 2018 Pusan National University Department of Electronics Engineering Distinguished Faculty Achievement Award. He is a committee member of MTT-24 RFID Technologies since April 2018.

JOURNAL OF ELECTROMAGNETIC ENGINEERING AND SCIENCE, VOL. 20, NO. 3, 176~182, JUL. 2020

https://doi.org/10.26866/jees.2020.20.3.176
ISSN 2671-7263 (Online) · ISSN 2671-7255 (Print)

Array Antenna Design for Passive Coherent Location Systems with Non-Uniform Array Configurations

Doyoung Jang[1] · Jun Hur[2] · Hongsuk Shim[3] · Junsik Park[3] · Chihyun Cho[4] · Hosung Choo[1,*]

Abstract

This study investigates non-uniform array configurations to maximize the beamforming performance of passive coherent location (PCL) systems. The proposed array consists of eight dipole elements that are divided into two groups with different distances from the array center. This double-layered non-uniform configuration is designed considering the array antenna characteristics (peak-to-side lobe ratio, first null bandwidth, null width, and null depth). The resulting antenna array can provide more appropriate patterns for PCL systems than a conventional uniform circular array. The target detection performance of the proposed array in PCL systems is tested in a certain scenario. The results demonstrate that the proposed antenna in PCL systems can detect the target with Doppler and range errors of 1 Hz and 1.2 km, respectively, in a given situation.

Key Words: Antenna, Array Antenna, Passive Coherent Location, Passive Radar.

I. Introduction

Passive coherent location (PCL) systems based on non-cooperative sources such as FM and TV signals have been developed successfully in recent years [1–4]. The purpose of a PCL system is to detect and track airborne targets using a reference and a surveillance channel. The reference channel, used to obtain commercial broadcast signals, should steer the beam toward a base station, and at the same time the surveillance channel should have a radiation pattern that includes deep null toward the base station. From the correlation between the signals of the two channels, targets can be detected and tracked [5, 6]. However, in general, echo signals reflected from potential targets are extremely weak and are obscured by strong direct signals. To increase the detectability of echo signals by minimizing the terrestrial multipath effect and other clutters, interference suppression techniques that support the accuracy of direction-of-arrival information are typically used [7–10]. In addition, the probability hypothesis density and the multi-frame assignment have been proposed to enhance the detection performance of PCL systems [11–13]. Their performance can be further optimized by improving the performance of the antennas employed in PCL systems. For example, antenna elements with multi-band and dual polarization characteristics have been designed to increase the probability of target detection by expanding the operating frequency and available polarization. Although studies aiming to determine the optimal beam pattern of the array for PCL systems according to various array configurations have also

Manuscript received February 3, 2020 ; Revised March 18, 2020 ; Accepted March 30, 2020. (ID No. 20200203-014J)
[1]School of Electronic and Electrical Engineering, Hongik University, Seoul, Korea.
[2]Metamaterial Electronic Device Research Center, Hongik University, Seoul, Korea.
[3]Hanwha Systems Co. Ltd., Seongnam, Korea.
[4]Korea Research Institute of Standards and Science, Daejeon, Korea.
[*]Corresponding Author: Hosung Choo (e-mail: hschoo@hongik.ac.kr)

been conducted [14, 15], they are limited to certain canonical forms of array configurations. Other studies have performed optimizations of array configurations using various optimization methods, such as the particle swarm algorithm [16], the invasive weed algorithm [17], and the genetic algorithm [18]. However, non-uniform array configurations that can effectively improve the array performance of PCL systems have not been sufficiently considered.

In this paper, we propose a non-uniform array configuration to maximize the beamforming performance of PCL systems. The proposed array consists of eight dipole elements divide into two groups with different distances from the array center. This double-layered non-uniform configuration is used to observe the trends of beamforming performance for various array configurations. Each element is designed and fabricated to operate in the FM frequency band, and the antenna performance required for PCL systems are examined. The array antenna characteristics—peak-to-side lobe ratio (PSLR), first null bandwidth (FNBW), null width, and null depth—are then investigated to derive the optimum array configuration. Parametric studies of various array distances are conducted, and the optimal configuration is determined by evaluating the cost function of the beamforming performance. To verify the performance enhancement of the proposed array, the reference and surveillance beams are compared with the conventional uniform circular array (UCA). The results demonstrate that the proposed non-uniform array configuration has more suitable beam patterns compared with the conventional UCA. The target detection performance of the proposed array for PCL systems is tested in a certain scenario.

II. Design of the Dipole Element

Fig. 1 shows a photograph of the fabricated dipole element with a broadband balun (ADT1.5–1+, Mini-Circuits) embedded in the circuit board. The balun operates in a range from 1 to 300 MHz with an insertion loss of less than 1 dB. This structure can help minimize the pattern distortion by the unbalanced current of the coaxial feed while maintaining the broadband matching characteristics. Thanks to its compact size ($7.9 \times 5.6 \times 2.8$ mm^3), the balun can be mounted on a board, as shown in Fig. 1(a) and (b). It provides the housing structure with the circuit board to protect the circuit from external physical shocks while reliably attaching the dipole antenna to it. The fully manufactured dipole with the housing is shown in Fig. 1(c). The length and radius of the dipole are $h = 134$ cm and $r = 7.5$ mm, respectively.

Fig. 2 provides a comparison of the measured and simulated voltage standing wave ratios (VSWRs) of the proposed dipole element (solid and dashed lines, respectively). The measurement

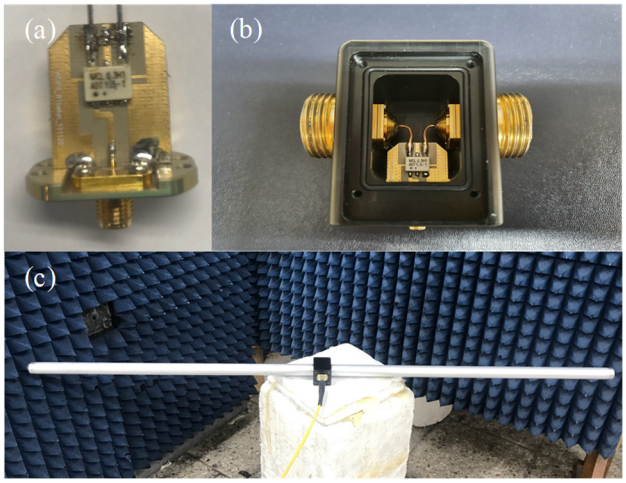

Fig. 1. Photograph of the dipole element for the PCL array: (a) balun with circuit board, (b) housing structure, and (c) dipole element.

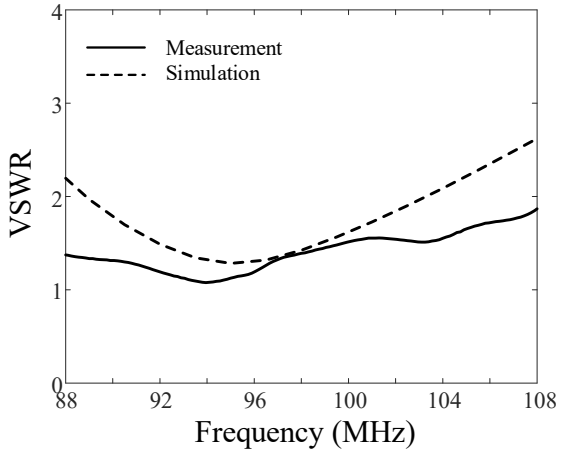

Fig. 2. Measured and simulated VSWRs of the dipole element.

is performed in a semi-anechoic chamber, resulting in a bandwidth of 23 MHz (from 85 MHz to 108 MHz, VSWR < 2) with a fractional bandwidth greater than 23%. The fractional bandwidth of the simulated VSWR is 17%, which shows good agreement with the measured data. Fig. 3 illustrates the boresight gain as a function of frequency. The solid line represents the measured data, which maintains a gain above 1 dBi from 88 to 108 MHz. The simulation values are similar to the measured values, with differences less than 0.5 dB. These results show that the performance of the designed dipole element is suitable for a PCL system.

III. Proposed Array Configuration

Fig. 4 shows the geometry of the proposed non-uniform eight-element array for PCL systems. It consists of two groups (inner and outer layers) with different distances d_1 and d_2 from the array center, as shown in Fig. 4(a). The expandable mast

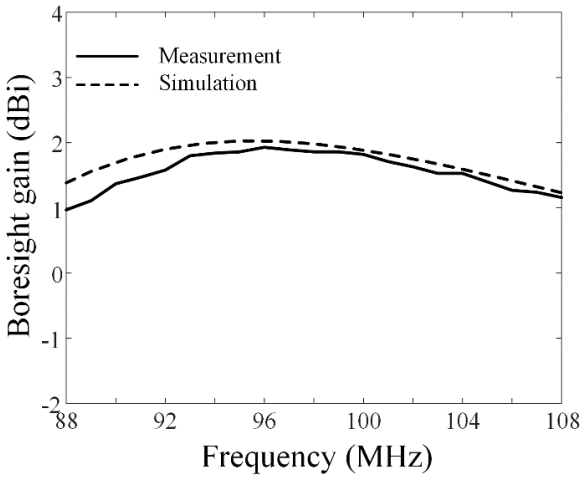

Fig. 3. Measured and simulated boresight gain of the dipole element.

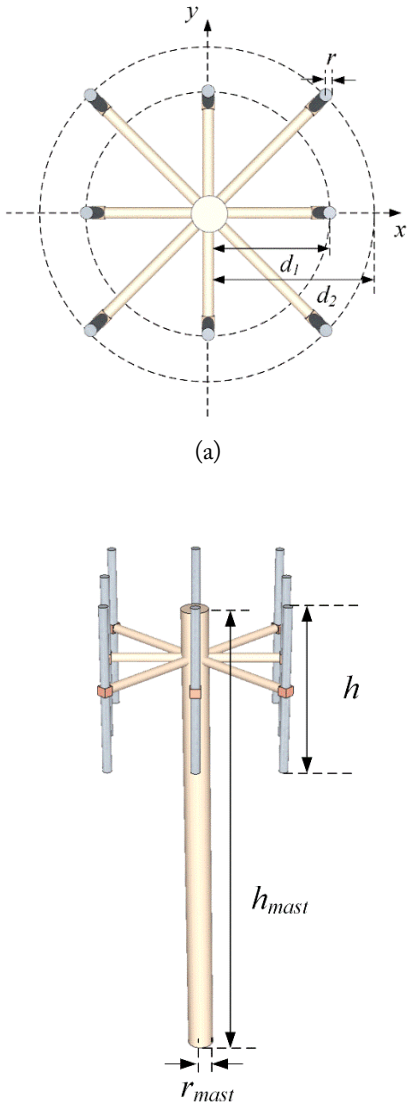

(a)

(b)

Fig. 4. Configuration of the proposed array: (a) top view and (b) isometric view.

Table 1. Parameters of the proposed array

Parameter	Value
d_1	0.41λ
d_2	0.32λ
d_{ratio} (d_2/d_1)	0.8
h	134 cm
r	7.5 mm
h_{mast}	8.6 mm
r_{mast}	30 mm

with length h_{mast} and radius r_{mast} is used to mount the array elements. WIPL-D Pro electromagnetic simulation software (WIPL-D, Belgrade, Serbia) is used to optimize and analyze the proposed configuration. The optimum design parameters are displayed in Table 1.

To effectively detect targets, the array antenna of the PCL system must be able to generate two different channels: the reference and the surveillance channel. Since PCL systems are passive radar systems that do not generate a reference signal, commercial broadcast signals from FM base stations are often used as reference signals for detecting targets. Therefore, the beam pattern of the reference channel should have a higher PSLR and narrower FNBW to obtain only the reference signal from the base station. However, the beam pattern of the surveillance channel requires a greater null depth and a narrower null width toward the base station. This is because the surveillance channel should only receive scattered signals from targets without the reference signals. The optimum array configuration is derived by considering the beam patterns of the reference and surveillance channels. The mask functions for the reference and surveillance beams are used to obtain the optimized beam patterns [15]. The mask function $F(\phi)$ can be calculated as

$$A \cdot \omega = F(\phi) \tag{1}$$

where A and ω are the array manifold and weightings to create the beam pattern of the proposed non-uniform array, respectively. The weightings for the beam pattern are then calculated with the following equation:

$$\omega = \left(A^H \cdot A \right)^{-1} \cdot A^H \cdot F(\phi) \tag{2}$$

From Eq. (2), we can derive the weightings ω that can minimize the square error between the pattern and the mask function. Since the FM band ranges from 88 to 108 MHz, the array characteristics of the PSLR, FNBW, null depth, and null width are examined at three specific frequencies: 88, 98, and 108 MHz. The cost function to assess array performance is defined to achieve the optimal array configuration as follows:

$$Cost_r = \left(1-\alpha\frac{PSLR(x,y)}{PSLR_{\max}}\right)+\gamma\frac{FNBW(x,y)}{FNBW_{\max}} \quad (3)$$

$$Cost_s = \left(1-\beta\frac{Nulldepth(x,y)}{Nulldepth_{\max}}\right)+\delta\frac{Nullwidth(x,y)}{Nullwidth_{\max}} \quad (4)$$

$$Cost_{total} = Cost_r + Cost_s \quad (5)$$

where $Cost_r$ and $Cost_s$ are the cost functions of the reference and surveillance beams, respectively. These costs are computed using the PSLR, FNBW, null depth, and null width. Weight constants of $\alpha = 0.8$, $\beta = 0.5$, $\gamma = 0.2$, and $\delta = 0.5$ are used in the optimization. Lower cost means more appropriate beam pattern.

Fig. 5 illustrates the total cost map according to d_1 and d_{ratio}. d_1 is changed from 0.4λ to 0.6λ at intervals of 0.01λ, and d_{ratio} is varied from 0.5 to 1.5 with intervals of 0.05. The minimum cost of 0.67 is obtained when d_1 and d_{ratio} are 0.41λ and 0.8, respectively, while a cost of 0.7 is observed with the UCA configuration ($d_1 = d_2 = 0.5\lambda$).

Fig. 6 shows the patterns of the reference and surveillance beams at a center frequency of 98 MHz in the FM band. The solid lines indicate the beam pattern of the proposed array, and the dashed lines represent the beam pattern of the UCA configuration. For the proposed array, the PSLR and FNBW are 13.3 dB and 139°, respectively, and the null depth and null width are 37.5 dB and 23°, respectively. The exact values of the PSLR, FNBW, null depth, and null width at all analysis frequencies are listed in Table 2. The results indicate that the average PSLR and null depth at three frequencies (88, 98, and 108 MHz) are greater than those in the UCA configuration by 0.7 dB and 0.7 dB, respectively.

To verify the detection performance using the proposed array, an amplitude range–Doppler map is created as shown Fig. 7. In the given scenario, the distance between the PCL radar and the target is assumed to be 100 km, and the target's velocity is assumed to be 551 m/s. The received reference and surveillance

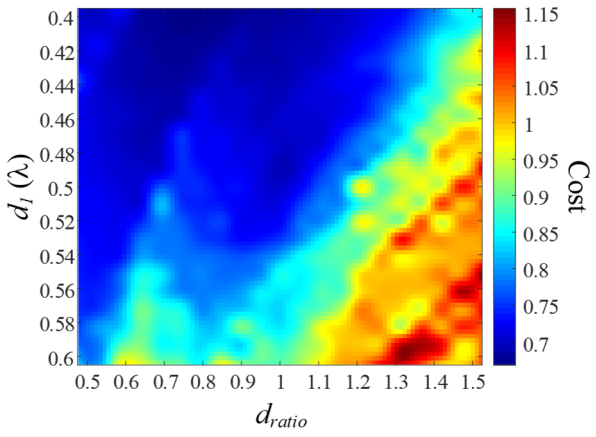

Fig. 5. Total cost map according to d_1 and d_{ratio}.

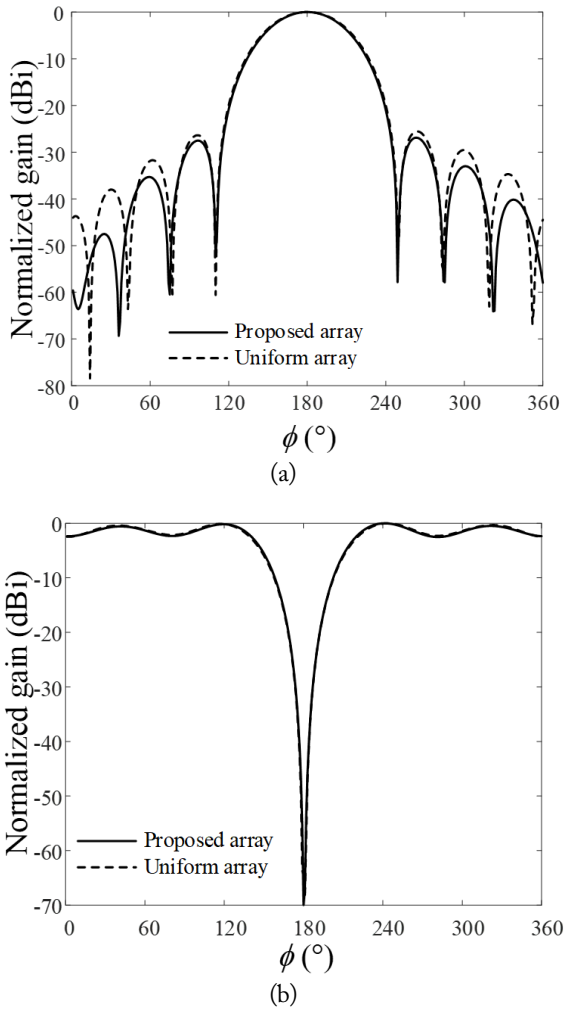

Fig. 6. Beam patterns of the proposed and uniform circular array at 98 MHz: (a) reference channel and (b) surveillance channel.

signals are used in the cross-correlation equation to obtain the amplitude range–Doppler map. The cross correlation χ can be calculated as

$$\chi(t, f_d) = \int_{-\infty}^{\infty} x(t)\cdot x(t-\tau)^* e^{j2\pi f_d t}\cdot dt \quad (6)$$

Table 2. Comparison of array antenna characteristics

Parameter	PSLR (dB)	FNBW (°)	Null depth (dB)	Null width (°)
88 MHz				
Proposed array	13.5	139	35.0	23
UCA	12.8	140	32.1	23
98 MHz				
Proposed array	13.3	139	37.5	23
UCA	12.5	140	38.0	23
108 MHz				
Proposed array	12.9	139	32.4	27
UCA	12.3	140	32.8	23

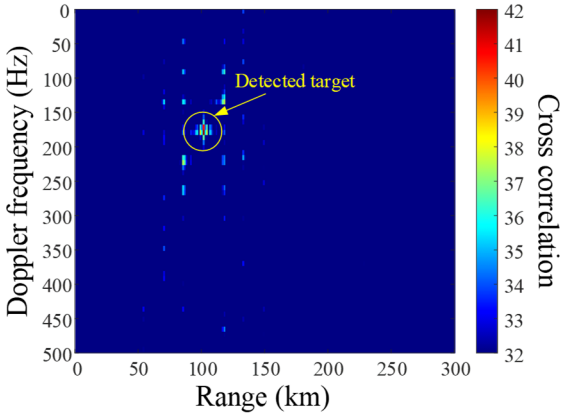

Fig. 7. Amplitude range–Doppler map for a detected target in a given scenario.

where τ is the signal delay between the received reference and surveillance signals, and f_d is the Doppler frequency according to the target's velocity. With a target velocity of 551 m/s, the actual Doppler frequency is 180 Hz. The value derived from the correlation equation is 179 Hz. The estimated range between the PCL radar and the target is 101.2 km, which is close to the scenario's range of 100 km. These results demonstrate that the proposed non-uniform array for PCL systems can effectively detect targets.

IV. Conclusion

Non-uniform array configurations were investigated to maximize the beamforming performance of PCL systems. The proposed array consisted of eight dipole elements that are divided into two groups with distances of 0.41λ and 0.32λ from the array center, respectively. The individual dipole element had a bandwidth of 23 MHz (85 to 108 MHz, VSWR < 2), which showed suitable performance for PCL systems. The array antenna characteristics (PSLR, FNBW, null width, and null depth) were then investigated to derive the optimum array configuration. The results showed that the average PSLR and null depth of the proposed array at three frequencies (88, 98, and 108 MHz) were greater than those of the UCA configuration by 0.7 dB and 0.7 dB, respectively. Moreover, the proposed non-uniform array configuration had more suitable beam patterns compared with the conventional UCA. The target detection performance of the proposed array was tested in a certain scenario, and the target was detected with Doppler and range errors of 1 Hz and 1.2 km, respectively.

This work was supported by a grant-in-aid from Hanwha Systems.

References

[1] S. Paine, D. W. O'Hagan, M. Inggs, C. Schupbach, and U. Boniger, "Evaluating the performance of FM-based PCL radar in the presence of jamming," *IEEE Transactions on Aerospace and Electronic Systems*, vol. 55, no. 2, pp. 631-643, 2018.

[2] C. R. Berger, B. Demissie, J. Heckenbach, P. Willett, and S. Zhou, "Signal processing for passive radar using OFDM waveforms," *IEEE Journal of Selected Topics in Signal Processing*, vol. 4, no. 1, pp. 226-238, 2010.

[3] F. Colone, D. Langellotti, and P. Lombardo, "DVB-T signal ambiguity function control for passive radars," *IEEE Transactions on Aerospace and Electronic Systems*, vol. 50, no. 1, pp. 329-347, 2014.

[4] P. E. Howland, D. Maksimiuk, and G. Reitsma, "FM radio based bistatic radar," *IEE Proceedings-Radar, Sonar and Navigation*, vol. 152, no. 3, pp. 107-115, 2005.

[5] C. K. Kim, J. S. Lee, J. S. Chae, and S. O. Park, "A modified stripmap SAR processing for vector velocity compensation using the cross-correlation estimation method," *Journal of Electromagnetic Engineering and Science*, vol. 19, no. 3, pp. 159-165, 2019.

[6] S. G. Ha, J. Cho, J. Lee, B. W. Min, J. Choi, and K. Y. Jung, "Numerical study of estimating the arrival time of UHF signals for partial discharge localization in a power transformer," *Journal of Electromagnetic Engineering and Science*, vol. 18, no. 2, pp. 94-100, 2018.

[7] J. Wang, H. T. Wang, and Y. Zhao, "Direction finding in frequency-modulated-based passive bistatic radar with a four-element adcock antenna array," *IET Radar, Sonar & Navigation*, vol. 5, no. 8, pp. 807-813, 2011.

[8] R. Tao, H. Z. Wu, and T. Shan, "Direct-path suppression by spatial filtering in digital television terrestrial broadcasting-based passive radar," *IET Radar, Sonar & Navigation*, vol. 4, no. 6, pp. 791-805, 2010.

[9] M. Malanowski, K. Kulpa, and J. Misiurewicz, "Acceleration estimation for passive coherent location radar," in *Proceedings of 2008 IEEE Radar Conference*, Rome, Italy, 2008, pp. 1-5.

[10] G. H. Park, D. G. Kim, H. J. Kim, and H. N. Kim, "Maximum-likelihood angle estimator for multi-channel FM-radio-based passive coherent location," *IET Radar, Sonar & Navigation*, vol. 12, no. 6, pp. 617-625, 2018.

[11] M. Radmard, S. M. Karbasi, and M. M. Nayebi, "Data fusion in MIMO DVB-T-based passive coherent location," *IEEE Transactions on Aerospace and Electronic Systems*, vol. 49, no. 3, pp. 1725-1737, 2013.

[12] R. Tharmarasa, M. Subramaniam, N. Nadarajah, T. Kirubarajan, and M. McDonald, "Multitarget passive coher-

ent location with transmitter-origin and target-altitude uncertainties," *IEEE Transactions on Aerospace and Electronic Systems*, vol. 48, no. 3, pp. 2530-2550, 2012.

[13] M. Tobias and A. D. Lanterman, "Probability hypothesis density-based multitarget tracking with bistatic range and Doppler observations," *IEE Proceedings-Radar, Sonar and Navigation*, vol. 152, no. 3, pp. 195-205, 2005.

[14] M. Villano, F. Colone, and P. Lombardo, "Antenna array for passive radar: configuration design and adaptive approaches to disturbance cancellation," *International Journal of Antennas and Propagation*, vol. 2013, article no. 920639, 2013.

[15] M. Malanowski and K. Kulpa, "Digital beamforming for passive coherent location radar," in *Proceedings of 2008 IEEE Radar Conference*, Rome, Italy, 2008, pp. 1-6.

[16] H. Li, Y. Jiang, Y. Ding, J. Tan, and J. Zhou, "Low-sidelobe pattern synthesis for sparse conformal arrays based on PSO-SOCP optimization," *IEEE Access*, vol. 6, pp. 77429-77439, 2018.

[17] G. G. Roy, S. Das, P. Chakraborty, and P. N. Suganthan, "Design of non-uniform circular antenna arrays using a modified invasive weed optimization algorithm," *IEEE Transactions on Antennas and Propagation*, vol. 59, no. 1, pp. 110-118, 2011.

[18] K. K. Yan and Y. Lu, "Sidelobe reduction in array-pattern synthesis using genetic algorithm," *IEEE Transactions on Antennas and Propagation*, vol. 45, no. 7, pp. 1117-1122, 1997.

Doyoung Jang

received his B.S. degree in information and telecommunication engineering from Dongyang Mirae University, Seoul, Korea in 2018 and his M.S. degree in electronic and electrical engineering from Hongik University, Seoul, Korea in 2020. He worked as a research engineer in MOASOFT, Seoul, Korea, from 2015 to 2018. He is currently working toward an Ph.D. degree in electronic and electrical engineering at Hongik University, Seoul, Korea. His research interests include direction finding, passive radars, electromagnetic wave propagation, and electromagnetic environmental effects.

Hongsuk Shim

received his B.S. in computer engineering from Chungbuk National University, Cheongju, Korea in 2005 and his M.S. degree in computer engineering from Chungnam National University, Daejeon, Korea in 2008. He is currently working as a researcher for Hanwha Systems, Pangyo, Korea. His research interests include electronic warfare systems, electronic support, electronic attack, and electronic and communications intelligence signal analysis and processing.

Jun Hur

received his B.S., M.S., and Ph.D. degrees in electronic and electrical engineering from Hongik University, Seoul, Korea in 2014 and 2019, respectively. Since 2019, he has been a postdoctoral researcher at the Metamaterial Electronic Device Research Center of Hongik University. His research interests include global positioning system antennas, antenna arrays, and position optimization of array elements for adaptive beamforming.

Junsik Park

received his B.S. and M.S. degrees in electronic engineering from Chonbuk National University, Jeonju, Korea in 2014 and 2016, respectively. He is currently working as a researcher for Hanwha Systems, Pangyo, Korea. His research interests include electronic warfare systems, electronic support, electronic attack, and military antenna and RF circuits.

Chihyun Cho

received his B.S., M.S., and Ph.D. degrees in electronic and electrical engineering from Hongik University, Seoul, Korea, in 2004, 2006, and 2009, respectively. From 2009 to 2012, he participated in the development of military communication systems at the Communication R&D Center, Samsung Thales, Seongnam, Korea. Since 2012, he has been Principal Research Scientist with the Korea Research Institute of Standards and Science, Daejeon, Korea. In 2014, he was a guest researcher at the National Institute of Standards and Technology in Boulder, CO, USA. He also served in the Presidential Advisory Council on Science and Technology in Seoul, Korea in 2016–2017. His current research interests include microwave metrology, time–domain measurements, and standards of communication parameters.

Hosung Choo

received his B.S. degree in radio science and engineering from Hanyang University in Seoul in 1998 and his M.S. and Ph.D. degrees in electrical and computer engineering from the University of Texas at Austin, in 2000 and 2003, respectively. In September 2003, he joined the school of electronic and electrical engineering, Hongik University, Seoul, Korea, where he is currently a full professor. His principal areas of research are the use of the optimization algorithm in developing antennas and microwave absorbers. His studies include the design of small antennas for wireless communications, reader and tag antennas for RFID, and on-glass and conformal antennas for vehicles and aircraft.

JOURNAL OF ELECTROMAGNETIC ENGINEERING AND SCIENCE, VOL. 20, NO. 3, 183~189, JUL. 2020

https://doi.org/10.26866/jees.2020.20.3.183
ISSN 2671-7263 (Online) · ISSN 2671-7255 (Print)

Characteristics of the Angled Printed Dipole Array Antenna with Different Numbers of Dipole Elements

Heesu Wang · Ikmo Park*

Abstract

This paper investigated the characteristics of series-fed angled dipole antennas as the number of dipoles increased from one to two, four, and eight. A parallel strip line printed on both sides of the substrate was used to connect angled printed dipoles of the same size in a series with equal spacing. As expected, although the gain increased as the number of dipoles increased, the impedance and gain bandwidths decreased. In addition, as the number of dipoles increased, the half-power beamwidth (HPBW) differences between the xz- and yz-planes decreased and the radiation pattern of the xz-plane became more symmetric. Antennas with one, two, four, and eight-dipole elements in a series were designed, and their peak gains were 5.0 dBi, 7.2 dBi, 9.4 dBi, and 10.4 dBi, respectively. The differences between the xz- and yz-plane HPBWs of the four antennas were 160.4°, 41.7°, 14.2°, and 5.3°, respectively. As the number of dipoles in the antenna increased, the differences between the HPBWs in the xz- and yz-planes decreased.

Key Words: Dipole Array, Endfire Antenna, Ka-Band, Millimeter-Wave Antenna, Printed Dipole Antenna, 5G Antenna.

I. Introduction

The 5G wireless communication systems use the high carrier frequency of low millimeter-wave bands to enhance the rate of data transmission. However, because this use of high carrier frequencies increases propagation loss over distance, the need for a high-gain antenna to overcome this problem has become significant [1–5]. The endfire dipole antenna, which is printed on both sides of a substrate, is widely used in wireless communication systems and consists of a small, simple structure with a wide impedance bandwidth and stable gain [6–9].

However, single-printed dipole antennas exhibit low gain, making them inapplicable for use at high frequencies. The radiation pattern of a single-printed dipole antenna is typically asymmetrical, which causes the beam scanning range to present asymmetrically, making it difficult to use for two-dimensional phased array antennas [10–13]. Metal cavity-backed antenna structures, or Yagi-Uda antenna structures with multiple directors, are used to increase the gain and symmetricity of the radiation patterns [14–22]. Metal cavity-backed antennas have similar half-power beamwidths (HPBWs) in the E- and H-planes of their radiation pattern. Thus, the radiation pattern is symmetrical and the antenna gain is high due to cavity resonance. Nonetheless, metal cavity-backed antennas are heavy and expensive [23]. A Yagi-Uda antenna structure can achieve a high gain and symmetrical radiation pattern at a small size and low price, but its antenna characteristics can be difficult to optimize due to the number of directors is increased [24, 25].

In this paper, we propose an array antenna with a symmetrical radiation pattern and high gain by connecting multiple dipole elements in a series. In the proposed array antenna, several identical dipole elements are connected in a series using parallel strip

Manuscript received January 2, 2020 ; Revised March 31, 2020 ; Accepted April 22, 2020. (ID No. 20200102-002J)
Department of Electrical and Computer Engineering, Ajou University, Suwon, Korea.
*Corresponding Author: Ikmo Park (e-mail: ipark@ajou.ac.kr)

lines printed on both sides of the substrate. We designed a single dipole antenna, and array antennas with two-, four-, and eight-dipoles and compared their characteristics.

II. Single Dipole Antenna Design and Characteristics

Fig. 1 shows the geometry of the single angled printed dipole antenna with the dipole bent 45° toward the ground plane. Angled dipoles are smaller than straight dipoles and have excellent matching performance. In addition, mutual coupling is low when used as an array [13, 14]. This paper used an angled dipole because of the abovementioned advantages. The detailed design procedure and characteristics of the single-element angled dipole antenna can be found in [14]. The substrate used in the antenna design is a Rogers RO4003C ($\varepsilon_r = 3.38$, $\tan\delta = 0.0027$) substrate, and its thickness is 0.2032 mm. Each arm of the single dipole antenna is printed on both sides of the substrate, and the power input through the microstrip line of the truncated ground plane is transferred to the dipole through the parallel strip lines printed on both sides of the substrate. Each dipole is connected by a parallel strip line, and the length of L_q is adjusted so that the impedance of the parallel strip line and the 50-Ω microstrip line match. An ANSYS High Frequency Structure Simulator (HFSS) was used to simulate and optimize a single angled printed dipole antenna, and the design parameters of the optimized antenna were as follows: $W = 10$ mm, $L = 14.8$ mm, $L_g = 10$ mm, $L_d = 2.2$ mm, $W_d = 0.3$ mm, $S = 2$ mm, $S_{d1} = 2.8$ mm, $W_r = 0.3$ mm, $L_q = 1.6$ mm, $W_q = 0.3$ mm, and $W_f = 0.5$ mm.

Fig. 2 illustrates the characteristics of a single angled dipole antenna. The –10 dB impedance bandwidth is 25.6–31.0 GHz, and the 3-dB gain bandwidth is 20.1–34.9 GHz. The gain at the center frequency of 28 GHz is 4.5 dBi, and the cross-polarization level is less than –15.1 dB. The HPBWs of the *xz*- and *yz*-planes are 62.6° and 219.3°, respectively, and the HPBW of the *yz*-plane is approximately 157° wider than the HPBW of the *xz*-plane. Moreover, the radiation pattern of the *xz*-plane is asymmetrical. In line with the endfire direction, the HPBWs on the left and right sides of the radiation pattern are indicated as HPBW_L and HPBW_R—with the corresponding angles of 34° and 28.6°—respectively. HPBW_L is approximately 5.4° wider than HPBW_R. The *xz*-plane radiation patterns present asymmetrically in a single dipole due to the considerable influence of the truncated ground plane that acts as a reflector. Each arm of the dipole is printed symmetrically on both sides of the substrate; however, the truncated ground plane exists in only some areas on one side of the substrate, making the whole structure asymmetrical. Therefore, the radiation pattern of the *xz*-plane presents asymmetrically, and the main beam direction is tilted.

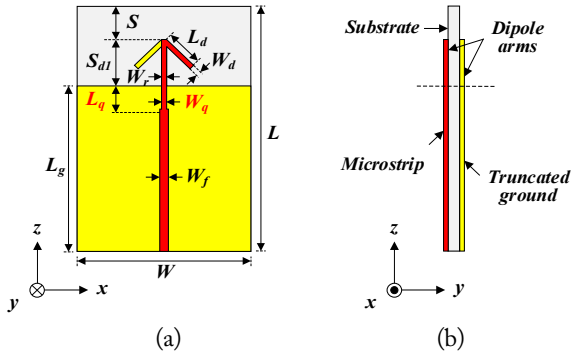

Fig. 1. A single-printed angled dipole antenna: (a) front view and (b) side view.

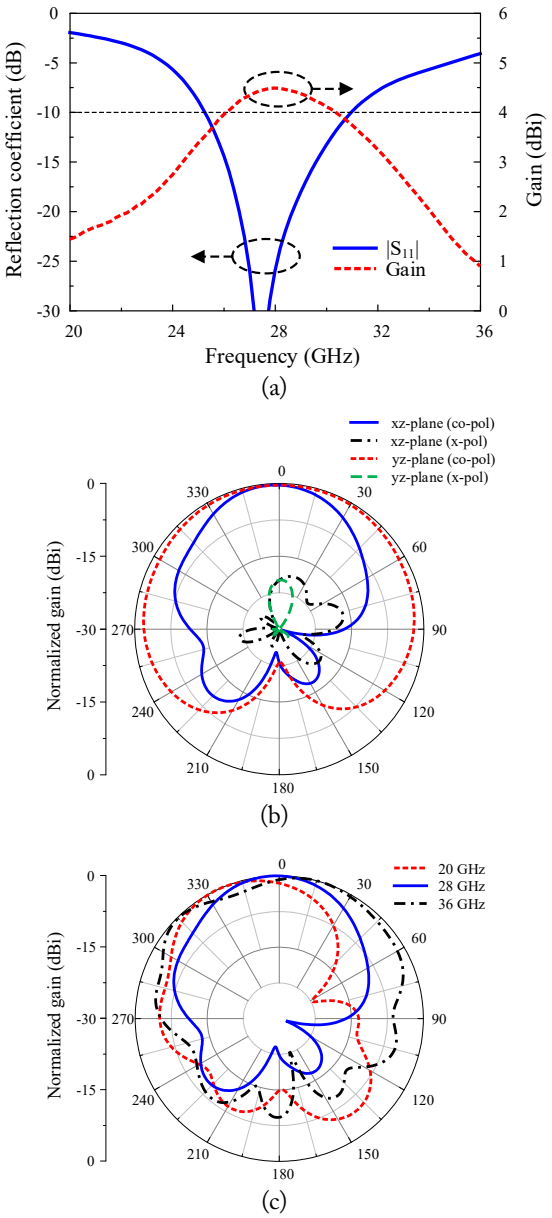

Fig. 2. Simulation results of the single dipole antenna: (a) reflection coefficient and gain curve, (b) radiation pattern at 28 GHz, and (c) radiation pattern of the *xz*-plane at three different frequencies.

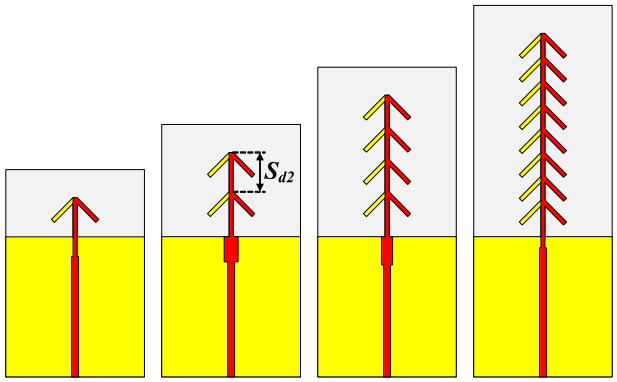

Fig. 3. Series-fed array antenna geometry.

III. Series-Fed Dipole Array Antennas

Fig. 3 shows the structure of series-fed printed dipole arrays with dipole elements of the same size as the single-printed dipole antenna above. Two, four, and eight-dipole elements were connected in a series, and the antennas' characteristics were optimized. The spacing and phase differences between the dipole elements of the series-fed endfire array determine the gain of the array. To maximize the gain of the endfire array, the phase difference between dipole elements must decrease as the number of dipole elements in the array increases [26]. Therefore, the spacing between dipoles, S_{d2}, was reduced when the number of dipoles of the array increased. The exact value of S_{d2}, which provides the maximum gain at the center frequency, was obtained through a parametric study. A quarter-wave transformer was used to match the impedance of the 50-Ω microstrip line and the array antenna, and the length, S_{d1}, of the parallel strip line connecting the first dipole and the microstrip line was adjusted. The S_{d2} values of the two-, four-, and eight-dipole element array antennas are 2.8 mm, 2.3 mm, and 1.7 mm, respectively. When expressed in terms of wavelengths, they are $0.26\lambda_0$, $0.21\lambda_0$, and $0.16\lambda_0$, respectively. Table 1 shows the optimized design parameters of the single-printed dipole antenna and the array antennas with two, four, and eight-dipole elements in a series.

Fig. 4 shows the simulation results for the antenna with one-, two-, four-, and eight-dipole elements. Fig. 4(a) shows the four antennas' reflection coefficients. When compared to a single dipole antenna, the impedance bandwidth of the array, wherein

Table 1. Design parameters of antennas

Parameter	1-dipole	2-dipole	4-dipole	8-dipole
S_{d1} (mm)	2.8	3.2	3.2	2.8
S_{d2} (mm)	-	2.8	2.3	1.7
S_{d2} (λ_0)	-	0.26	0.21	0.16
L_q (mm)	1.4	1.8	2.0	0.6
W_q (mm)	0.3	1.0	0.8	0.3

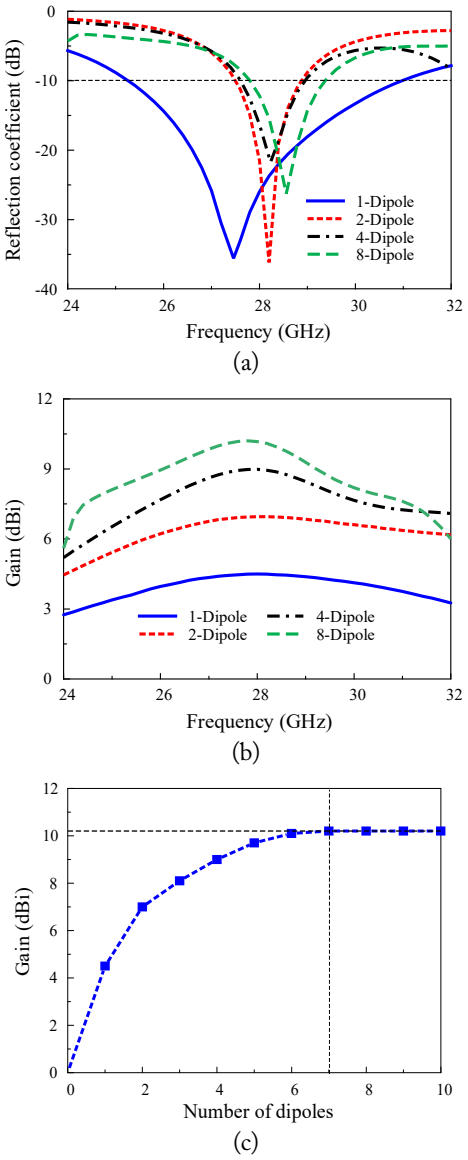

Fig. 4. Simulation results of one-, two-, four-, and eight-dipole antennas at 28 GHz: (a) reflection coefficient, (b) gain, and (c) gain with respect to the number of dipoles.

several dipoles of the same size are connected in a series, is reduced. The impedance bandwidths of the one-, two-, four-, and eight-dipole arrays are 25.6–31.0 GHz, 27.5–28.9 GHz, 27.6–28.9 GHz, and 27.8–29.3 GHz, respectively. Fig. 4(b) shows the gain characteristics of the antennas in the endfire direction. The gains at the center frequencies of the one-, two-, four-, and eight-dipole arrays are 4.5 dBi, 7.0 dBi, 9.0 dBi, and 10.2 dBi, respectively. For arrays with two or more dipoles, the 3-dB gain bandwidth gradually decreased as the number of dipoles increased. Fig. 4(c) shows the gains as the number of dipoles changed. The gain stopped increasing when the number of dipoles was greater than seven.

When the number of dipole elements forming the series-fed endfire array antenna is large, the phase constant (β) of the feedline connecting the dipole elements should be close to the wave

number of free space to obtain high gain [26]. Because the phase constant of the parallel strip line in this study is larger than the wave number of free space (k_o), the gain increment cannot be achieved when more than a certain number of dipole elements are used.

Fig. 5 shows the surface current distribution of an array antenna consisting of two-, four-, eight-, and twelve-dipole elements. Although the number of dipoles increases on the array antenna, the current is not concentrated on a specific dipole and is uniformly distributed. Fig. 6 shows the surface current vectors of the antennas with one-, two-, three-, and four-dipole elements. For the array antennas composed of one-, two-, and three-dipole elements, the phase difference of the current between the adjacent dipole elements is close to 180°. As a result, constructive interference occurs, which increases the gain of the array antenna in the endfire direction. However, the array antenna with four dipoles does not significantly increase the gain because the phase difference of the currents of the third and fourth dipoles is close to being in-phase. As the number of dipoles increases, the phase difference between the adjacent dipole elements becomes in-phase more frequently. Therefore, the gain does not increase when more than a certain number of dipole elements are used.

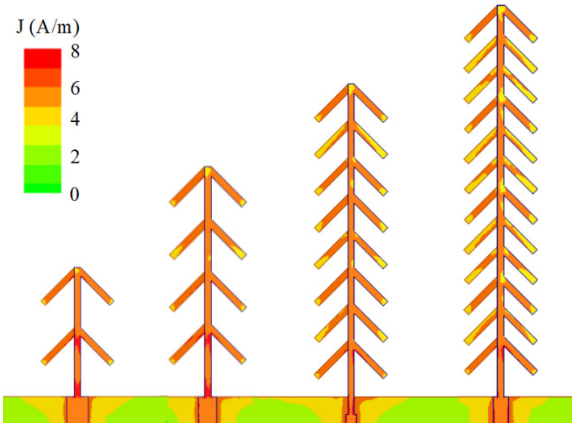

Fig. 5. Current distribution of the printed two-, four-, eight-, and twelve-element dipole array antennas.

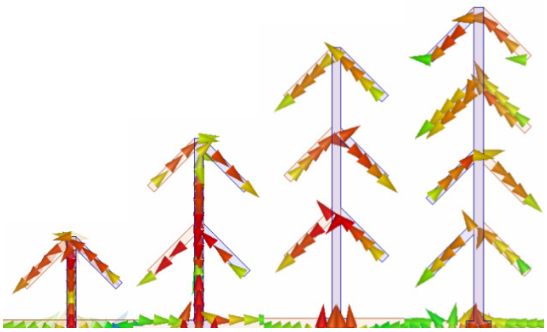

Fig. 6. Current vector of the printed one-, two, three-, and four-element dipole array antennas.

Fig. 7 shows the normalized radiation pattern at the center frequency of 28 GHz. As the number of dipoles increases, the HPBWs of the *xz*- and *yz*-planes of the radiation patterns became similar. As the number of dipoles increases, the directivity increases, and the influence of the reflected power in the truncated ground plane is reduced. Therefore, the radiation pattern of the *xz*- and *yz*-planes presented more symmetrically. For four

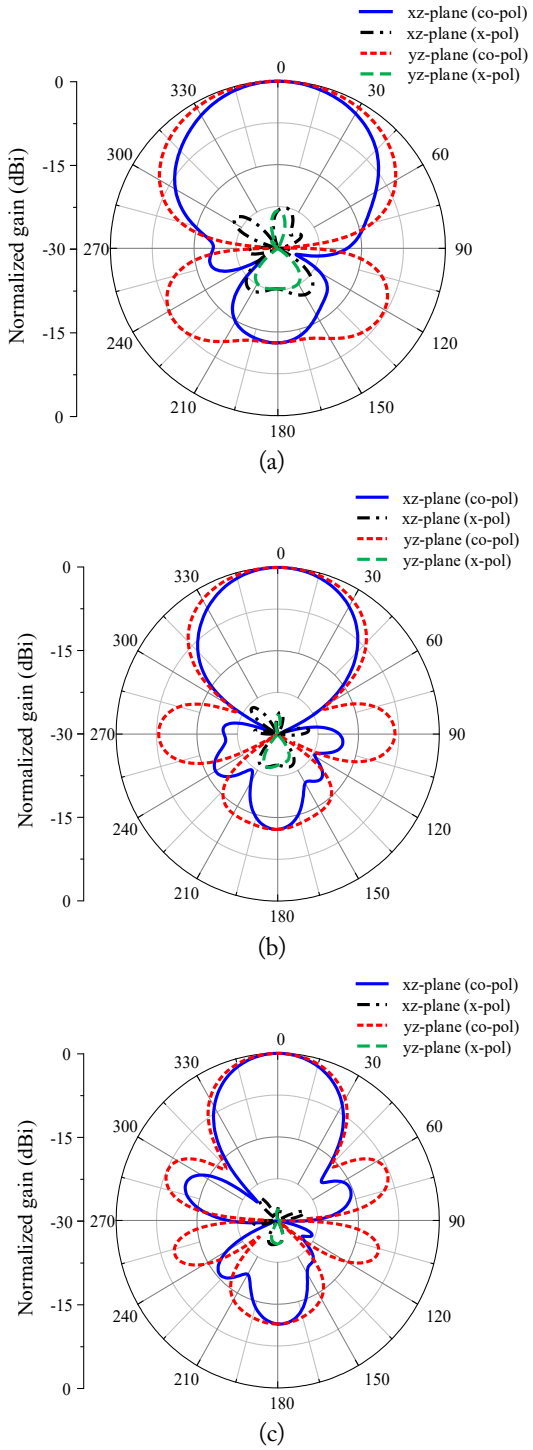

Fig. 7. Normalized radiation pattern of the dipole array antennas at 28 GHz: (a) two-dipole, (b) four-dipole, and (c) eight-dipole.

Table 2. Radiation pattern characteristics

Characteristic	1-dipole	2-dipole	4-dipole	8-dipole
-10 dB IBW (GHz)	5.4	1.4	1.3	1.5
3-dB gain BW (GHz)	14.8	14.6	9.0	7.1
Gain at 28 GHz (dBi)	4.5	7.0	9.0	10.2
xz-plane HPBW (°)	62.6	68.9	54.6	43.6
xz-plane $HPBW_L$ (°)	34.0	33.3	26.5	21.5
xz-plane $HPBW_R$ (°)	28.6	35.7	28.1	22.3
yz-plane HPBW (°)	219.3	97.7	68.7	49.8
x-pol level (dB)	-15.1	-16.3	-17.6	-18.6

or more dipoles connected in a series, the HPBW difference between the *xz*- and *yz*-planes was significantly reduced to less than 20°. The HPBW differences between the *xz*- and *yz*-planes of the designed one-, two-, four-, and eight-dipole arrays were 156.7°, 28.8°, 14.1°, and 5.3°, respectively. In the *xz*-plane radiation pattern, the difference between $HPBW_R$ and $HPBW_L$ was less than 2°, and more symmetrical radiation patterns were obtained. The differences between $HPBW_L$ and $HPBW_R$ for the *xz*-plane of one-, two-, four-, and eight-dipole arrays were 5.4°, 2.4°, 1.6°, and 0.8°, respectively. For multiple dipoles connected in a series, the cross-polarization components in each dipole cancelled each other out. Therefore, the cross-polarization level was lower than in a single dipole antenna. The characteristics of the one-, two-, four-, and eight-dipole arrays are shown in Table 2.

IV. Measurement Results

The printed angled dipole array antenna with four-dipole elements connected in a series was fabricated, and the reflection coefficient, gain, and radiation pattern were measured. Fig. 8 is a photograph of the fabricated antenna. The Rohde & Schwarz ZVA 67 VNA was used to measure the reflection coefficient, and MTG Corp.'s anechoic chamber was used to measure the radiation pattern. Fig. 9 shows the simulated and measured results of the fabricated antenna. The measured –10 dB impedance bandwidth of the four-dipole array antenna is 27.2–29.0 GHz. The measured impedance bandwidth is nearly the same as the simulated result of 27.6–28.9 GHz. The measured gain at the center frequency of 28 GHz is 9.0 dBi, and the HPBWs in the *xz*- and *yz*-planes are 54.6° and 68.7°, respectively. The 3-dB gain bandwidth of the array antenna is 23.6–33.5 GHz.

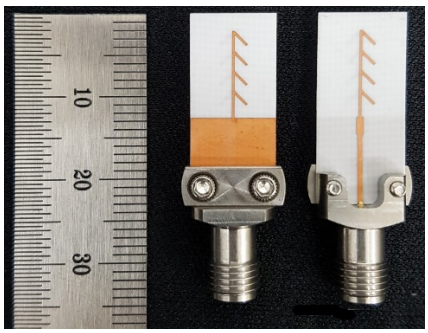

Fig. 8. Photograph of the printed four-element dipole array antenna.

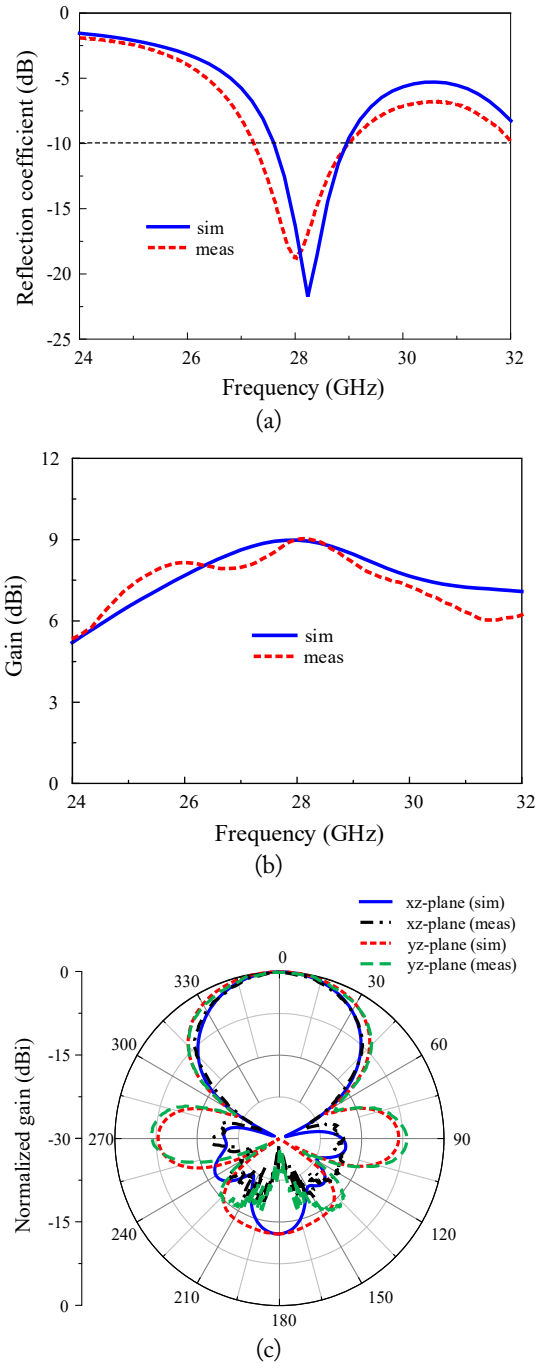

Fig. 9. Comparison between the measured and simulated results: (a) reflection coefficient, (b) gain, and (c) radiation pattern at 28 GHz.

The measured gain at 28 GHz is almost the same as the simulated results, and the HPBWs in the *xz*- and *yz*-planes are 56.1° and 68.5°, respectively. The measured 3-dB gain band-

width is 24.3–32.2 GHz, which is approximately 1.0 GHz narrower than the simulated results.

V. Conclusion

This paper demonstrated that when using multiple angled dipoles, series-fed array antennas can achieve higher gains, more symmetrical radiation patterns, and lower cross-polarization levels than single angled dipole antennas. We designed two-, four-, and eight-dipoles in a series, and the gains at the center frequency of the array antennas were 7.0 dBi, 9.0 dBi, and 10.2 dBi, respectively. The single angled printed dipole exhibited a large HPBW difference of 156.7° between the *xz*- and *yz*-planes, and the radiation pattern of the *xz*-plane was asymmetrical. By connecting four or more dipoles in a series, the HPBW difference between the *xz*- and *yz*-planes was greatly reduced. In addition, the radiation pattern of the *xz*-plane presented symmetrically. Therefore, the proposed structure presented a high gain and symmetrical radiation pattern. It was also lighter and cheaper than antenna structures using metal cavities and significantly easier to optimize than quasi-Yagi antennas using several directors. Therefore, the proposed antenna could prove useful for 5G communication systems.

This work was supported in part by the National Research Foundation (NRF) of Korea grant funded by the Korean government (MSIT) (No. 2018R1D1A1A02086071); in part by the "Human Resources Program in Energy Technology" of the Korea Institute of Energy Technology Evaluation and Planning (KETEP)-granted financial resources from the Ministry of Trade Industry & Energy, Republic of Korea (No. 20184030292220); and in part by the GRRC program of Gyeonggi province (No. GRRC-AJOU-2016B01, Photonics-Medical Convergence Technology Research Center).

References

[1] T. S. Rappaport, S. Sun, R. Mayzus, H. Zhao, Y. Azar, K. Wang, et al., "Millimeter wave mobile communications for 5G cellular: it will work!," *IEEE Access*, vol. 1, pp. 335-349, 2013.

[2] W. Roh, J. Y. Seol, J. Park, B. Lee, J. Lee, Y. Kim, J. Cho, K. Cheun, and F. Aryanfar, "Millimeter-wave beamforming as an enabling technology for 5G cellular communications: theoretical feasibility and prototype results," *IEEE Communications Magazine*, vol. 52, no. 2, pp. 106-113, 2014.

[3] J. G. Andrews, S. Buzzi, W. Choi, S. V. Hanly, A. Lozano, A. C. Soong, and J. C. Zhang, "What will 5G be?," *IEEE Journal on Selected Areas in Communications*, vol. 32, no. 6, pp. 1065-1082, 2014.

[4] M. Agiwal, A. Roy, and N. Saxena, "Next generation 5G wireless networks: a comprehensive survey," *IEEE Communications Surveys & Tutorials*, vol. 18, no. 3, pp. 1617-1655, 2016.

[5] S. X. Ta, H. Choo, and I. Park, "Broadband printed-dipole antenna and its arrays for 5G applications," *IEEE Antennas and Wireless Propagation Letters*, vol. 16, pp. 2183-2186, 2017.

[6] Y. H. Suh and K. Chang, "A new millimeter-wave printed dipole phased array antenna using microstrip-fed coplanar stripline Tee junctions," *IEEE Transactions on Antennas and Propagation*, vol. 52, no. 8, pp. 2019-2026, 2004.

[7] R. A. Alhalabi and G. M. Rebeiz, "High-efficiency angled-dipole antennas for millimeter-wave phased array applications," *IEEE Transactions on Antennas and Propagation*, vol. 56, no. 10, pp. 3136-3142, 2008.

[8] R. Li, T. Wu, B. Pan, K. Lim, J. Laskar, and M. M. Tentzeris, "Equivalent-circuit analysis of a broadband printed dipole with adjusted integrated balun and an array for base station applications," *IEEE Transactions on Antennas and Propagation*, vol. 57, no. 7, pp. 2180-2184, 2009.

[9] S. X. Ta and I. Park, "Broadband printed-dipole antennas for millimeter-wave applications," in *Proceedings of 2017 IEEE Radio and Wireless Symposium (RWS)*, Phoenix, AZ, 2017, pp. 65-67.

[10] P. Hannan, "The element-gain paradox for a phased-array antenna," *IEEE Transactions on Antennas and Propagation*, vol. 12, no. 4, pp. 423-433, 1964.

[11] D. M. Pozar, "The active element pattern," *IEEE Transactions on Antennas and Propagation*, vol. 42, no. 8, pp. 1176-1178, 1994.

[12] D. M. Pozar, "A relation between the active input impedance and the active element pattern of a phased array," *IEEE Transactions on Antennas and Propagation*, vol. 51, no. 9, pp. 2486-2489, 2003.

[13] H. Wang, K. E. Kedze, and I. Park, "A high gain and wideband series-fed angled printed dipole array antenna," *IEEE Transactions on Antennas and Propagation*, vol. 68, no. 7, pp. 5708-5713, 2020.

[14] S. X. Ta and I. Park, "Cavity-backed angled-dipole antennas for millimeter-wave wireless applications," *International Journal of Antennas and Propagation*, vol. 2016, article no. 5083807, 2016.

[15] Z. Tu, D. F. Zhou, G. Q. Zhang, F. Xing, X. Lei, and D. W. Zhang, "A wideband cavity-backed elliptical printed dipole antenna with enhanced radiation patterns," *IEEE Antennas and Wireless Propagation Letters*, vol. 12, pp. 1610-1613, 2013.

[16] S. X. Ta and I. Park, "A cavity-backed angled-dipole anten-

na array for low millimeter-wave bands," in *Proceedings of 2016 International Workshop on Antenna Technology (iWAT)*, Cocoa Beach, FL, 2016, pp. 57-59.

[17] S. X. Ta, B. Kim, H. Choo, and I. Park, "Wideband quasi-Yagi antenna fed by microstrip-to-slotline transition," *Microwave and Optical Technology Letters*, vol. 54, no. 1, pp. 150-153, 2012.

[18] G. Zhai, Y. Cheng, Q. Yin, S. Zhu, and J. Gao, "Gain enhancement of printed log-periodic dipole array antenna using director cell," *IEEE Transactions on Antennas and Propagation*, vol. 62, no. 11, pp. 5915-5919, 2014.

[19] X. R. Li, M. Ye, and Q. X. Chu, "Novel high gain printed log-periodic dipole antenna," in *Proceedings of 2016 IEEE International Symposium on Antennas and Propagation (APSURSI)*, Fajardo, Puerto Rico, 2016, pp. 1647-1648.

[20] Q. X. Chu, X. R. Li, and M. Ye, "High-gain printed log-periodic dipole array antenna with parasitic cell for 5G communication," *IEEE Transactions on Antennas and Propagation*, vol. 65, no. 12, pp. 6338-6344, 2017.

[21] L. Lu, K. Ma, F. Meng, and K. S. Yeo, "Design of a 60-GHz Quasi-Yagi antenna with novel ladder-like directors for gain and bandwidth enhancements," *IEEE Antennas and Wireless Propagation Letters*, vol. 15, pp. 682-685, 2016.

[22] S. X. Ta, J. J. Han, H. Choo, and I. Park, "High gain 60 GHz band printed quasi-Yagi antenna using a novel microstrip-slotline transition feed," in *Proceedings of 2012 5th Global Symposium on Millimeter-Waves*, Harbin, China, 2012, pp. 1-4.

[23] Y. He, K. Ma, N. Yan, Y. Wang, and H. Zhang, "A cavity-backed endfire dipole antenna array using substrate-integrated suspended line technology for 24 GHz band applications," *IEEE Transactions on Antennas and Propagation*, vol. 66, no. 9, pp. 4678-4686, 2018.

[24] N. V. Venkatarayalu and T. Ray, "Optimum design of Yagi-Uda antennas using computational intelligence," *IEEE Transactions on Antennas and Propagation*, vol. 52, no. 7, pp. 1811-1818, 2004.

[25] U. Singh, H. Kumar, and T. S. Kamal, "Design of Yagi-Uda antenna using biogeography based optimization," *IEEE Transactions on Antennas and Propagation*, vol. 58, no. 10, pp. 3375-3379, 2010.

[26] W. W. Hansen and J. R. Woodyard, "A new principle in directional antenna design," *Proceedings of the Institute of Radio Engineers*, vol. 26, no. 3, pp. 333-345, 1938.

Heesu Wang

received his B.S. and M.S. degrees in Electrical and Computer Engineering from Ajou University, Suwon, Korea, in 2018 and 2020, respectively. He is currently studying for his Ph.D. at the Department of Electrical and Computer Engineering at Ajou University, Suwon, Korea. His research interests include the design of patch antennas, printed antennas, small antennas, and metasurface antennas for various wireless communication applications.

Ikmo Park

received his B.S. degree in Electrical Engineering from the State University of New York at Stony Brook and his M.S. and Ph.D. degrees in Electrical Engineering from the University of Illinois at Urbana-Champaign. He joined the Department of Electrical and Computer Engineering at Ajou University, Suwon, Korea, in 1996. He has authored and co-authored over 300 technical journals and conference papers. He also holds over 40 domestic and international patents. He served as a Chair of the Department of Electrical and Computer Engineering at Ajou University, and he is a member of the Board of Directors at the Korea Institute of Electromagnetic Engineering and Science (KIEES). He serves as the Editor-in-Chief for the Journal of KIEES, an Editorial Board member for the International Journal of Antennas and Propagation, an Editorial Board member for MDPI's Electronics, and an Associate Editor for the IET's Electronics Letters. He has also served as an Editorial Board member of the Journal of Electromagnetic Engineering and Science. He currently serves as chair, organizer, and member of program committees for various conferences, workshops, and short courses in electromagnetic-related topics. His present research interests include the design and analysis of microwave, millimeter-wave, terahertz wave, and nano-structured antennas with metamaterials and metasurfaces.

JOURNAL OF ELECTROMAGNETIC ENGINEERING AND SCIENCE, VOL. 20, NO. 3, 190~198, JUL. 2020

https://doi.org/10.26866/jees.2020.20.3.190
ISSN 2671-7263 (Online) · ISSN 2671-7255 (Print)

Modeling of Monopulse Radar Signals Reflected from Ground Clutter in a Time Domain Considering Doppler Effects

Jeong-Hun Nam[1] · Jae-Won Rim[1] · Hyunsoo Lee[2] · Il-Seuk Koh[1,*] · Jong-Hwa Song[3]

Abstract

To evaluate the performance of a monopulse radar system, it is necessary to accurately model radar return signals from the ground surface in a time domain. In this paper, we propose a numerical method to model these return signals including radar radio frequency specifications, such as the pulse repetition interval, frequency, and polarization, as well as the antenna geometry, the ground clutter backscattering characteristics, and so on. The Doppler effect is also incorporated into the signal generation scheme because of the dynamics of the platform/clutter and the antenna orientation. The Doppler frequency shift caused by the ground clutter is modeled by employing the time correlation of the received signals. In some scenarios, the monopulse signals are generated and numerically examined. For real radar application, the effect of the platform's roll stabilization on the monopulse signals is investigated based on the proposed signal generation scheme.

Key Words: Doppler Effect, Ground Clutter, Monopulse Radar, Radar Return Signal.

I. Introduction

The radar system mounted on an airborne platform operates in an air-to-ground mode as well as in an air-to-air mode [1]. For example, the AN/APG-77 is the F-22's primary sensor that provides several functions, including terrain mapping, ground-moving target searching/tracking, and air-to-ground ranging (AGR) [2]. The AN/APG-77 radar adopts a monopulse system with an active electronically scanned array (AESA) antenna. The amplitude- or phase-comparison monopulse radar transmits one pulse and then receives three monopulse channels as the sum, elevation, and azimuth difference channels. The channels are calculated as three weighted sums of partial signals received by each antenna element in a receiving mode [3, 4]. Also, in the air-to-ground mode, the clutter backscattering may become much stronger than that of the air-to-air mode, and such strong backscattering can seriously degrade the radar's performance [5].

The radar echo signals are determined by basic radar radio frequency (RF) specification, such as frequency and pulse repetition interval (PRI), etc., and the radar's operation environment, such as platform dynamics, ground clutter type, antenna footprint on the ground plane (mainly determined by the platform orientation), and the ASEA antenna's beam illumination. Due

Manuscript received May 31, 2019 ; Revised October 1, 2019 ; Accepted May 12, 2020. (ID No. 20190531-044J)
[1]Deparment of Electronic Engineering, Inha University, Incheon, Korea.
[2]Agency for Defense Development, Daejeon, Korea.
[3]Hanwha Systems, Yongin, Korea.
[*]Corresponding Author: Il-Suek Koh (e-mail: ikoh@inha.ac.kr)

to the dynamics of the platform and ground clutter, the received signal is slightly distorted, which can be modeled by considering the Doppler frequency shift. Since the range-Doppler (RD) map clearly shows the Doppler frequencies, RD-processing is crucial in many radar applications, including a synthetic aperture radar (SAR) [6] and a moving target indicator [7]. Hence, the modeling of the radar echo signal in a time-domain is required when considering the effect of all the aforementioned factor's needed to generate an accurate RD map.

Much attention has been paid to the backscattering determined by the ground clutter, which can be used to determine the mean power received by the radar. Since the clutter signal is a typical random signal, several probability density functions (PDF) have been used, such as Gaussian, Weibull, K-distribution, and so on [8]. Except in the case of sea clutter, the Gaussian distribution is a simple and accurate way to develop a time-domain signal model [9]. The correlated Gaussian random signal can be generated in a relatively easy and accurate manner [10, 11], and is a conventional method for incorporating the Doppler effect of the clutter into the modeling of pulse-Doppler radar signals [12].

In Section II, we address the proposed modeling approach of the radar echo signal for a phase-comparison monopulse radar [3], considering the Doppler effects due to the dynamics of the platform and the ground clutter simultaneously. Section III presents the numerical results for operating scenarios that consider the platform dynamics and antenna beam steering direction, etc. Finally, an AGR simulation is examined for a real-world application.

II. Modeling Method

1. Scenario and Coordinate Systems

The dynamic scenario for the air-to-ground radar operation is shown in Fig. 1. An airborne platform moves at a constant velocity, $\vec{v} = v_x\hat{x} + v_y\hat{y} + v_z\hat{z}$, while repeatedly transmitting a signal to the ground surface at every PRI. Given that an antenna beam is illuminated toward the line of sight (LOS), the return signals may be reflected primarily from the main-lobe beam projected on the ground that is truncated by the half-power beam width (HPBW) for a numerical simulation. The return signals of multiple pulses are aligned along the fast time (t) and the slow time (η), generating 2D raw signals [13]. The mean reflection power from the ground clutter inside the projected main-lobe beam can be calculated using the backscattering coefficient [14]. Here, we assume the ground clutter to be a rough surface [15] for which a theoretical backscattering model, such as an Integral Equation Model (IEM) may be accurate [16] for two co-polarized scatterings. The return signal can be assumed to be a Gaussian random signal whose backscattering coefficient

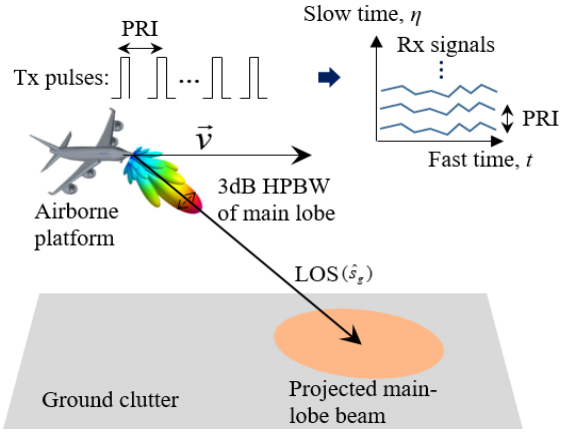

Fig. 1. Dynamics scenario for air-to-ground radar.

is used as a variance of the random signal. The movement of the platform and ground clutter can be modeled using the Doppler frequency shift in the received signals.

Note that the shape of the projected main-lobe beam in Fig. 1 is dependent on the orientations of the platform and the antenna. Hence, the coordinate systems of the platform and the antenna are important. The relationship between the global and local coordinate systems of the platform is shown in Fig. 2. The parameters related to the coordinate systems in Fig. 2 are summarized as follows:

$(\hat{x}_p, \hat{y}_p, \hat{z}_p)$:	Orientation vector of the platform in its local coordinates,
$(\hat{x}_g, \hat{y}_g, \hat{z}_g)$:	Orientation vector of the platform in the global coordinates,
$\hat{s}_l$ and $\hat{s}_g$:	LOS vectors of the antenna in the platform's local coordinates and in the global coordinates, respectively,
θ and φ:	Elevation and azimuth angles in the antenna's local coordinates,
θ_r, θ_y, and θ_p:	Roll, yaw, and pitch angles in the platform's local coordinates.

As the local coordinate of the antenna coincides with that of the platform, $\hat{s}_l$ is defined as

$$\hat{s}_l = \sin\theta\cos\varphi\hat{x}_p + \sin\theta\sin\varphi\hat{y}_p + \cos\theta\hat{z}_p .$$

Considering the dynamics of the platform, the LOS vector of the antenna in the global coordinates is rotated depending on θ_r, θ_y, and θ_p, as seen in Fig. 2. Based on θ_r, θ_y, and θ_p, the antenna's LOS vector in the global coordinate, $\hat{s}_g$, is represented as

$$\hat{s}_g = R_x(\theta_r)R_y(\theta_y)R_z(\theta_p)\hat{s}_l$$

where R_x, R_y, and R_z are rotation matrices along the global x, y, and z axes, respectively [17]. In Fig. 3, the signs of the antenna weights for three monopulse channels are defined. The V and W

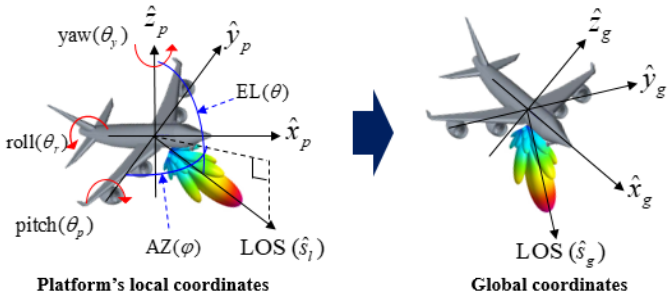

Fig. 2. Local and global coordinate systems of the platform and antenna.

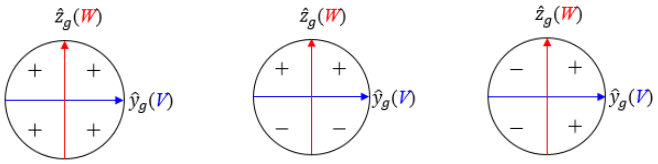

Fig. 3. Sign of antenna weight for phase-comparison monopulse sum and difference patterns: (a) sum (w^{Σ}), (b) elevation difference ($w^{\Delta EL}$), and (c) azimuth difference ($w^{\Delta AZ}$).

axes of the monopulse radar coincide with the y_g and z_g axes in the global coordinates, respectively [18]. In Figs. 4 and 5, the projected main-lobe beam and the *V* and *W* axes are found on the ground plane using a ray-tracing technique: first, the normal vector of the antenna's *VW* plane is aligned in the direction of $\hat{s}_g$. Then, rays are launched from the antenna's center to the rim of the HPBW of the antenna pattern or the *V* and *W* lines in the antenna's *VW* plane. Finally, the intercept points between the rays and the ground plane are calculated.

The simulation parameters are presented in Table 1. In Fig. 4, the platform orientation and antenna beam steering are given as $\theta_r = 0°$, $\theta_y = 0°$, $\theta_p = 0°$, and $\theta = 105°$, $\varphi = 0°$–$60°$, respectively. As observed in Fig. 4(a), it is well-known that as the azimuth angle (φ) increases, the HPBW of the *V* axis broadens while the HPBW of the *W* axis remains constant [19]. The simulation and theoretical estimations for the HPBW of the *V* and *W* axes on the ground are compared in Fig. 4(b), where an excellent agreement can be observed. As shown in Fig. 5(a), if the platform is rolled, the monopulse axes rotate by a small angle, γ, with respect to the major axes parallel to the

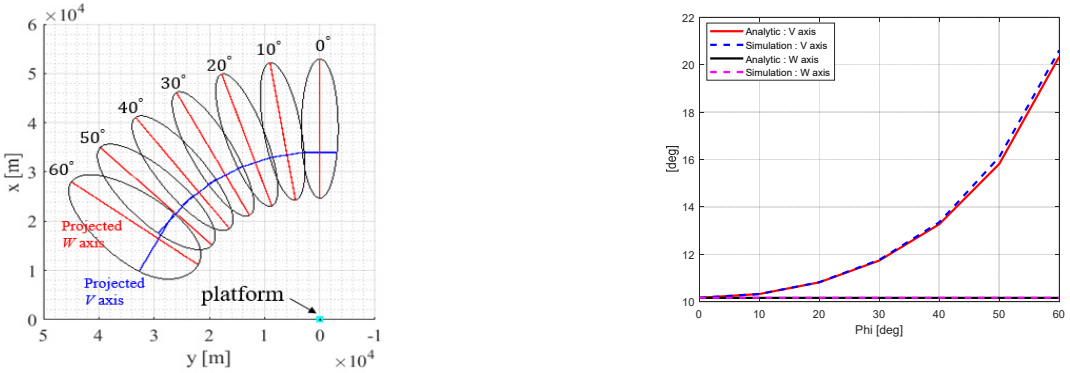

(a) (b)

Fig. 4. Simulation results according to the azimuth angle φ. (a) Projected antenna footprint and *V* and *W* axes, and (b) analytic and simulation results of the *V* and *W* axis widths.

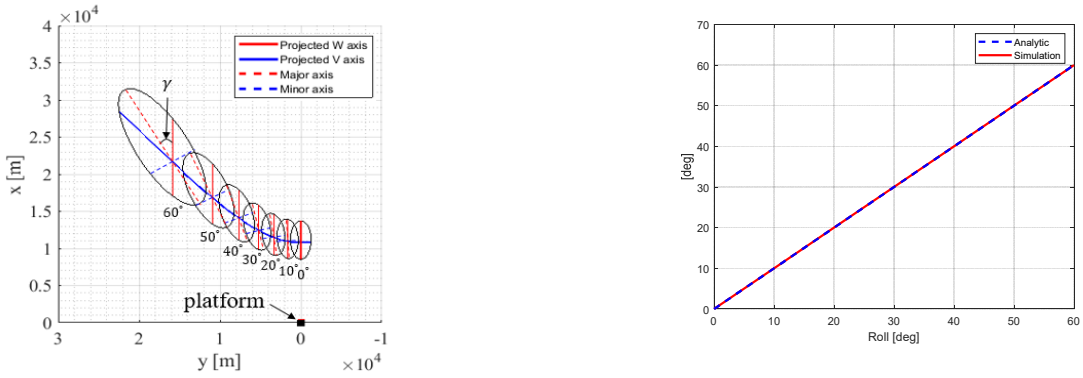

(a) (b)

Fig. 5. Simulation results according to the rolling angle θ_r. (a) Projected antenna footprint and the *V* and *W* axes, and (b) analytic and simulation results of γ.

Table 1. Simulation parameters

Parameter	Value
Polarization	VV
Frequency	X band
Number of pulses	50
Platform height (feet)	30,000
Platform speed (m/s)	180
PRF (Hz)	1,670
Rectangle size (m)	30 × 30
Number of antenna array	
V axis	20
W axis	20
Antenna array spacing	
V axis	λ / 4
W axis	λ / 4
Correlation function	Gaussian [23]
Correlation length (cm)	8.4 [5]
rms height (cm)	0.4 [5]
Dielectric constant	15.4 – *j*2.15 [5]

LOS vector [14]. The estimations of γ by simulation and by the known theoretical formula [14] are in excellent agreement, as seen in Fig. 5(b). For this calculation, the platform orientation angles are assumed as $\theta_r = 0^o$–60^o, $\theta_y = 0^o$, and $\theta_p = 0^o$. The beam illumination angles of the antenna are fixed at $\theta = 130^o$ and $\varphi = 0^o$. Therefore, the projected antenna footprint on the ground plane can be accurately found for any platform and antenna orientation.

2. Radar Return Signal in a Time-Domain

The configuration of the signal transmission/reception at the radar and the corresponding projected main-lobe beam needed to calculate the radar return signals in a time-domain are shown in Fig. 6. First, the projected main-lobe beam is divided into uniform rectangular grids (cells) based on a preset range resolution. The range resolution is determined using the sampling time interval of the fast time (*t*) [13]. The projected area can be approximated as an ellipse [20] whose major axis is parallel to

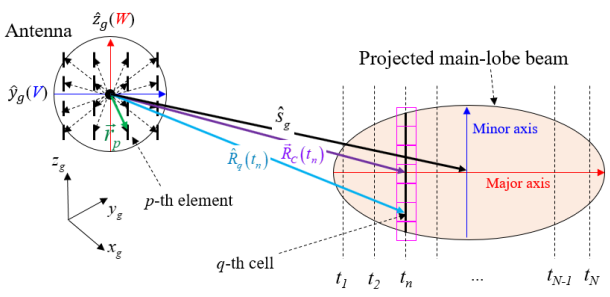

Fig. 6. Signal transmission/reception of antenna to/from surface-projected main-lobe beam.

the LOS direction from the radar to the center of the ellipse. Since the minor axis is perpendicular to the major axis, the ellipse can be uniformly discretized using a rectangle along the major and minor axes, as seen in Fig. 6. The ellipse is located in the far-field region from the platform, and so the return signals from the cells along a line parallel to the minor axis are coherently added into one time-domain response in each sampling time (range bin). The received monopulse signals from each *q*-th ground cell is represented as

$$\Psi_q^{\Sigma}(t_n,\eta) = \frac{AF_{\Sigma}AF_{\Sigma}G^2\sigma_q(t_n,\eta)A(q)}{R_c^2(t_n,\eta)}\delta\left[t-\frac{2R_c(t_n,\eta)}{c}\right],$$
$$\Psi_q^{\Delta EL}(t_n,\eta) = \frac{AF_{\Sigma}AF_{\Delta EL}G^2\sigma_q(t_n,\eta)A(q)}{R_c^2(t_n,\eta)}\delta\left[t-\frac{2R_c(t_n,\eta)}{c}\right],$$
$$\Psi_q^{\Delta AZ}(t_n,\eta) = \frac{AF_{\Sigma}AF_{\Delta AZ}G^2\sigma_q(t_n,\eta)A(q)}{R_c^2(t_n,\eta)}\delta\left[t-\frac{2R_c(t_n,\eta)}{c}\right], \quad (1)$$

where σ_q and $A(q)$ are the backscattering coefficient and area of the *q*-th cell, respectively, *G* is the gain of the antenna element, and $\delta(\cdot)$ is the Dirac delta function. Note that the *q*-th cell belongs to the sampling time (t_n), as shown in Fig. 6. The sampling time can be computed simply as $t_n = 2R_c(t_n,\eta)/c$, where *c* is the speed of light. $R_c(t_n,\eta)$ is the distance from the platform to the *q*-th cells corresponding to the major axis, as shown in Fig. 6. AF_{Σ}, $AF_{\Delta EL}$, and $AF_{\Delta AZ}$ are the array factors of the antenna for the sum, elevation difference, azimuth difference channels, respectively, on the *q*-th cell, which is given as

$$AF_{\Sigma} = \sum_{p=1}^{N_p} w_p^{\Sigma}\exp\left(-jk_0[\hat{R}_q(t_n,\eta)-\hat{s}_g]\cdot\vec{r}_p\right),$$
$$AF_{\Delta EL} = \sum_{p=1}^{N_p} w_p^{\Delta EL}\exp\left(-jk_0[\hat{R}_q(t_n,\eta)-\hat{s}_g]\cdot\vec{r}_p\right),$$
$$AF_{\Delta AZ} = \sum_{p=1}^{N_p} w_p^{\Delta AZ}\exp\left(-jk_0[\hat{R}_q(t_n,\eta)-\hat{s}_g]\cdot\vec{r}_p\right), \quad (2)$$

where N_p is the number of the antenna elements and k_0 is the free-space propagation constant. $\hat{R}_q(t_n,\eta)$ is the direction vector from the phase center of the antenna to the *q*-th cell at $t = t_n$. $\vec{r}_p$ is the displacement vector from the phase center of the antenna to the *p*-th antenna element. w_p^{Σ}, $w_p^{\Delta EL}$, and $w_p^{\Delta AZ}$ are the weight of the *p*-th antenna element for three monopulse channels, as seen in Fig. 3. In monopulse systems, a sum channel is used at the transmitting (Tx) mode and three channels, such as the sum, elevation difference, and azimuth difference channels, are employed in the receiving (Rx) mode [4]. The total return signals sampled at $t=t_n$ are a summation of the return signal from specific ground cells. The calculated cells at $t=t_n$ are mathematically denoted as $Cell(q) \in t_n$. Adding all responses from the ground cells belonging to

$Cell(q) \in t_n$, three monopulse signals can be formulated without the consideration of the Doppler effects as

$$\Psi_{\Sigma,\Delta EL,\Delta AZ}(t_n,\eta) = \sum_{Cell(q)\in t_n}^{Terrain} \Psi_q^{\Sigma,\Delta EL,\Delta AZ}(t_n,\eta) \tag{3}$$

where Ψ_Σ, $\Psi_{\Delta EL}$, and $\Psi_{\Delta AZ}$ are the total radar return signals for the monopulse sum, elevation difference, and aizumuth difference channels, respectively.

In Fig. 7, the return signal is calculated from a flat ground whose backscattering is assumed to be a constant at a slow time, $\eta = 0$. In Fig. 7(a) and 7(b), the platform orientation and antenna beam steering are assumed as $\theta_r = 60°$, $\theta_y = 0°$, $\theta_p = 0°$, and $\theta = 130°$, $\varphi = 0°$, respectively. The "/w γ" and "/wo γ" indicate "with γ-correction" and "without γ-correction", respectively. In Fig. 7(a), the roll angle is not zero, so it can be observed that the null of $\Psi_{\Delta EL}$ locates off the boresight and the monopulse response of $\Psi_{\Delta AZ}$ is not zero. But, as shown in Fig. 7(b), when the return signal is compensated with the known γ-correction scheme, the null point of $\Psi_{\Delta EL}$ is shifted to the boresight and the level of $\Psi_{\Delta AZ}$ is decreased to almost zero [4]. The exact and simulated monopulse ratios, Im($\Psi_{\Delta EL}$)/Re(Ψ_Σ), are compared in Fig. 7(c) for $\theta_r = 0°$ [14]. The proposed signal-generation scheme can provide an accurate monopulse ratio. The Re(Ψ_Σ) is approximately 2×10^{-19}, which is essentially zero. Here, Re(z) and Im(z) are the real and imaginary parts of z, respectively. Therefore, the generated time-domain signal can provide accurate monopulse signal behaviors.

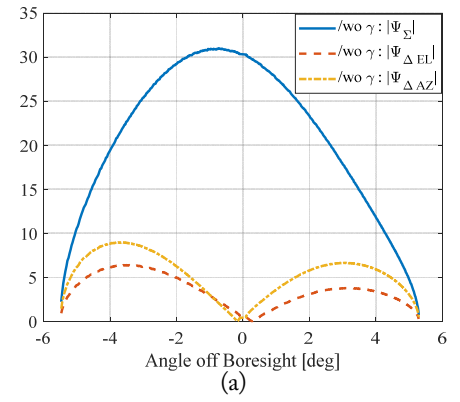

(a)

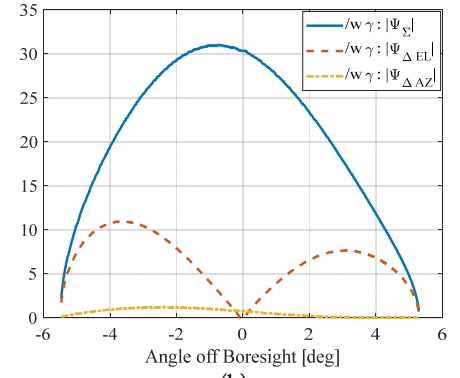

(b)

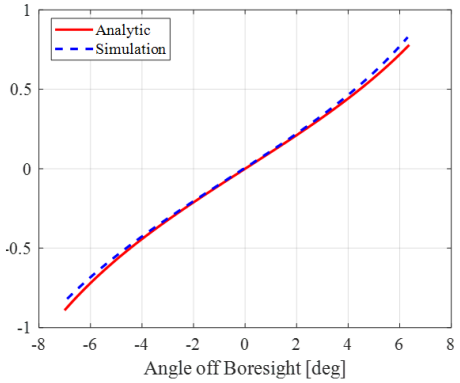

(c)

Fig. 7. Monopulse response vs angle-off boresight: (a) monopulse signal before γ-correction, (b) monopulse signal after γ-correction, and (c) monopulse ratio of Im($\Psi_{\Delta EL}$) to Re(Ψ_Σ).

3. Doppler Effects

There are two dominant Doppler effects in the dynamic situation considered here because of to the movements of the platform and ground clutter. The Doppler shift of the clutter can be included simply by generating the correlated Gaussian random variable of $\sigma_q(t_n,\eta)$ in the slow time in (1) for a proper correlation function, such as the Gaussian and exponential functions. Here, the Cholesky decomposition method is used [11]. The correlation time (t_c) is inversely proportional to the Doppler frequency of the ground clutter [21, 22]. After computing (1) with the correlated $\sigma_q(t_n,\eta)$ along the slow time, the Doppler shift due to the platform dynamic is considered. The time-dependent distance between the platform and the q-th cell is expressed at the slow time (η_m) as

$$R_q(t_n,\eta_m) = \sqrt{\left[x_f + v_x(t_n+\eta_m) - x_q\right]^2 + \left[y_f + v_y(t_n+\eta_m) - y_q\right]^2 + \left[z_f + v_z(t_n+\eta_m) - z_q\right]^2} \tag{4}$$

where (x_f, y_f, z_f) and (x_q, y_q, z_q) are the coordinates of the platform and the center of the q-th cell at $(t = 0, \eta = 0)$ of the global coordinates, respectively. By using the Taylor series expansion, the Doppler frequencies along the fast-time, f_{D,t_n}, and slow-time, f_{D,η_m} axes, can be formulated as

$$f_{D,t_n} = \frac{-\vec{R}_q(0,\eta_m)\cdot\vec{v}}{R_q(0,\eta_m)\lambda_0}, f_{D,\eta_m} = \frac{-\vec{R}_q(0,0)\cdot\vec{v}}{R_q(0,0)\lambda_0} \tag{5}$$

where λ_0 is the free-space wavelength. Finally, the total return signal, including the Doppler effect due to platform movement, is given as

$$\Psi_{\Sigma,\Delta EL,\Delta AZ}(t_n,\eta_m) = \sum_{Cell(q)\in t_n}^{Terrain} \begin{bmatrix} \Psi_q^{\Sigma,\Delta EL,\Delta AZ}(t_n,\eta)\times \\ \exp(-j2\pi f_{D,t_n} t_n)\times \\ \exp(-j2\pi f_{D,\eta_m}\eta_m) \end{bmatrix}. \tag{6}$$

If two Doppler effects are considered at the same time, it is physically expected that the correlation time of the generated signal may be similar to the shorter one between the correlation times due to the platform and clutter dynamics.

III. Simulation Results

The simulation parameters are summarized in Table 1. The parameters of correlation length, root mean square (RMS), and dielectric constant of the rough surface are found in [5]. The pulse repetition frequency (PRF) is the reciprocal of PRI. A complete signal generation is considered, including two Doppler effects. For the rest of the simulations, the platform orientation and antenna beam steering are set as $\theta_r = 45^o$, $\theta_y = 0^o$, $\theta_p = 0^o$, and $\theta = 130^o$, $\varphi = 0^o$, respectively. In Fig. 8, the RD maps are shown for the sum and elevation difference signals. The RD map is calculated by taking the fast Fourier transform (FFT) along the slow-time axis, which clearly shows the signal Doppler frequencies. The correlation time of the clutter is assumed as 0.03 seconds for an X-band ground clutter [25]. The Doppler frequency can be exactly computed as 9,192.5 Hz at the center of the projected ellipse. The signal Doppler frequencies on the projected antenna footprint distributes over the wrapped Doppler frequency range $(-800 < f_D < -700) \bigcup (344.6 < f_D < 800)$ [19]. Hence, the correct Doppler frequency generation is observed in Fig. 8. In Fig. 8(b), the null of the elevation signal can be observed. In the Tx mode, only the sum pattern is transmitted, and so the Doppler frequency distribution of the difference pattern is similar to that of the sum pattern. Over the projected antenna footprint on the ground, the Doppler frequencies exit over a 500-Hz band, which indicates that the 500-Hz frequency band is generated due to the platform dynamics. Hence, the correlation time of the return signal due to the platform movement is around $1/500 \approx 0.002$ seconds [22, 24]. Thus, two correaltion times of the ground clutter is chosen: a longer correlation time, 0.03 seconds, and a shorter one, 0.001 seconds. As explained earlier, the correlation time of the generated radar signal should be similar to the shorter one between the correlation times due to the platform and clutter dynamics. In Fig. 9, the correlation of the generated signal is computed along the slow time to produce two correlation times of the clutter. It shows that the correlation time becomes the shorter one between the two values of t_c of the gound clutter and the platform.

Next, an AGR simulation is considered for a real radar application. Here, we use the coherent integration technique to combine the 2D time-domain signal [26]. The coherent technique truncates the RD map of the sum signal around the Doppler center. Also, the RD map of the elevation difference signal

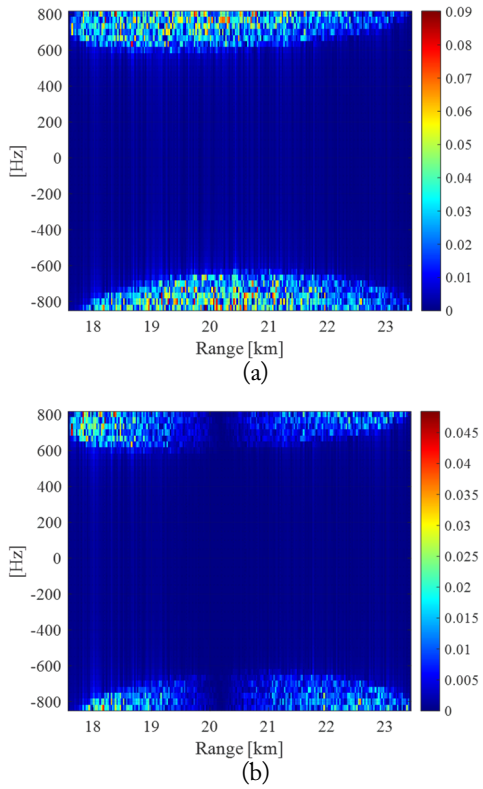

Fig. 8. RD maps of monopulse signals for $t_c = 0.03$ seconds: (a) sum signal (Ψ_Σ) and (b) elevation signal ($\Psi_{\Delta EL}$).

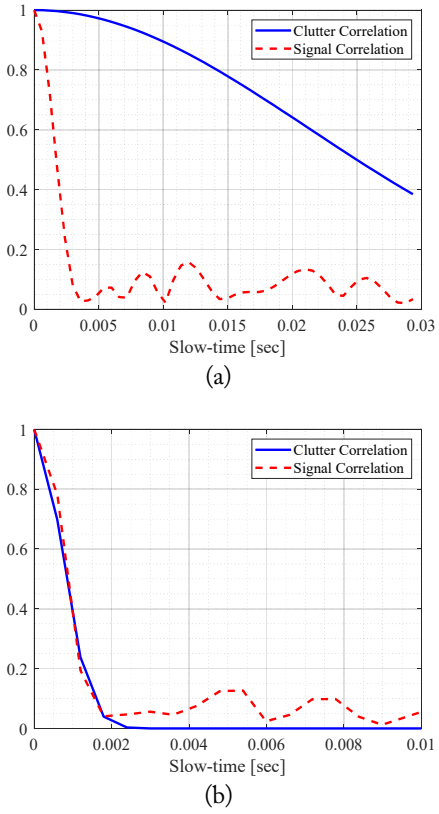

Fig. 9. Correlation of received signals: (a) $t_c = 0.03$ seconds and (b) $t_c = 0.001$ seconds.

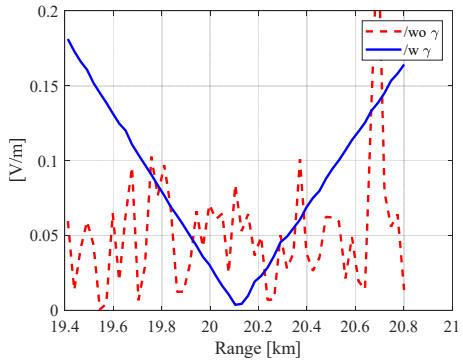

Fig. 10. Monopulse ratio for AGR simulation with and without γ-correction.

is chosen from the same range as that for the sum pattern. Then, the monopulse ratio is calculated and averaged to one ratio [14, 26]. In Fig. 10, the ratio is shown with and without a γ-correction scheme. The γ-correction scheme can retrieve the correct monopulse ratio, which enhances the accuracy of the range estimation. The null point of the monopulse ratio is around the range estimation [26]. Without the γ-correction scheme, the range estimation error is about 2.06% but with the γ-correction scheme, the error is drastically reduced to about 0.07% which is within the known error range ($<\approx 1\%$) of the phase-comparison monopulse AGR scheme [14].

IV. Conclusion

A numerical algorithm was proposed to generate the ground return signal in a time domain for a monopulse radar system, which can accurately consider the radar operation scenario and the Doppler effects due to the movements of the platform and ground clutter. To truncate the return area, the main beam up to the HPBW is projected on the ground surface. Since the projected antenna footprint is estimated using a ray-tracing technique, the accuracy of the footprint can be very high for any radar operation scenario. To simulate the monopulse system, the sum signal is transmitted and then, using the appropriate array weights, the sum and two difference signals are synthesized. This method guarantees the correlation relationship between the sum and difference signals from an identical ground cell. The backscattering coefficient of the ground clutter is assumed to be a Gaussian random process. Thus, the Doppler effect of the ground clutter can be efficiently modeled using a correlated random number generation. For an application example, an AGR simulation is considered. The proposed signal-generation method is applied to a monopulse AGR simulation. It is numerically shown that with the known γ-correction scheme, the signal distortion caused by rolling of the platform can be effectively removed. The range estimation error is within the known error boundary for the phase-comparison monopulse AGR scheme.

This work was supported by a grant-in-aid of Hanwha Systems (No. U-18-015).

References

[1] M. I. Skolnik, *Radar Handbook*. New York, NY: McGraw-Hill, 1970.

[2] J. A. Malas, "F-22 radar development," in *Proceedings of the IEEE 1997 National Aerospace and Electronics Conference (NAECON)*, Dayton, OH, 1997, pp. 831-839.

[3] N. J. Willis and H. D. Griffiths, *Advances in Bistatic Radar*. Raleigh, NC: SciTech Publishing Inc., 2007.

[4] S. M. Sherman and D. K. Barton, *Monopulse Principles and Techniques,* 2nd ed. Boston, MA: Artech House, 2011.

[5] Y. Oh, K. Sarabandi, and F. T. Ulaby, "An empirical model and an inversion technique for radar scattering from bare soil surfaces," *IEEE Transactions on Geoscience and Remote Sensing*, vol. 30, no. 2, pp. 370-381, 1992.

[6] J. C. Curlander and R. N. McDonough. *Synthetic Aperture Radar: Systems and Signal Processing*. New York, NY: John Wiley & Sons, 1991.

[7] X. M. Li, D. Z. Feng, H. W. Liu, M. D. Xing, and D. Luo, "Two-dimensional pulse-to-pulse canceller of ground clutter in airborne radar," *IET Radar, Sonar & Navigation*, vol. 3, no. 2, pp. 133-143, 2009.

[8] G. Zhu, Y. Chen, and H. Yin, "Analysis of typical ground clutter statistical characteristics," in *Proceedings of 2017 International Applied Computational Electromagnetics Society Symposium (ACES)*, Suzhou, China, 2017, pp. 1-2.

[9] A. C. Gurbuz, "Determination of background distribution for ground-penetrating radar data," *IEEE Geoscience and Remote Sensing Letters*, vol. 9, no. 4, pp. 544-548, 2011.

[10] Y. Zhang, H. Hu, and J. Luo, *Distributed Antenna Systems: Open Architecture for Future Wireless Communications*. Boca Raton, FL: Auerbach Publications, 2007.

[11] S. Sorooshyari and D. G. Daut, "Generation of correlated Rayleigh fading envelopes for accurate performance analysis of diversity systems," in *Proceedings of the 14th IEEE Proceedings on Personal, Indoor and Mobile Radio Communications (PIMRC)*, Beijing, China, 2003, pp. 1800-1804.

[12] A. P. Szabo, "Clutter simulation for airborne pulse-Doppler radar," in *Proceedings of the International Conference on Radar (IEEE Cat. No. 03EX695)*, Adelaide, Australia, 2003,

pp. 608-613.
[13] B. R. Mahafza, *Introduction to Radar Analysis*, 2nd ed. Boca Raton, FL: CRC Press, 2017.
[14] P. K. Zwagerman, "Air-to-ground ranging using electronic roll stabilization of monopulse data," in *Proceedings of the 1988 IEEE National Radar Conference*, Ann Arbor, MI, 1988, pp. 151-156.
[15] A. K. Fung, *Microwave Scattering and Emission Models and Their Applications*. Boston, MA: Artech House, 1994.
[16] H. Laur, P. Bally, P. Meadows, J. Sanchez, B. Schaettler, E. Lopinto, and D. Esteban, "Derivation of the backscattering coefficient σ0 in ESA ERS SAR PRI products," European Space Agency, Noordwijk, The Netherlands, *ESA Document ES-TN-RE-PM-HL09*, 2002.
[17] H. Anton and R. C. Busby, *Contemporary Linear Algebra*. Hoboken, NJ: John Wiley & Sons, 2003.
[18] J. J. Hiroshige and T. A. Kennedy, "Error analysis of electronic roll stabilization for electronically scanned antennas," in *Proceedings of the 1991 IEEE National Radar Conference*, Los Angeles, LA, 1991, pp. 71-75.
[19] B. R. Mahafza, *Radar Systems Analysis and Design Using MATLAB,* 3rd ed. Boca Raton, FL: CRC Press, 2013.
[20] Y. Zheng, S. M. Tseng, and K. B. Yu, "Closed-form four-channel monopulse two-target resolution," *IEEE Transactions on Aerospace and Electronic Systems*, vol. 39, no. 3, pp. 1083-1089, 2003.
[21] G. R. Curry, *Radar System Performance Modeling*, 2nd ed. Boston, MA: Artech House, 2004.
[22] D. Tse and P. Viswanath, *Fundamentals of Wireless Communication*. Cambridge, MA: Cambridge University Press, 2005.
[23] C. R. Dietrich and G. N. Newsam, "Fast and exact simulation of stationary Gaussian processes through circulant embedding of the covariance matrix," *SIAM Journal on Scientific Computing*, vol. 18, no. 4, pp. 1088-1107, 1997.
[24] G. V. Morris and L. Harkness, *Airborne Pulsed Doppler Radar*, 2nd ed. Boston, MA: Artech House, 1996.
[25] J. Xu, Y. Peng, Q. Wan, X. Wang, and X. Xia, "Doppler distributed clutter model of airborne radar and its parameters estimation," *Science in China Series F: Information Sciences*, vol. 47, no. 5, pp. 577-586, 2004.
[26] J. H. Nam, H. S. Lee, I. S. Koh, J. H. Song, and C. S. Bae, "Performance assessment of mono-pulse radar air-to-ground ranging algorithm for various clutter environments," *The Journal of Korean Institute of Electromagnetic Engineering and Science*, vol. 31, no. 7, pp. 631-639, 2020.

Jeong-Hun Nam

received a B.S. degree in electronic engineering from Gangneung-Wonju National University, Gangneung, Korea, in 2017. He is currently working toward his M.S. degree at the department of electronic engineering, Inha University, Incheon, Korea. His research interests include radar system modeling and radar clutter signal modeling and analysis.

Hyunsoo Lee

received his M.S. and Ph.D. degrees in electronics engineering from Inha University, Incheon, Korea, in 2014 and 2019, respectively. He is currently working at the agency for defense development, Daejeon, Korea, as a research engineer. His research interests include electromagnetic numerical analysis and diffraction by discontinuous wedge structure.

Jae-Won Rim

received B.S. and M.S. degrees in electronic engineering from Inha University, Incheon, Korea, in 2014 and 2016, respectively. He is currently working toward a Ph.D. at the department of electronic engineering, Inha University, Incheon, Korea. His research interests include modeling and simulation of radar systems, electronic warfare, and numerical methods in electromagnetic fields.

Il-Suek Koh

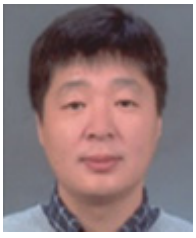

received B.S. and M.S. degrees in electronics engineering from Yonsei University, Seoul, Korea, in 1992 and 1994, respectively, and a Ph.D. degree from the University of Michigan, Ann Arbor, MI, USA, in 2002. In 1994, he joined LG electronics Ltd., Seoul, as a research engineer. Currently, he works at Inha Univerity, Incheon, Korea, as a professor. His research interests include wireless communication channel modeling and numerical and analytical methods for electromagnetic fields.

Jong-Hwa Song

received B.S. and M.S. degrees in electronics engineering from Ajou University, Suwon, Korea, in 2005 and 2007, respectively. He received his Ph.D. from Konkuk University, Korea, in 2016. Currently, he works as a senior engineer on a Avionics Radar Team at Hanwha Systems. His main research interests are radar system design, radar signal processing, and navigation systems for airborne radar.

JOURNAL OF ELECTROMAGNETIC ENGINEERING AND SCIENCE, VOL. 20, NO. 3, 199~206, JUL. 2020

https://doi.org/10.26866/jees.2020.20.3.199
ISSN 2671-7263 (Online) · ISSN 2671-7255 (Print)

Performance Evaluation of a Modified SweepSAR Mode for Quad-Pol Application in SAR Systems

Jung-Hwan Lim[1] · Jae Wook Lee[1,*] · Taek-Kyung Lee[1] · Hyeon-Cheol Lee[2] · Sang-Gyu Lee[2] · Sang-Burm Ryu[2] · Seong-Sik Yoon[3]

Abstract

Efficient earth observation using spaceborne synthetic aperture radar (SAR) requires the analysis of high-resolution wide-swath (HRWS) systems, which have a fine resolution and a short revisit time through wide-area observation, and quadrature-polarimetric (quad-pol) systems, which can obtain a quad-pol image and have many applications. The operational method of SAR generally affects system performance involving the system parameters and antenna patterns, and thus analyzing HRWS quad-pol SAR systems is essential to the system design. In this paper, an extension of the modified SweepSAR technique to a quad-pol observation scenario is performed and a comparison to ScanSAR and conventional SweepSAR is provided for a simulated scenario. On the basis of the system requirements, we selected the optimal parameters and designed a reflector antenna suitable for a wide-swath quad-pol SAR system. As a result of comparing the wide-swath quad-pol SAR operation modes, the modified SweepSAR mode demonstrated advantages in terms of system performance, such as the ambiguity ratio and swath width, and reflector antenna design for a spaceborne SAR system.

Key Words: High-Resolution Wide-Swath (HRWS), Quadrature-Polarimetric (Quad-Pol), Reflector Antenna, Synthetic Aperture Radar (SAR).

I. Introduction

A spaceborne synthetic aperture radar (SAR) is a sensor that is mounted on a satellite and utilizes radio waves to enable high-resolution and all-weather Earth observation. However, conventional spaceborne SAR has some limitations in use because it has a trade-off relationship within the main system parameters. In addition, it obtains information from the Earth's surface by transmitting and receiving only a single polarization.

In Earth observation using spaceborne SAR, an efficient observation requires a short revisit time by observing wide areas [1]. For this purpose, wide-swath SAR operation modes, such as ScanSAR and TOPSAR (terrain observation with progressive scans SAR), were introduced and studied [2, 3]. However, these two modes observe the sub-swaths sequentially and this operational method worsens the resolution in the azimuthal direction of the SAR system. Therefore, obtaining a wide-swath and fine resolution at the same time is difficult for a conventional wide-swath SAR system. To overcome this constraint, many operation modes are currently being studied as high-resolution wide-swath (HRWS) systems. Among these systems, we are interested in HRWS systems using a reflector antenna [4–6]. Generally,

Manuscript received March 13, 2020 ; Revised May 25, 2020 ; Accepted June 8, 2020. (ID No. 20200313-034J)
[1]Department of Electronics and Information Engineering, Korea Aerospace University, Goyang, Korea.
[2]Satellite Payload Development Division, Korea Aerospace Research Institute, Daejeon, Korea.
[3]Imaging Radar Team, Hanwha Systems, Yongin, Korea.
[*]Corresponding Author: Jae Wook Lee (e-mail: jwlee1@kau.ac.kr)

reflector antennas have high gain and moderate bandwidth and can be made light-weight by using composite material or with a mesh-type design. In addition, digital beam forming (DBF) can be performed by on/off operation of the feed elements. One of the operation modes analyzed as a reflector-based HRWS system is SweepSAR [4], which is a SAR operation mode of obtaining a high-resolution image using a broad beam to transmit and a narrow beam to receive based on the SCORE(scan-on-receive) method using DBF. However, this operation mode requires the use of a low pulse repetition frequency (PRF) to obtain an unambiguous wide swath. For this reason, a modified mode of SweepSAR using dual channels, which is called M-SweepSAR, was examined for a single polarization (single-pol) SAR system [6].

Generally, the SAR system employs only a single transmitting/receiving polarization and obtains one type of polarization information. In contrast, in polarimetric SAR, such as dual-polarimetric and quadrature-polarimetric (quad-pol) approaches, various information can be obtained using multiple transmitting and receiving polarizations, and it has been utilized this way in many fields [7, 8]. However, for a SAR system operating in a quad-pol mode, interleaving transmitting pulses of different polarizations impacts the design of the SAR system. Therefore, accurately analyzing this effect, as done in [9, 10], is necessary to design an appropriate quad-pol SAR system.

In the current paper, the reflector antenna and the performance of the proposed quad-pol system operating in M-SweepSAR mode are designed and analyzed, respectively. We also compared wide-swath quad-pol SAR systems in terms of system performance and antenna design.

II. Performance of the Wide-Swath Quad-Pol SAR System

Generally, a SAR system can be characterized by performance indicators, such as the ambiguity-to-signal ratio and resolution. These indicators are strongly related to the system parameters, antenna patterns, and SAR operation modes.

The ambiguity-to-signal ratio, which comprises the range ambiguity-to-signal ratio (RASR) and azimuth ambiguity-to-signal ratio (AASR), is the ratio of undesired signals to the desired SAR signal. it is calculated through the transmitting/receiving antenna pattern, $G_t(\theta)/G_r(\theta)$; backscattering coefficient, σ^0; slant range, ρ; range ambiguous slant range, ρ_{RA}; incidence angle, θ_I; Doppler processing bandwidth, PB; and the angles at which the ambiguity signal occurs in the range and azimuth directions, θ_A and θ_{AZ}, respectively [9, 11]. The resolution, which is the degree of distinguishing the main target from other objects, in the azimuthal direction (ρ_a), is calculated through the beam footprint velocity (V_g), Doppler bandwidth (Δf_{dop}) and wavelength (λ) [12, 13]. The range resolution is related to the bandwidth of the transmitted pulse and is not directly associated with other performance indicators.

$$RASR = \frac{\sum_{n\neq 0}\int_{PB} \frac{\sigma^0(\theta_I(n))G_t(\theta_A(n),\theta_{AZ})G_r(\theta_A(n),\theta_{AZ})}{\rho_{RA}^3(n)\sin(\theta_I(n))} d\theta_{AZ}}{\int_{PB} \frac{\sigma^0(\theta_I(0))G_t(\theta_A(0),\theta_{AZ})G_r(\theta_A(0),\theta_{AZ})}{\rho^3\sin(\theta_I(0))} d\theta_{AZ}} \quad (1)$$

$$AASR = \frac{\sum_{n\neq 0}\int_{PB} G_t(\theta_{AZ}(n))G_r(\theta_{AZ}(n))d\theta_{AZ}(n)}{\int_{PB} G_t(\theta_{AZ}(0))G_r(\theta_{AZ}(0))d\theta_{AZ}(0)} \quad (2)$$

$$\rho_a = \frac{0.886V_g}{\Delta f_{dop}} = \frac{0.443\lambda}{PB} \quad (3)$$

We dealt with the wide-swath and quad-pol operation modes and designed the antenna, which is one of the most important parts of the SAR system, to conduct a proper performance analysis.

1. Wide-Swath SAR System

The swath width of the spaceborne SAR system is affected by the SAR system parameters, such as the PRF, pulse width, altitude of the satellite, and incidence angle. Moreover, the swath width is also related to noise and the resolution performance. As a representative operation mode, ScanSAR, the most widely used wide-swath SAR operation mode, uses multiple beams to sequentially observe sub-swaths, which are designed according to the position of the blind ranges determined by the PRF and pulse width.

However, as the sub-swaths are observed sequentially, the dwell time of each sub-swath is decreased, and the azimuth resolution is degraded in proportion to the number of sub-swaths [2]. In contrast, SweepSAR continuously observes the total swath width by using a broad transmitting antenna beam and narrow receiving antenna beams through a DBF method, whereas ScanSAR uses the same transmitting/receiving pattern for each sub-swath. However, due to the azimuth ambiguity performance and blind range, conventional SweepSAR requires a low PRF and a large reflector antenna.

Alternatively, M-SweepSAR, which is examined in this paper, can overcome this constraint by using two channels, so that this operation mode can reduce the reflector size than SweepSAR. M-SweepSAR uses two rows of linear-array feed antennas, with each of the two channels corresponding to a row. Each channel forms a transmitting/receiving pattern in the same way as the DBF method of SweepSAR. Unlike SweepSAR, however, an area which overlaps the blind range of one channel can be observed by using the other channel. In other

words, each channel operates simultaneously with different PRFs. Two channels continuously observe the total swath with one of the two frequency bands within the total available bandwidth and filtering is performed to reduce interference [6, 14]. The operational concepts of the three wide-swath modes (ScanSAR, SweepSAR, and M-SweepSAR) are shown in Fig. 1.

In this way, the required antenna conditions depend on the SAR operation mode. The selection of the SAR system parameters, such as the PRF, is also affected in meeting the system requirements.

2. Quad-Pol SAR System

In the quad-pol SAR operation, H/V polarization is transmitted and received alternately within the given intervals, and the PRF is doubled that of the single-pol SAR. Therefore, the quad-pol SAR can obtain four types of information: HH, HV, VH, and VV. However, the increase in the PRF causes a decrease of the receiving interval and performance degradation in the RASR.

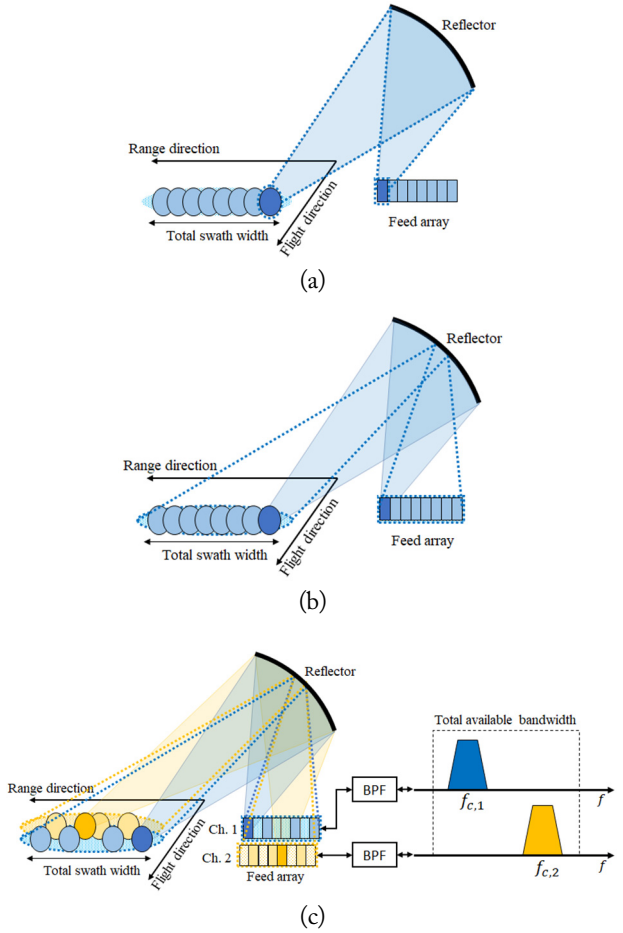

Fig. 1. Operational concepts of the wide-swath SAR systems: (a) ScanSAR, (b) SweepSAR, and (c) M-SweepSAR. Dashed line is transmitting operation; colored region is receiving operation. Adapted from Lim [13].

Moreover, the behavior of backscattering coefficients in different polarizations [15, 16] needs to be considered for the prediction of the quad-pol SAR performance. Due to the interleaving of the transmitting pulses of different polarizations, two types of signals with different transmitting polarization channels but the same receiving polarization channels are considered as range ambiguities. Since cross-polarized backscatter levels are typically lower than the co-pol ones and the first-order ambiguities, in Eq. (1), dominate the range ambiguity levels when considering the antenna radiation pattern, poorer RASR performance is expected for cross-pol in a conventional quad-pol SAR system [9]. For these reasons, when we assume the same effective channel PRF, the quad-pol mode obtains about half the swath width of the single-pol mode.

Therefore, the considerable effects of the use of the quad-pol mode on the SAR system performance need to be analyzed. In addition, performance degradation should be compensated with the selection of appropriate parameters based on the relation between the SAR system parameters and the system performance [17, 18]. The increase in the PRF leads to the degradation of the RASR performance while improving the AASR performance. PB, which is the reliable range in the azimuthal direction, also affects ambiguity performances. It is especially important in the AASR characteristics, which are related to the azimuth resolution, rather than to the RASR.

3. Design of the SAR Reflector Antenna

For satisfying the required performance of a SAR system, a proper antenna should be considered and designed depending on the polarization. In other words, it is necessary to design an antenna that considers quad-pol performance because there is a limit to achieving sufficient quad-pol performance by appropriately selecting the system parameters while using an antenna that had been considered for only single mode in its design [18]. According to a brief comparison between two systems employing the single-pol mode and the quad-pol mode, the ambiguity performance of the single-pol mode is better than that of the quad-pol mode. In terms of resolution, the characteristic of the quad-pol mode is better than that of the single-pol because ScanSAR, which has a trade-off relation between resolution and the number of sub-swaths, covers less swath width due to the increase of the PRF and the RASR performance degradation, especially at the far region, in the quad-pol mode. Therefore, the antenna should be designed to match the ambiguity ratio of the quad-pol mode and the resolution of the single-pol mode.

The relation among the size of the reflector antenna, ambiguity ratio, and resolution of the SAR system is as follows. Increasing the reflector length in the azimuthal direction improves the azimuth ambiguity performance and degrades the resolution regardless of the operation mode. Increasing the reflector width

in the range direction improves the range ambiguity performance in ScanSAR. However, as the beamwidth decreases, the space between the feeds becomes narrower considering the beam deviation factor (BDF) to ensure a continuous total swath width, and the resolution performance is degraded because it leads to an increased number of sub-swaths. The *BDF* of an offset reflector antenna is derived from the beam scan angle, θ_B; feed tilt angle, θ_F; focal length, F; and parent reflector, D_P; as shown in the following [19]:

$$BDF = \frac{\theta_B}{\theta_F} = \frac{1+0.36\left(4\frac{F}{D_p}\right)^{-2}}{1+\left(4\frac{F}{D_p}\right)^{-2}} \tag{4}$$

As SweepSAR and M-SweepSAR continuously observe the full range of the swath width, improving the range ambiguity ratio by increasing the reflector width does not affect the resolution. However, as the reflector width increases, the space between the feeds becomes narrower and the minimum space is limited by the size of the feed antenna. Therefore, RASR and AASR require an increase in the reflector size, but the resolution and the size of the feed antenna must be considered as the upper bound of the reflector width [13, 20].

III. Characteristic Analysis and Comparison of the Quad-Pol M-SweepSAR System

In this research, we selected a spaceborne SAR system with a C-band center frequency operating at an altitude of 505 km with a total swath width of 150 km for a single-pol mode at an incidence angle of 20°–35° [6]. In this case, we assumed that the SAR system performance, which involves an ambiguity ratio in each direction and the resolution should be under the conditions of −20 dB and 10 m, respectively.

The required SAR antenna beamwidth was determined by the swath width and the number of sub-swaths, which help in selecting the optimum reflector antenna depending on the operation mode. This paper suggests a reflector length for the offset reflector antennas of 4 m, 13.5 m, and 6 m for ScanSAR, SweepSAR, and M-SweepSAR, respectively. These antennas had a reflector with F/D_p= 0.409 and a feed array linearly placed in the range direction with one row. Only M-SweepSAR had a feed array with two rows. The radiation patterns of the reflector antenna by several elements at one row of the feed array for the M-SweepSAR system are presented in Fig. 2. These patterns were simulated using the FEKO EM simulation tool. The transmitting pattern in the elevation direction was broad enough to cover the overall swath using additional feed antennas at both ends of each row of the feed array. The receiving patterns were tilted in the elevation direction, so that each feed received echoes from each sub-swath.

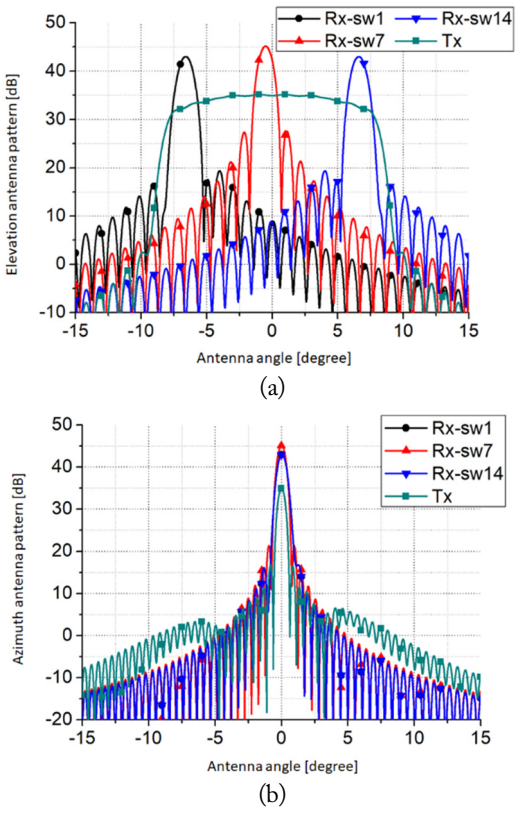

Fig. 2. Antenna radiation patterns used for the quad-pol M-SweepSAR system: (a) elevation patterns and (b) azimuth patterns.

The reflector antenna of each SAR system had a feed antenna according to the number of sub-swaths in the single-pol mode. However, SAR systems use fewer feed antennas in the quad-pol mode to meet the requirements (except for the M-SweepSAR system). In quad-pol M-SweepSAR, the PRF and signal acquisition areas of each channel were determined based on the timing diagram shown in Fig. 3. M-SweepSAR had 14

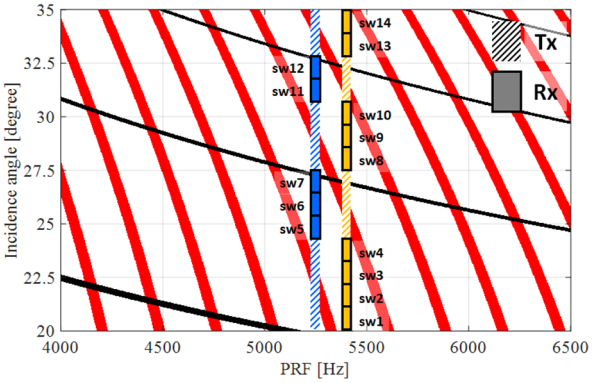

Fig. 3. Timing diagram of the quad-pol M-SweepSAR system. Red lines are blind range; black lines, nadir return; dashed region, channel PRF selection; colored segments, sub-swaths corresponding to each feed element.

sub-swaths in the quad-pol mode with PRFs of 5,250 Hz and 5,400 Hz in each row of the feed array, which maintained an PB of 0.16° and had 14 sub-swaths in a single-pol mode. As shown in Fig. 3, each row of the feed array transmits the signal to sub-swath (sw) 1–14, with one row receiving echoes from sw 5–7 and 11–12, and the other row receiving echoes from sw 1–4, 8–10, and 13–14. ScanSAR had three sub-swaths in the quad-pol mode, with three PRFs of 10.15, 10, and 9 kHz and a PB of 0.44°, and 6 sub-swaths in the single-pol mode. SweepSAR had 13 sub-swaths in the quad-pol mode, with a PRF of 3,400 Hz and PB of 0.26°, and 24 sub-swaths in the single-pol mode. All of the information for the three wide-swath operation modes working in the quad-pol mode is shown in Table 1.

Based on the simulation results of the three quad-pol SAR systems for wide-swath, the SAR performances, including reflector antenna size, ambiguity ratio, resolution, and swath width, were analyzed and compared with the use of the backscattering coefficients assumption, which was suggested by Ulaby and Dobson [16]. In our previous work [18], we had conducted a comparison between our calculation results and data in [9] to verify our analysis procedure on quad-pol SAR systems. Generally, the RASR for the co-pol (HH and VV) was about 10 dB lower than that for the cross-pol (HV and VH). Therefore, we present only the RASR for HV in Fig. 4.

From Table 1 and Fig. 4, the reflector length for SweepSAR was the largest in order to meet the required performance in the single-pol and quad-pol modes while maintaining the required swath width obtained in the single-pol mode because of the characteristics of the SweepSAR operation mode. Conversely, the reflector lengths of M-SweepSAR and ScanSAR were half that of SweepSAR and the smallest, respectively. Quad-pol SweepSAR had the largest reflector antenna but was best in terms of total ambiguity ratio, which means the sum of RASR and AASR. Quad-pol ScanSAR and quad-pol M-SweepSAR had similar levels in ambiguity within the incidence angle range of 20.0°–27.5°. However, it can be conjectured from Fig. 4 that quad-pol M-SweepSAR had better characteristics than quad-pol ScanSAR and satisfied the requirements on the overall incidence angle range.

Table 1. Comparison of the wide-swath quad-pol SAR operation modes

Operation mode	ScanSAR	SweepSAR	M-SweepSAR
Reflector length (m)	4	13.5	6
Number of feeds	6	26 (Tx: 26, Rx: 24)	32 (Tx: 16 × 2, Rx: 14 × 2)
Number of sub-swaths	3	13	14
Swath width (km) (incidence angle, °)	70 (20–27.5)	75 (20–28.1)	150 (20–35)
PRF (Hz)	10,150 10,000 9,000	3,400	5,250 (Ch. 1) 5,400 (Ch. 2),
PB (°)	0.44	0.26	0.16
Azimuth resolution (m)	9.7	5.4	8.9
RASR/AASR (dB)		<–20	

The azimuth resolution depends on the Doppler bandwidth, and in the case of ScanSAR, it is also affected by the number of sub-swaths. As shown by the simulation results, quad-pol ScanSAR had the largest PB with the smallest antenna size, but its resolution was the worst. In addition, quad-pol SweepSAR had the best resolution among the three operation modes, even though it had the largest antenna size because quad-pol M-SweepSAR had a narrower PB for the azimuth ambiguity performance.

In terms of the swath width under the conditions of less than –20 dB RASR and AASR, quad-pol ScanSAR was limited in

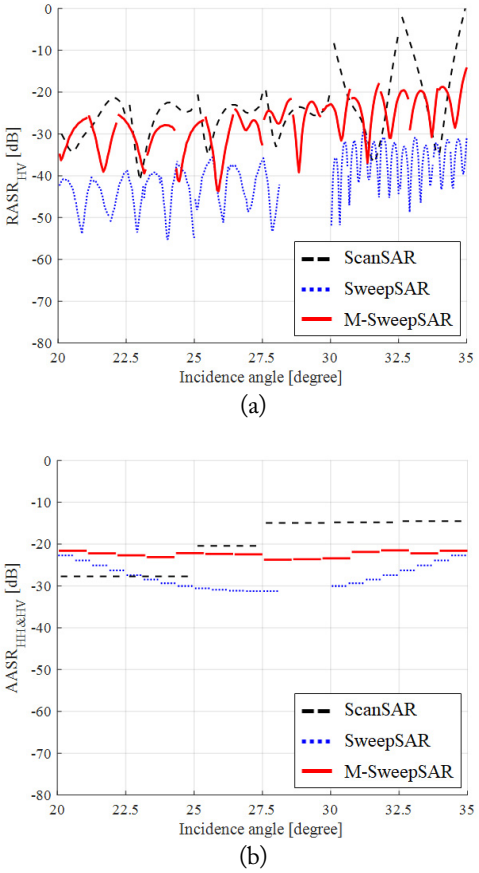

Fig. 4. Comparison of the ambiguity performance of the quad-pol SAR system according to the operation mode: (a) RASR and (b) AASR.

obtaining a wide swath width because of the ambiguity performance degradation over a large incidence angle range. As the PRF increased, and the receiving interval was reduced for the quad-pol mode, quad-pol SweepSAR was also limited in obtaining a continuous total swath width because of the blind range. Therefore, the two modes had half of the total swath width in comparison with the single-pol mode. On the contrary, quad-pol M-SweepSAR could obtain a swath width almost like that of the single-pol mode within the required performance levels. In other words, M-SweepSAR used two PRFs, and this characteristic was advantageous in obtaining a wider swath width than SweepSAR. In addition, M-SweepSAR had a better ambiguity performance than ScanSAR; it was also advantageous in obtaining a wider swath width than ScanSAR.

Most of the differences in the performance indicators discussed in this chapter arose from the differences in antenna patterns, which were determined on the basis of the required performance. Therefore, if the requirements change, the antenna size, which determines the achievable range of the SAR system performance, should be changed. As a result of confirming the performance changes derived from the size of the reflector antenna in each operation mode, increasing the reflector size for the ScanSAR improves the ambiguity performance but worsens the resolution [20]. Conversely, SweepSAR and M-SweepSAR have the advantage of maintaining resolution in comparison with ScanSAR even when the reflector size increases, and M-SweepSAR can reduce the reflector size in comparison with SweepSAR, as mentioned in Chapter II. In other words, for the ScanSAR system to obtain a wider swath width in the quad-pol, a larger reflector must be required to improve the ambiguity ratios, which does not satisfy the resolution requirement. However, we can design a reflector antenna for the M-SweepSAR and achieve a wider swath width in the quad-pol, although it uses a larger reflector than ScanSAR.

IV. Conclusion

In this paper, the performance analysis of the proposed quad-pol M-SweepSAR system was conducted. To determine the validity of our analysis, we designed, analyzed, and compared the ScanSAR, SweepSAR, and M-SweepSAR systems. The result of the analysis and comparison of the three operation modes based on the properly designed systems indicated that M-SweepSAR is expected to be highly recommended as the HRWS spaceborne SAR system because it is advantageous in satisfying the required ambiguity ratio and resolution in both the single-pol and the quad-pol modes with an appropriate reflector antenna size and obtains a wider swath width in the quad-pol mode than the conventional wide-swath operation mode. However, as the feed array has two rows, the system must have dual channels and operate two center frequencies in the available bandwidth. Therefore, filtering for interference suppression should be considered for practical implementation.

This work was performed for the Development of Radar Payload Technologies for Compact Satellite in Korea Aerospace Research Institute, funded by the Ministry of Science and ICT.

References

[1] A. Currie and M. A. Brown, "Wide-swath SAR," *IEE Proceedings F (Radar and Signal Processing)*, vol. 139, no. 2, pp. 122-135, 1992.

[2] D. D'Aria, and F. D. Zan, D. Giudici, A. M. Guarnieri, and F. Rocca, "Burst-mode SARs for wide-swath surveys," *Canadian Journal of Remote Sensing*, vol. 33, no. 1, pp. 27-38, 2007.

[3] F. De Zan and A. M. Guarnieri, "TOPSAR: terrain observation by progressive scans," *IEEE Transactions on Geoscience and Remote Sensing*, vol. 44, no. 9, pp. 2352-2360, 2006.

[4] A. Freeman, G. Krieger, P. Rosen, M. Younis, W. T. Johnson, S. Huber, R. Jordan, and A. Moreira, "SweepSAR: beam-forming on receive using a reflector-phased array feed combination for spaceborne SAR," in *Proceedings of 2009 IEEE Radar Conference*, Pasadena, CA, 2009, pp. 1-9.

[5] M. Villano, G. Krieger, and A. Moreira, "Staggered SAR: high-resolution wide-swath imaging by continuous PRI variation," *IEEE Transactions on Geoscience and Remote Sensing*, vol. 52, no. 7, pp. 4462-4479, 2014.

[6] S. S. Yoon, J. W. Lee, T. K. Lee, S. B. Ryu, H. C. Lee, and S. G. Lee, "A modified SweepSAR mode with dual channels for high resolution and wide swath," *Journal of Electromagnetic Engineering and Science*, vol. 18, no. 3, pp. 199-205, 2018.

[7] V. Turkar, R. Deo, S. Hariharan, and Y. S. Rao, "Comparison of classification accuracy between fully polarimetric and dual-polarization SAR images," in *Proceedings of 2011 IEEE International Geoscience and Remote Sensing Symposium*, Vancouver, Canada, 2011, pp. 440-443.

[8] Y. Yamaguchi, S. Sengoku, H. Yamada, and R. Sato, "Scattering power decomposition results of ALOS2 quad pol data along Amazon River," in *Proceedings of the 12th European Conference on Synthetic Aperture Radar (EUSAR)*, Aachen, Germany, 2018, pp. 1-4.

[9] M. Villano, G. Krieger, and A. Moreira, "New insights into ambiguities in quad-pol SAR," *IEEE Transactions on Geoscience and Remote Sensing*, vol. 55, no. 6, pp. 3287-3308, 2017.

[10] R. K. Raney, A. Freeman, and R. L. Jordan, "Improved range ambiguity performance in quad-pol SAR," *IEEE Transactions on Geoscience and Remote Sensing*, vol. 50, no. 2, pp. 349-356, 2012.
[11] W. A. Imbriale, *Spaceborne Antennas for Planetary Exploration*. New York, NY: John Wiley & Sons, 2006, pp. 305–317.
[12] I. G. Cumming and F. H. Wong, *Digital Processing of Synthetic Aperture Radar Data: Algorithms and Implementation*. Boston, MA: Artech House, 2005, pp. 113–157.
[13] J. H. Lim, "A study on process implementation for performance analysis of C-band quad-pol SAR systems," M.S. thesis, Department of Electronics and Information Engineering, Korea Aerospace University, Goyang, Korea, 2020.
[14] F. Bordoni, G. Krieger, and M. Younis, "Multifrequency subpulse SAR: exploiting chirp bandwidth for an increased coverage," *IEEE Geoscience and Remote Sensing Letters*, vol. 16, no. 1, pp. 40-44, 2018.
[15] T. Jin and Y. Oh, "An improved semi-empirical model for radar backscattering from rough sea surfaces at X-band," *Journal of Electromagnetic Engineering and Science*, vol. 18, no. 2, pp. 136-140, 2018.
[16] F. T. Ulaby and M. C. Dobson, *Handbook of Radar Scattering Statistics for Terrain*. Norwood, MA: Artech House, 1989.
[17] H. M. Braun, "A new SAR sensor designed for microsatellites," in *Proceedings of 2010 IEEE International Geoscience and Remote Sensing Symposium*, Honolulu, HI, 2010, pp. 213-215.
[18] J. H. Lim, S. S. Yoon, J. W. Lee, T. K. Lee, S. B. Ryu, H. C. Lee, and S. G. Lee, "Performance analysis of quad-pol SAR system for wide-swath operation mode," *The Journal of Korean Institute of Electromagnetic Engineering and Science*, vol. 30, no. 2, pp. 141-151, 2019.
[19] W. L. Stutzman and G. A. Thiele, *Antenna Theory and Design*, 3rd ed. New York, NY: John Wiley & Sons, 2013, pp. 407–410.
[20] J. H. Lim, J. W. Lee, T. K. Lee, S. B. Ryu, H. C. Lee, and S. G. Lee, "Optimal Design of the Reflector Antenna to Improve Performance of C-Band Quad-Pol ScanSAR Systems," *Journal of Electromagnetic Engineering and Science*, vol. 20, no. 2, pp. 155-157, 2020.

Jung-Hwan Lim

received his B.S. and M.S. degrees in electronics and information engineering from Korea Aerospace University (KAU), Goyang, Korea, in 2018 and 2020, respectively. He is currently working toward a Ph.D. degree at the Microwave and Millimeterwave Solution Laboratory of KAU. His current research interests include satellite communications/radar antennas, spaceborne SAR systems, and EMI/EMC.

Jae Wook Lee

received his B.S. degree in electronic engineering from Hanyang University, Seoul, Korea, in 1992, and his M.S. and Ph.D. degrees in electrical engineering with a specialization in electromagnetics from the Korea Advanced Institute of Science and Technology, Daejeon, Korea, in 1994 and 1998, respectively. From 1998 to 2004, he was a senior member of the Advanced Radio Technology Department, Radio and Broadcasting Research Laboratory, Electronics and Telecommunications Research Institute, Daejeon. He was with the faculty of the Korea Aerospace University (KAU), Goyang, Korea. He is currently a professor at the School of Electronics and Information Engineering of KAU. His current research interests include high-power amplifier design, computational electromagnetics, electromagnetic interference/electro–mag–netic compatibility analysis on printed circuit boards, satellite antennas, and spaceborne SAR systems.

Taek-Kyung Lee

received his B.S. degree in electronic engineering from Korea University, Seoul, Korea, in 1983, and his M.S. and Ph.D. degrees in electrical engineering from the Korea Advanced Institute of Science and Technology (KAIST), Daejeon, Korea, in 1985 and 1990, respectively. From 1990 to 1991, he was a post-doctoral fellow at the University of Texas at Austin, TX, USA, under a grant from the Korea Science and Engineering Foundation. From 1991 to 1992, he was a research scientist at KAIST. In 1992, he joined the faculty of Korea Aerospace University (KAU), Goyang, Korea. He was an associate visiting research professor at the University of Illinois at Urbana–Champaign, IL, USA, from 2001 to 2002. From 2006 to 2007, he was the chairman of the School of Electronics, Information, and Computer Engineering at KAU, where he was the director of the Aerospace and Aviation Electronics Research Center, from 2011 to 2013. He was the Chairman of the Radar Technical Group, Korean Institute of Electromagnetic Engineering and Science, Seoul, from 2012 to 2013, and he served as the president of this institute in 2014. He is currently a professor at the School of Electronics and Information Engineering, KAU. His current research interests include computational electromagnetics, antennas, microwave passive circuits, satellite antennas and spaceborne SAR systems, and air surveillance systems.

Hyeon-Cheol Lee

received his B.S. and the M.S. degrees in electronic engineering from Kyungpook National University in 1987 and 1989, respectively, and his Ph.D. degree in electrical engineering from Texas A&M University in 2001. From 1989 to 1996, he worked at the Agency for Defense Development (ADD) to modify/operate Target Tracking Control Systems for testing Surface-to-Air Missiles and develop the datalink of surveillance UAVs. In 2002, he worked at the Department of Computer Science in Texas A&M University as a post-doctorate researcher, detecting image contours with an adaptive threshold algorithm. He joined in 2003 at the Korea Aerospace Research Institute (KARI) to develop datalinks and an Auto-tracking System of Vertical Takeoff Landing UAVs. He is recently developing satellite SAR payloads.

Sang-Gyu Lee

received his B.S., M.S., and Ph.D. degrees in electronic engineering from Chungnam National University in 1993, 1995, and 2011, respectively. During 1993–1995, he focused his research in MPEG2 scalability codec and constant bit rate control mechanisms. Since 1995, he has been in charge of the development of very-high-speed satellite image downlink subsystems of KOMPSATs with the Korea Aerospace Research Institute (KARI), Daejeon, Korea. From 2013 to 2015, he was the program manager of KARI's Internal Research and Development (IRND) program, development of phased array antenna for satellite data transmission. Since 2014, he has been in charge of the development of radar payload technologies for the compact satellite. He was the head of payload electronics team of KARI from 2015.

Sang-Burm Ryu

received his B.S. degree in electronic engineering from Daejeon National University of Technology in Daejeon, Korea in 1996 and his M.S. and Ph.D. degrees in the Department of Electronic Engineering from Chungbuk National University, Korea in 2001 and 2010, respectively. Since 2011, he has been working as a senior engineer with the Satellite Payload Development Division, Satellite R&D Head Office, Korea Aerospace Research Institute, Daejeon, Korea. His research interests include spaceborne SAR systems, satellite communications, and spaceborne microwave radiometers.

Seong-Sik Yoon

received his B.S., M.S., and Ph.D. degrees in electronic engineering from Korea Aerospace University, Goyang, Korea, in 2010, 2013, and 2018, respectively. He is currently senior researcher at the Satellite R&D center of Hanwha Systems. His current research interests include satellite communication antennas, radar antenna design and analysis, and spaceborne SAR systems.

JOURNAL OF ELECTROMAGNETIC ENGINEERING AND SCIENCE, VOL. 20, NO. 3, 207~212, JUL. 2020

https://doi.org/10.26866/jees.2020.20.3.207
ISSN 2671-7263 (Online) · ISSN 2671-7255 (Print)

Digitally-Controlled Bondwire Inductor with High Quality Factor and Wide Tuning Range

Yonggoo Lee · Bomson Lee*

Abstract

A tunable bondwire inductor (TBI) with high-quality factor and wide tuning range is presented. The proposed TBI is fabricated on a single chip by combining a single-pole four-throw (SP4T) switch integrated circuit (IC) and four bondwire inductors on a package substrate. The SP4T switch IC is fabricated using 180 nm silicon-on-insulator (SOI) complementary metal-oxide-semiconductor (CMOS) technology. The fabricated TBI chip exhibits a 521% tuning range of inductance from 1.77 to 11 nH at 0.1 GHz and a relatively high-quality factor. To the knowledge of the authors, the results of this work demonstrate the best combined performance of inductance tuning range and quality factor.

Key Words: Bondwire, Digitally-Controlled, High Quality Factor, Tunable Inductor, Wide Tuning Range.

I. Introduction

With increasing demands for high data rate services and the miniaturization of portable radio devices, the challenge of supporting multiple air interface technologies that enable compact multi-mode multi-band devices has become critical [1, 2]. Currently, the market for electrically controllable matching circuits, tunable voltage-controlled oscillators (VCOs), tunable filters, and multi-band power amplifier modules (PAM) is growing rapidly [3–5]. Digitally tunable capacitors using complementary metal-oxide-semiconductors (CMOS) or microelectromechanical system (MEMS) switches have been widely used to meet these technical trends [6–8].

A digitally tunable inductor can be realized by physically changing the metal line length of an inductor with switches. Losses of the switches and metal lines have always been limiting factors in commercializing high-quality (Q) tunable inductors. MEMS-applied tunable inductors have been studied due to their low losses [9, 10]. However, they suffer from several drawbacks, such as complexity, difficulty in monolithic integration with other ICs, and reliability problems [11, 12]. Analog control with MEMS actuators and digital control with MOS switches have been employed to realize the tunable inductors [13–15], but these inductors have drawbacks in Q-factor, tuning range, and action voltage.

We propose a high-Q and wide tunable bondwire inductor (TBI) digitally controlled by RF CMOS switches. The bondwire inductors are adopted because their self-resistance and standard manufacturing process cost are much lower than those of spiral inductors [16, 17]. The RF switches are designed using 180 nm silicon-on-insulator (SOI) CMOS technology to minimize their turn-on resistance. The performance of the proposed TBI is compared with other research results.

Manuscript received March 24, 2020 ; Revised May 13, 2020 ; Accepted June 24, 2020. (ID No. 20200324-040J)
Department of Electronic Engineering, Kyung Hee University, Yongin, Korea.
*Corresponding Author: Bomson Lee (e-mail: bomson@khu.ac.kr)

II. Design of the Tunable Bondwire Inductor

The basic schematic of the proposed TBI and the related equivalent circuits are shown in Fig. 1. The RF switches (S_1, S_2, ···, S_N) and inductors (L_1, L_2, ···, L_N) are connected in series, which are connected in parallel between nodes L_{in} and L_{out}. L_{pkg1} and L_{pkg2} are the inductance of the bondwire used to package the switch integrated circuit (IC), M_{ij} is the mutual inductance between ith and jth inductors, and R_{on} is the resistance for the switch "on" state [18, 19]. The CMOS switch is made of 12 field-effect transistors (FETs) stacked for a high-power handling capability of up to 35 dBm. It is designed to have low R_{on} with an enlarged gate width for a high Q characteristic. The bondwire inductor is based on the single π-model [20]. When the number of inductors connected in parallel increases, the total inductance decreases, and the role of the low-loss L_{pkg1} becomes more important. The overall Q characteristic of the proposed TBI significantly depends on the resistance of the bondwire (L_{pkg1} in Fig. 1) used to package the switch IC. To reduce the resistance, double bonding wire is used. This has been found to significantly enhance the overall Q. Spiral inductors on CMOS substrates usually have low Q-factors because of their high conductor loss, caused by thin metal lines and high dielectric loss. In order to solve these electrical problems, the proposed TBI is designed on a package substrate. The schematic diagram of this proposed TBI is shown in Fig. 2. The positions of the four bondwire inductors achieve a high Q factor by optimizing the configuration of the TBI using an electromagnetic (EM) field simulator that takes into account mutual inductance.

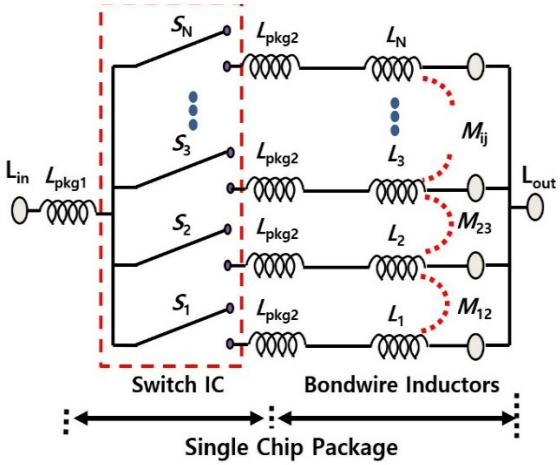

(a)

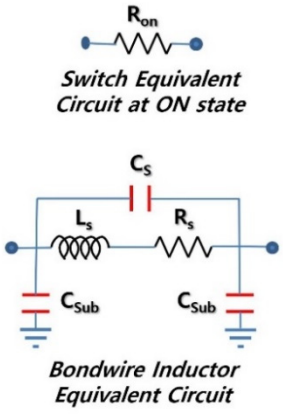

(b)

Fig. 1. (a) Basic schematic of the tunable inductor and (b) the related equivalent circuits.

For the wide tuning range and monotonous increase of inductance, the final inductance values for the single-pole four-throw (SP4T) switch IC and four bondwire inductors are L_{pkg1} = 0.5 nH, L_1 = 4.7 nH, L_2 = 6 nH, L_3 = 10.5 nH, and L_4 = 3.2 nH. These inductance values have been finalized with EM-simulated optimization using a High-Frequency Structure Simulator (HFSS; Ansys Inc., Canonsburg, PA, USA) and starting from a theoretical calculation. The bondwire inductors are implemented on a chip-on-board (COB) substrate with low-loss dielectric material and a thick top metal layer. As such, the loss for the TBI becomes smaller than that for the wafer-level bondwire inductor. Bondwire inductors with low inductance are more sensitive to the internal resistance of the RF switch than those with high inductance. Thus, the switch S_4 for the inductor L_4 is designed to have the lowest internal R_{on} among the four used switches. The SP4T switch IC is controlled through a 3-wire (clock, data, and enable) serial peripheral interface (SPI) and is usually powered using V_{dd} (Fig. 2) of about 3.3 V.

III. Fabrication and Measurement Results

A prototype TBI was fabricated using a COB assembly process to verify the feasibility of the proposed configuration. Photographs of the prototype are shown in Fig. 3. The size of the module consisting of four bondwire inductor arrays and an SP4T RF switch was 2.0 × 2.4 × 0.8 mm^3. The size of the

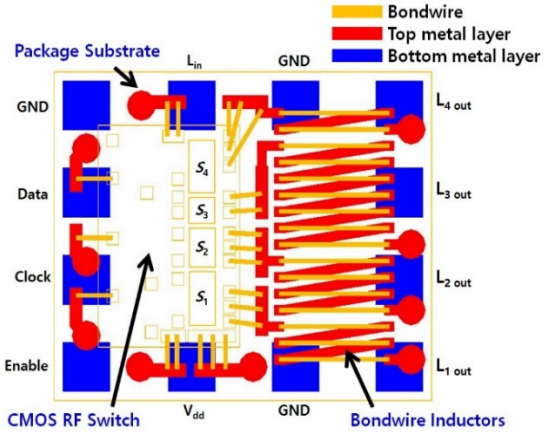

Fig. 2. Diagram of the proposed TBI structure.

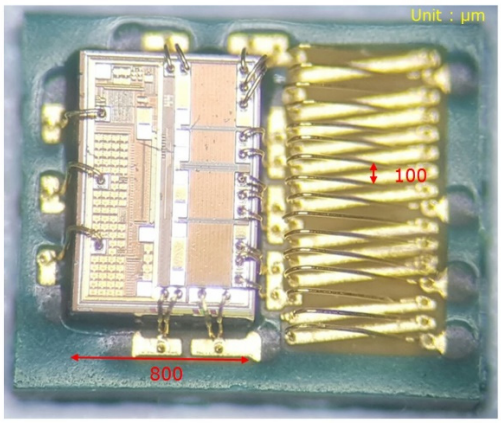

(a)

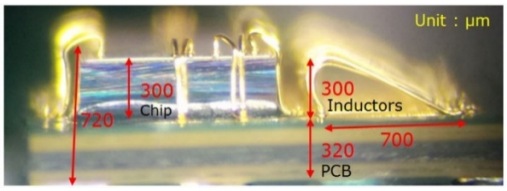

(b)

Fig. 3. Microphotograph of the TBI module: (a) top view and (b) side view.

fabricated SP4T switch with the SPI communication block was 1.3 × 0.8 × 0.3 mm^3. It used thin-film SOI 180 nm CMOS RF switch technology. During fabrication of the TBI, the switch chip was die-bonded on a package substrate (Fig. 2), and the wire bonding for the bondwire inductor and chip packaging was performed using 1 mil (25.4 μm) diameter gold wire. The separation between the bondwires is 100 μm. The height of the bondwires is 300 μm, and the total length of a single bondwire is 1.06 mm. The fabricated chip was measured using a Keysight E5071C network analyzer (Keysight Technologies Inc., Santa Rosa, CA, USA) with a short-open-load-through (SOLT) calibration and de-embedding.

Table 1 lists the performance of the TBI depending on states of 4-bit switch combinations. The fabricated TBI chip exhibits a variable inductance from 1.77 to 11 nH at 0.1 GHz. The maximum Q of 29.5 occurs at 2.1 GHz in state 15, where the self-resonant frequency (SRF) is 4.42 GHz.

The measured inductances and Q-factors are shown in Fig. 4 as a function of frequency from 0 to 3.5 GHz. The measured inductance of the TBI shows a monotonically increasing characteristic. In Fig. 4(b), the states with two or more bondwire inductors are shown to have higher Q characteristics than those with one bondwire inductor. These high Q characteristics are obtained by minimizing the turn-on resistance of the RF switch with an enlarged gate width, minimizing the self-resistance of package bondwire with a double bondwire connection, and optimizing the configuration of the TBI using the 3D EM simulation tool.

The measured inductances and Q-factors for all states at 1.5 GHz and 2 GHz are shown in Fig. 5. A higher Q occurs with more parallel-connected inductors, as in states 11 and 15. When the number of parallel inductors increases, the TBI has an additional magnetic flux due to the mutual coupling. The parallel inductance by the bondwire inductors becomes small so that the effect of the inductance of L_{pkg1} used as a package is relatively high. Therefore, a higher Q is achieved with more parallel-connected TBIs.

In Table 2, the performance of the proposed TBIs are com-

Table 1. Performance depending on switch states

Switch state	Combination of inductors	L (nH) @0.1 GHz	Peak Q (Q_{peak})	Freq. @Q_{peak}	SRF (GHz)
1	L_1	5.20	10.8	1.30	2.47
2	L_2	6.50	8.6	1.07	2.24
3	L_1 // L_2	3.14	17.1	1.24	3.41
4	L_3	11.00	6.2	0.72	1.74
5	L_1 // L_3	3.75	13.3	1.30	2.94
6	L_2 // L_3	4.32	11.0	1.23	2.54
7	L_1 // L_2 // L_3	2.61	14.4	1.44	3.07
8	L_4	3.70	15.3	1.24	2.95
9	L_1 // L_4	2.40	21.3	1.85	4.42
10	L_2 // L_4	2.59	19.1	1.72	2.94
11	L_1 // L_2 // L_4	1.95	28.0	2.01	4.40
12	L_3 // L_4	2.95	12.4	1.44	2.85
13	L_1 // L_3 // L_4	2.11	25.7	1.85	4.43
14	L_2 // L_3 // L_4	2.24	23.1	1.90	3.41
15	L_1 // L_2 // L_3 // L_4	1.77	29.5	2.10	4.42

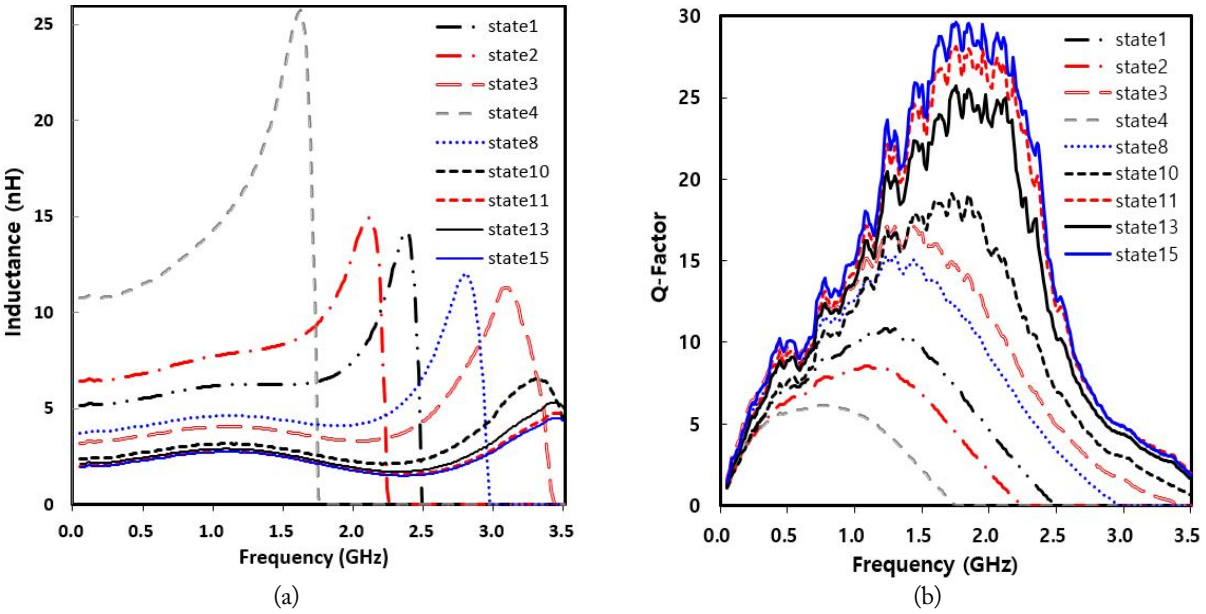

Fig. 4. Measured inductances (a) and Q-factors (b) for different switching states.

Table 2. Comparison of tunable inductors

Ref., year	Control		Size (mm^2)	Primary inductance (nH)	Tuning range (%)	Q-factor / freq. (GHz)
	Type	Method				
[13], 2003	Digital CMOS	1.6 V	0.2 × 0.22	8	< 200	7 / 2
[14], 2005	Analog MEMS	7 V	2.2 × 4	8.5	< 30	35 / 2
[21], 2008	Digital MEMS	40 V	-	1.1	47	45 / 6
[20], 2009	Analog MEMS	0–11 mW	0.25 × 0.25	0.72	< 100	26 / 15
[23], 2009	Digital MEMS	60 V	0.4 × 0.69	0.75	< 80	8.5 / 4
[15], 2010	Analog MEMS	9 V	-	0.36	< 78	17.6 / 3.9
[22], 2012	Analog MEMS	20 V	1.6 × 1.6	3	< 233	12.9 / 5.3
[24], 2012	Analog MEMS	~1.2 A	8 × 8	186	< 16	23 / 0.06
[25], 2013	Analog MEMS	Liquid injected	-	1.3	< 60	18 / 12
[26], 2013	Analog MEMS	RF 0.7 W	7 × 7	37.5	< 12	17 / 1.2
[27], 2018	Digital Memristor	−0.4 to 3 V	-	4.6	< 296	18 / 5
Proposed	Digital CMOS	3.3 V	2 × 2.4	1.77	< 521	29.5 / 2

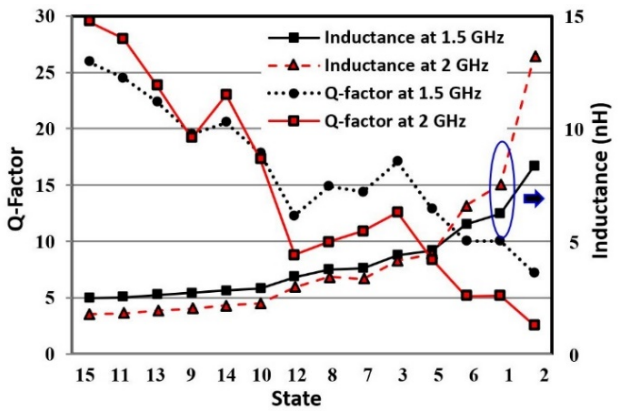

Fig. 5. Measured inductances and Q factors for all states at 1.5 GHz and 2 GHz.

pared with others [13–15, 20–27] in terms of primary inductance, size, tuning range, Q-factor, and action voltage. Due to the narrow tuning range characteristics below 233 and the need for voltage above 7 V or special operating signals, the tunable inductors [14, 15, 20–26] using MEMS actuators have limitations for general product applications. In Park et al. [13], a multi-layer stacked inductor switched by MOSFETs is reported. The main drawback of this device is its low Q, caused by parasitic losses of the transistor. In Wainstein and Kvatinsky [27], two topologies, a memristive-via switched tunable inductor and a multi-layer stacked inductor tuned by RF memristive switches, are proposed and simulated using Advanced Design System (ADS). By improving the parasitic losses of the switch, Wain-

stein and Kvatinsky [27] obtain a higher Q than Park et al. [13]. TBI has the advantages of complete SPI control, wide tuning range by 4-bit control, and high Q using bonding wire inductors. Overall, the proposed TBI is superior to others.

IV. Conclusion

The proposed tunable bondwire inductor has been shown to exhibit a wide (521%) tuning range, from 1.77 to 11 nH at 0.1 GHz. It has also shown high Q-factors, with a maximum of 29.5 when four inductors are all connected in parallel. These competitive results have been obtained using thin-film SOI 180 nm CMOS RF switch technology and wire bond technology.

The proposed tunable inductor is a promising key component for such uses as electrically controllable RF circuits, filters with wide tuning range, and matching circuits for various applications.

This research was supported by the Ministry of Science and ICT, Korea, under the Information Technology Research Center support program (No. IITP-2020-2016-0-00291) supervised by the Institute for Information & Communications Technology Planning & Evaluation (IITP).

References

[1] N. Cheng and J. P. Young, "Challenges and requirements of multimode multiband power amplifiers for mobile applications," in *Proceedings of 2011 IEEE Compound Semiconductor Integrated Circuit Symposium (CSICS)*, Waikoloa, HI, 2011, pp. 1-4.

[2] N. A. Kamsani, V. Thangasamy, M. F. Bukhori, and S. Shafie, "A multiband 130nm CMOS second order band pass filter for LTE bands," in *Proceedings of 2015 IEEE International Circuits and Systems Symposium (ICSyS)*, Langkawi, Malaysia, 2015, pp. 100-105.

[3] P. Starke, D. Fritsche, C. Carta, and F. Ellinger, "A passive tunable matching filter for multiband RF applications demonstrated at 7 to 14 GHz," *IEEE Microwave and Wireless Components Letters*, vol. 27, no. 8, pp. 703-705, 2017.

[4] E. Arabi, X. Jiao, K. Morris, and M. Beach, "Analysis of the coverage of tunable matching networks with three tunable elements," in *Proceedings of 2017 IEEE MTT-S International Microwave Symposium (IMS)*, Honolulu, HI, 2017, pp. 904-906.

[5] S. Yokano, T. Chiba, S. Nagai, K. Hirabayashi, and N. Adachi, "A wide range tunable bandpass filter using imaginary resonance phenomena," in *Proceedings of 2018 Asia-Pacific Microwave Conference (APMC)*, Kyoto, Japan, 2018, pp. 606-608.

[6] D. H. Baek, Y. Eun, D. S. Kwon, M. O. Kim, T. Chung, and J. Kim, "Widely tunable variable capacitor with switching and latching mechanisms," *IEEE Electron Device Letters*, vol. 36, no. 2, pp. 186-188, 2015.

[7] T. W. Lin, K. K. W. Low, R. Gaddi, and G. M. Rebeiz, "High-linearity 5.3-7.0 GHz 3-pole tunable bandpass filter using commercial RF MEMS capacitors," in *Proceedings of 2018 48th European Microwave Conference (EuMC)*, Madrid, Spain, 2018, pp. 555-558.

[8] Y. K. Jung and B. Lee, "Design of tunable optimal load circuit for maximum wireless power transfer efficiency," *Microwave and Optical Technology Letters*, vol. 56, no. 11, pp. 2619-2622, 2014.

[9] M. M. Teymoori and J. M. Ahangarkolaei, "MEMS tunable inductors: a survey," *Australian Journal of Basic and Applied Sciences*, vol. 5, no. 12, pp. 1868-1878, 2011.

[10] N. Habbachi, H. Boussetta, M. A. Kallala, P. Pons, A. Boukabache, and K. Besbes, "Leakage current effect on fixed and tunable solenoid RF MEMS inductors," in *Proceedings of 2017 International Conference on Engineering & MIS (ICEMIS)*, Monastir, Tunisia, 2017, pp. 1-6.

[11] V. Turgul, T. Nesimoglu, and B. S. Yarman, "A study on RF/microwave tunable inductor topologies," in *Proceedings of 2013 13th Mediterranean Microwave Symposium (MMS)*, Saida, Lebanon, 2013, pp. 1-4.

[12] R. R. Manikandan and V. N. R. Vanukuru, "A high performance switchable multiband inductor structure for LC-VCOs," in *Proceedings of 2017 30th International Conference on VLSI Design and 2017 16th International Conference on Embedded Systems (VLSID)*, Hyderabad, India, 2017, pp. 253-258.

[13] P. Park, C. S. Kim, M. Y. Park, S. D. Kim, and H. K. Yu, "Variable inductance multilayer inductor with MOSFET switch control," *IEEE Electron Device Letters*, vol. 25, no. 3, pp. 144-146, 2004.

[14] N. Sarkar, D. Yan, E. Horne, H. Lu, M. Ellis, J. B. Lee, R. Mansour, A. Nallani, and G. Skidmore, "Microassembled tunable MEMS inductor," in *Proceedings of 18th IEEE International Conference on Micro Electro Mechanical Systems (MEMS)*, Miami Beach, FL, 2005, pp. 183-186.

[15] D. M. Fang, X. H. Li, Q. Yuan, and H. X. Zhang, "Design, simulation, and characterization of variable inductor with electrostatic actuation fabricated by using surface micromachining technology," *IEEE Transactions on Electron Devices*, vol. 57, no. 10, pp. 2751-2755, 2010.

[16] Y. G. Lee, S. K. Yun, and H. Y. Lee, "Novel high-Q bondwire inductor for MMIC," in *Proceedings of International Electron Devices Meeting 1998 Technical Digest (Cat. No. 98CH36217)*, San Francisco, CA, 1998, pp. 548-

551.

[17] K. C. Lin, H. K. Chiou, P. C. Wu, W. H. Chen, C. L. Ko, and Y. Z. Juang, "2.4-GHz complementary metal oxide semiconductor power amplifier using high-quality factor wafer-level bondwire spiral inductor," *IEEE Transactions on Components, Packaging and Manufacturing Technology*, vol. 3, no. 8, pp. 1286-1292, 2013.

[18] Z. Cheng, G. Yan, W. Ni, D. Zhu, H. Ni, J. Li, S. Chen, and G. Liu, "15158A SP6T RF switch based on IBM SOI CMOS technology," *Journal of Semiconductors*, vol. 37, no. 5, article no. 055007, 2016.

[19] A. S. Cardoso, P. S. Chakraborty, A. P. Omprakash, N. Karaulac, P. Saha, and J. D. Cressler, "On the cryogenic performance of ultra-low-loss, wideband SPDT RF switches designed in a 180 nm SOI-CMOS technology," in *Proceedings of 2014 SOI-3D-Subthreshold Microelectronics Technology Unified Conference (S3S)*, Millbrae, CA, 2014.

[20] J. I. Kim and D. Peroulis, "Tunable MEMS spiral inductors with optimized RF performance and integrated large-displacement electrothermal actuators," *IEEE Transactions on Microwave Theory and Techniques*, vol. 57, no. 9, pp. 2276-2283, 2009.

[21] M. Rais-Zadeh, P. A. Kohl, and F. Ayazi, "MEMS switched tunable inductors," *Journal of Microelectromechanical Systems*, vol. 17, no. 1, pp. 78-84, 2008.

[22] S. S. Bedair, J. S. Pulskamp, C. D. Meyer, M. Mirabelli, R. G. Polcawich, and B. Morgan, "High-performance micromachined inductors tunable by lead zirconate titanate actuators," *IEEE Electron Device Letters*, vol. 33, no. 10, pp. 1483-1485, 2012.

[23] D. H. Choi, H. S. Lee, and J. B. Yoon, "Linearly variable inductor with RF MEMS switches to enlarge a continuous tuning range," in *Proceedings of 2009 International Solid-State Sensors, Actuators and Microsystems Conference (TRANSDUCERS)*, Denver, CO, 2009, pp. 573-576.

[24] B. Assadsangabi, M. M. Ali, and K. Takahata, "Ferrofluid-based variable inductor," in *Proceedings of 2012 IEEE 25th International Conference on Micro Electro Mechanical Systems (MEMS)*, Paris, France, 2012, pp. 1121-1124.

[25] F. Banitorfian, F. Eshghabadi, A. Abd Manaf, P. Pons, N. M. Noh, M. T. Mustaffa, and O. Sidek, "A novel tunable water-based RF MEMS solenoid inductor," in *Proceedings of 2013 IEEE Regional Symposium on Micro and Nanoelectronics (RSM)*, Langkawi, Malaysia, 2013, pp. 58-61.

[26] M. S. M. Ali, B. Bycraft, A. Bsoul, and K. Takahata, "Radio-controlled microactuator based on shape-memory-alloy spiral-coil inductor," *Journal of Microelectromechanical Systems*, vol. 22, no. 2, pp. 331-338, 2012.

[27] N. Wainstein and S. Kvatinsky, "TIME: tunable inductors using memristors," *IEEE Transactions on Circuits and Systems I: Regular Papers*, vol. 65, no. 5, pp. 1505-1515, 2018.

Yonggoo Lee

received a B.S. degree in Electronics Engineering from Ajou University, Suwon, Korea, in 1994. From 1994 to 1996, he was with Hyundai Mobis Technical Center, Yongin, Korea. He received an M.S. degree in Electronics Engineering from Ajou University, Suwon, Korea, in 1998. From 1998 to 2001, he was with CS Corporation, Seongnam, Korea. From 2001 to 2014, he was with GigaLane Company, Gyeonggi-do, Korea, as its Chief Technology Officer. He is currently pursuing a Ph.D. degree in Electronics Engineering from Kyung Hee University, Yongin, Korea. He founded WithWave Company, Suwon, Korea, in 2014, and manages it as Chief Executive Officer. His current research interests include RF tunable devices, microwave communication system, RF MEMS devices, millimeter-wave interconnections, and electromagnetic measurement standards.

Bomson Lee

received a B.S. degree in Electrical Engineering from Seoul National University, Seoul, Korea, in 1982. From 1982 to 1988, he was with the Hyundai Engineering Company Ltd., Seoul, Korea. He received M.S. and Ph.D. degrees in Electrical Engineering from the University of Nebraska, Lincoln, NE, USA, in 1991 and 1995, respectively. In 1995, he joined the faculty at Kyung Hee University, where he is currently a professor in the Department of Electronics and Radio Engineering. From 2007 to 2008, he was the chair of the technical group for microwave and radio wave propagation in the Korea Institute of Electromagnetic Engineering & Science (KIEES). In 2010, he was an Editor-in-Chief of the Journal of the Korean Institute of Electromagnetic Engineering and Science. In 2018, he served as the president of KIEES. His research interests include microwave antennas, RFID tags, microwave passive devices, wireless power transfer, and metamaterials.

JOURNAL OF ELECTROMAGNETIC ENGINEERING AND SCIENCE, VOL. 20, NO. 3, 213~220, JUL. 2020

https://doi.org/10.26866/jees.2020.20.3.213
ISSN 2671-7263 (Online) · ISSN 2671-7255 (Print)

Design and Investigation of a Miniaturized Single-Layer ACS-Fed Dual Band Antenna for LTE and 5G Applications

Shine Let Gunamony* · Josemin Bala Gnanadhas · Diana Evangeline Lawrence

Abstract

Presently, a single compact antenna is expected to operate in multiple frequency bands, so that it may be used for multiple applications. In this regard, a compact asymmetric coplanar strip (ACS) fed monopole antenna was designed to operate in LTE band-40 and 5G mid band frequencies. To achieve the desired dual band frequency, meander line radiating structure was used. The uniplanar design with the ACS feed considerably reduced the antenna size to 19.25 × 10.5 × 1.6 mm^3. This miniaturized dual band antenna can be easily integrated into circuit boards. The measured and simulated results provided a reflection coefficient (S_{11}) <−15 dB, which made the antenna suitable for LTE band-40 and 5G mid-band communication applications.

Key Words: ACS Feed, Dual-Band, LTE, Meander Antenna, 5G.

I. INTRODUCTION

Today, a single communicating device is expected to be capable of operating in multiple frequency bands based on applications such as WLAN, GPS, Bluetooth, WiMax, cellular mobile communication, and so on. To achieve compactness in the design of all components and circuits, considerable research has been conducted and is ongoing [1]. Furthermore, from an antenna design perspective, a single antenna with compact size has to operate in multiple frequency bands, which remains a challenging task. In the literature, to achieve a compact multiband functionality antenna, different radiating and ground plane structures and feeding techniques have been proposed. The various feeding techniques considered in antenna designs include microstrip feed, coplanar waveguide (CPW) feed, coaxial feed or asymmetric coplanar strip (ACS) feed [2]. To integrate the antenna with the radio frequency circuitry, uniplanar antenna design is well suitable (i.e., having the radiating patch and ground plane in a single layer) [1]. To feed the uniplanar design antenna either the CPW feed or ACS-feeding technique is used [3–8].

Different structures, such as L-shape, inverted L-shape, F-shape, mouse-shape, meander line, circular slot, U-shape slot, etcetera, are considered in the radiating patch and ground plane to achieve multiband functionalities in an antenna [4–6]. The ACS-fed meander line radiating structure is used to obtain antenna operation in WLAN and WiMax applications [4]. To operate in triple operating frequency bands, a mouse-shaped

Manuscript received February 19, 2020 ; Revised April 16, 2020 ; Accepted July 7, 2020. (ID No. 20200219-020J)
Department of Electrical and Computer Engineering, Karunya Institute of Technology and Sciences, Coimbatore, India.
*Corresponding Author: Shine Let Gunamony (e-mail: shinelet@gmail.com)

radiating strip has been proposed in [7]. Anil Kumar et al. [8] reported an F-shaped radiating patch that allows the antenna to operate in three bands such as digital cellular system (DCS), Wi-Fi and WiMax applications. Metamaterial-inspired conformed antenna design has been implemented to obtain dual band operation at Wi-Fi and WiMax frequencies [9]. Four pairs of circular and square slots are cut from the radiating patch to obtain dual band operation in WLAN bands [10]. An L-shaped microstrip line was used to obtain dual band operation in [11].A slit-loaded semi-circular ring radiating patch with asymmetric microstrip feeding allows the antenna to operate in triple bands such as WLAN, International Telecommunication Union (ITU), and X-band application [12]. An F-shaped ACS-fed monopole antenna operating in GPS, Wi-Fi and WiMax frequency bands was proposed in [13]. In the literature, a modified split ring resonator (SRR) structure is designed on an optically transparent substrate to obtain the WLAN dual band operation [14]. A D-shape SRR configuration is used in the antenna design to work in the WiMax and C-band applications [15]. Further compact and single-layer multi-band antennae operating at different mobile communication bands are needed based on an analysis of the available literature.

In this paper, a meander line structure ACS-fed dual band monopole antenna is proposed for operation within mobile communication Long Term Evolution (LTE) band-40 (2.3–2.4 GHz) and 5G mid-band (3.4–3.8 GHz). The following sections provide a detailed description of the antenna design evolution process, the parametric study that was conducted, the fabricated antenna, and a discussion of the results.

II. Antenna Design Evolution Process

The proposed meander line antenna structure was designed in a single side copper-platted FR4 substrate with 1.6 mm thickness. The proposed antenna's basic structure was derived from the literature [4]. The authors designed an antenna to operate in WLAN dual band, that is, 2.4 to 5 GHz. In the proposed design, different sizes of radiating strips are inserted to operate in LTE band-40 and 5G mid frequency bands used in mobile communication applications. In order to design an electrically small antenna, the electrical length of the antenna "βa" should be less than one [16]. Here "β" represents the free space wave number, and "a" is the radius of the imaginary sphere that encloses the antenna. For the designed antenna, $\beta a = 0.841 < 1$ at the maximum operating frequency of 3.6 GHz. The steps of the proposed antenna development are depicted in Fig. 1.

The following are the steps considered for the proposed antenna design:

Step 1: An inverted rectangular C-shape strip is supplied with ACS feeding. The resulting operating frequency is between 3.12 and 3.28 GHz.

Step 2: By making rectangular bends in the inverted C-shape, the total length of the radiating element is increased and a new inverted L-shape radiating strip is attached to the feed line. The operating frequency is changed to 2.65 to 2.71 GHz as the length increases.

Step 3: Two rectangular radiating strips of 0.5 mm length are added at the end of the rectangular bend. This helps to achieve the 2.3–2.34 GHz operating frequency, which is within the LTE band-40 frequency.

Step 4: To obtain dual band operating frequency, three rectangular radiating strips are included in the middle of the rectangular bend. It allows the antenna to operate in dual band frequencies: 2.36–2.4 GHz and 3.4–3.46 GHz.

Step 5: Two radiating strips are added in the inverted L-shape to adjust the operating frequency within the 5G mid frequency band. The obtained frequency of operation in the final design is 2.36–2.4 GHz and 3.44–3.5 GHz.

The reflection coefficients obtained at various steps are illustrated in Fig. 2.

The proposed dual band antenna's geometry representation is

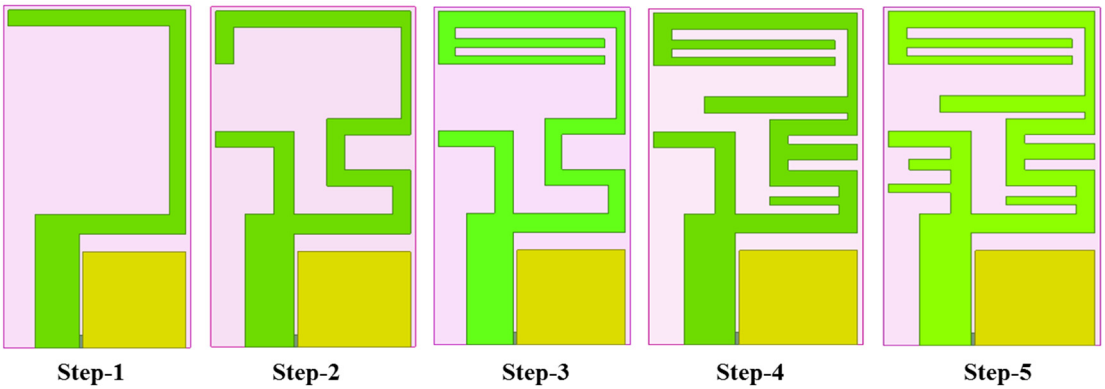

Fig. 1. Proposed antenna design evolution process.

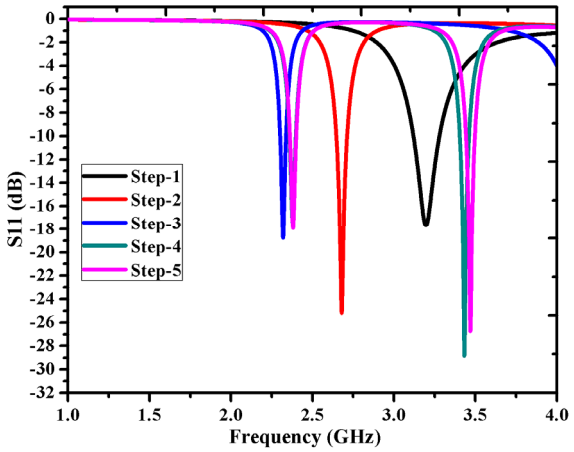

Fig. 2. Reflection coefficient obtained in the antenna design evolution process.

depicted in Fig. 3. The total dimension of the antenna is $L \times W$ mm^2. The ground metallic surface occupies an area of $L_g \times W_g$ mm^2. The gap introduced between the ground and radiating metallic surface near the feed point is 0.2 mm. The dimension of the rectangular strips added in the radiating surface is demonstrated in Table 1.

Using the antenna design concept, the height of the antenna (h) is directly proportional to its wavelength [17]. Here, a printed meander line (rectangular strip) design is considered. To radiate the antenna at 2.35 GHz, the monopole antenna should have a length of 31.91 mm. To have the radiation at 3.5 GHz, 21.43 mm is the required antenna length. Four E-shape meander line structures are used in the design and are shown in Fig. 4.

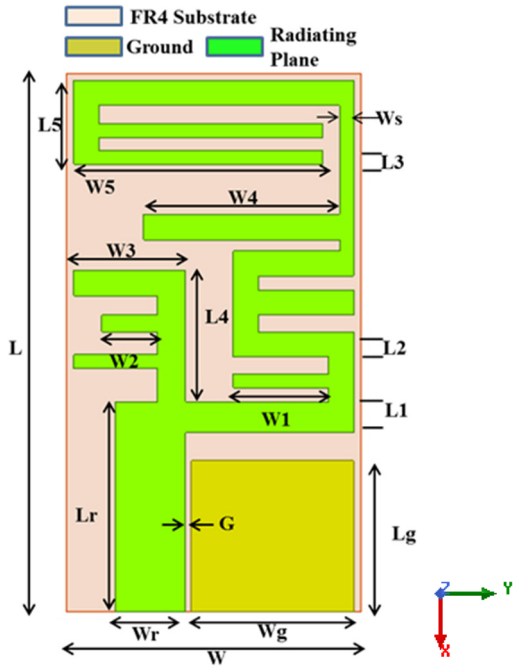

Fig. 3. Geometry of the proposed design.

Table 1. Parameters of the designed compact meander antenna

Parameter	Value (mm)	Parameter	Value (mm)
L	19.25	L_1	1.1
W	10.5	L_2	0.9
L_r	7.5	L_3	0.5
W_r	2.5	L_4	4.7
L_g	5.4	L_5	3
W_g	5.8	W_3	4
G	0.2	W_4	7
W_1	3.4	W_5	8.9
W_2	2	W_s	0.5

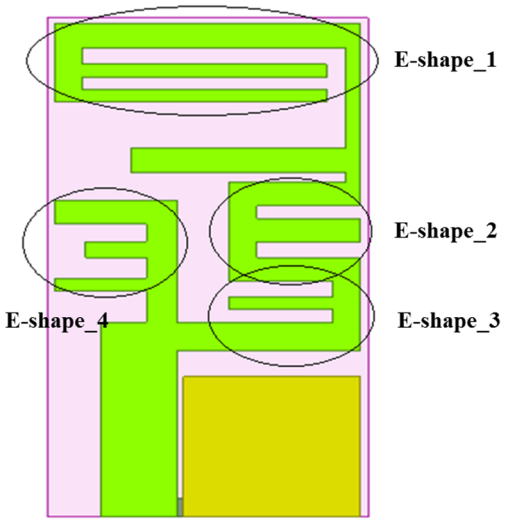

Fig. 4. E-shape structures in the proposed design.

In the design, E-shape_1 from the feed line plays a major role in tuning the antenna at a resonant frequency of 2.35 GHz. Furthermore, E-shape_3 helps the antenna tune to the resonant frequency at 3.5 GHz. Fig. 5 depicts the equivalent circuit of an E-shape. The strip line is represented as an inductor, and the gap between two strip lines are modelled as a capacitor. As the width or length of the strip line varies, the resonant frequency varies. The resonant frequency is given by:

$$f = \frac{1}{2\pi\sqrt{L_{eq}C_{eq}}}$$

where C_{eq} and L_{eq} represent the capacitor equivalent value and inductor equivalent value, respectively. The variation in resonant frequency occurs as the length and width of the strips differ and is discussed in the next section.

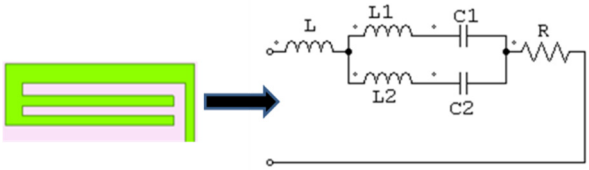

Fig. 5. E-shape equivalent circuit.

III. PARAMETRIC STUDY

The length and width of the rectangular strips were varied using parametric analysis and an optimum value was obtained. Fig. 6 displays the variation of the reflection coefficient (S_{11}) when the ground length (L_g) changes. As the ground length increases, the reflection coefficient of the LTE band-40 decreases, and when L_g decreases, the operating frequency moves away from the LTE band. Similarly, the operating frequency shifts away from the 5G mid-band as the L_g value increases or decreases from the optimal value. Based on the parametric study on ground length, the optimal value considered was $L_g = 5.4$ mm.

The parametric study was conducted on the rectangular strips inserted in the proposed antenna design. The strip length and width were determined using the parametric analysis. Fig. 7 illustrates the variation in reflection coefficient and the operating frequency as the length (L_1) and width (W_s) of the rectangular strip vary. As the rectangular strip width (W_s) decreases from the optimal value, the highest operating frequency shifts away from the 5G mid-band. Increase in W_s, shifts the 5G frequency band below the operating frequency. Similarly, the variation in L_1 alters the desired frequency of operation and the reflection coefficient, as depicted in Fig. 7(b). The optimal value considered for Ws and L_1 are 0.5 mm and 1.1 mm, respectively.

The surface current distribution at 2.35 and 3.5 GHz are shown in Fig. 8. At 2.35 GHz, the current distribution is near the end of the horizontal and vertical radiating rectangular strips. The current path length is equal to 32.4 mm. This path length is very close to $\lambda_g/4$ (monopole antenna length), contributing resonance at 2.35 GHz. At 3.5 GHz, the current distribution is close to the feedline, and the current path length is approximately 22 mm.

Radiation pattern provides information about the distribution of the radiating energy from the antenna to other devices. Fig. 9 depicts the simulated radiation pattern at frequencies of 2.35 and 3.5 GHz when angle Phi (ϕ) is zero degree. At $\phi = 0^{o}$, the

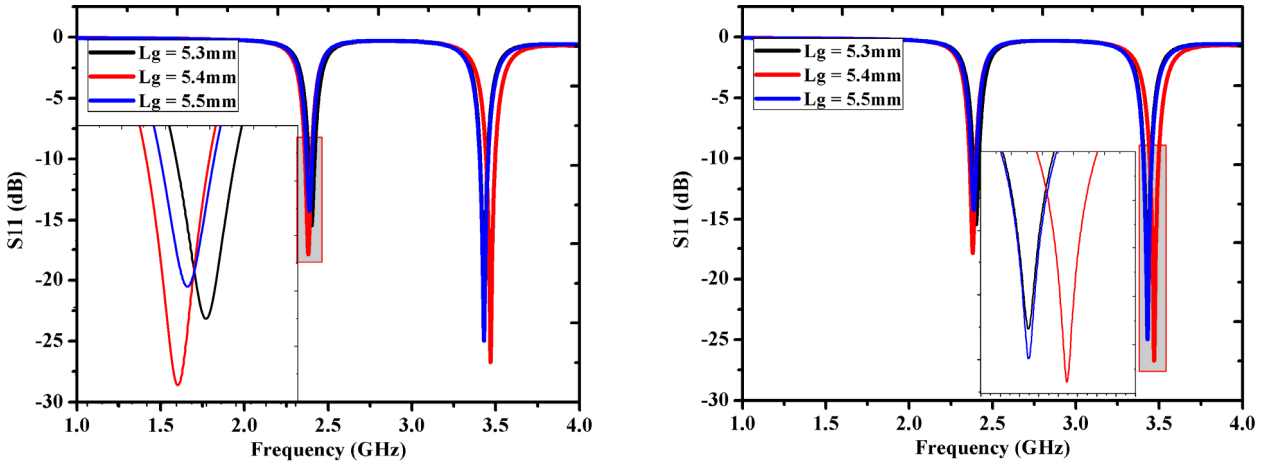

Fig. 6. Influence of ground length (L_g) variation on S_{11}.

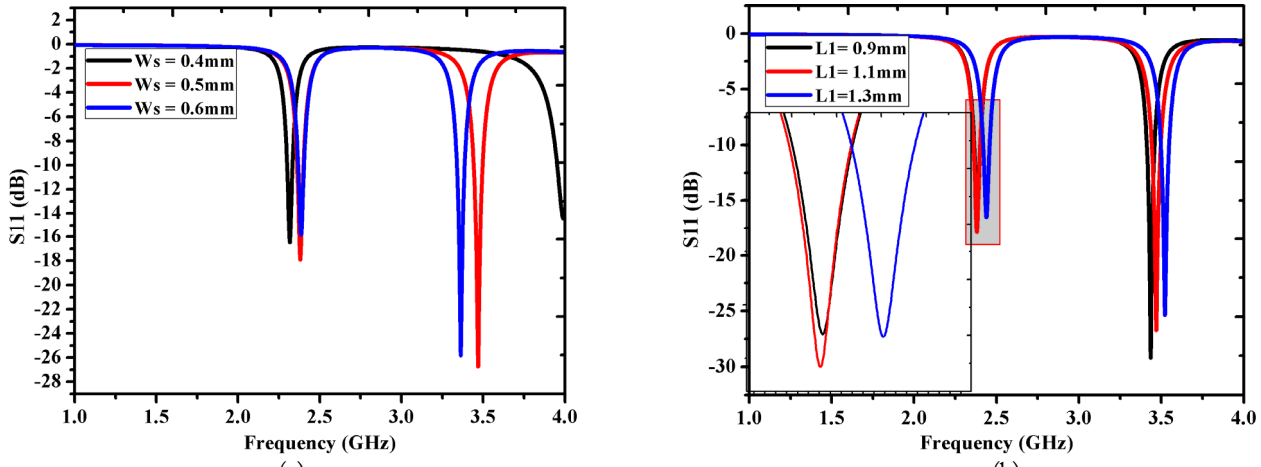

Fig. 7. Influence on S_{11} by variation of the rectangular strip: (a) width (W_s) and (b) length (L_1).

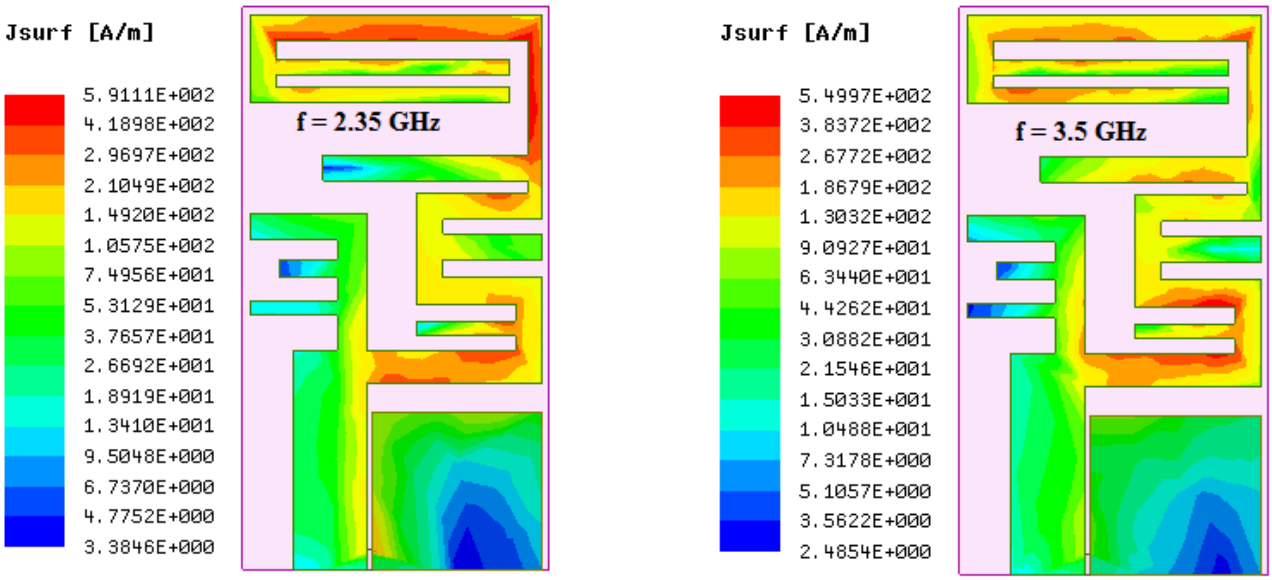

Fig. 8. Current distribution at (a) 2.35 GHz and (b) 3.5 GHz.

radiation pattern considered is in the XY-plane. The obtained "8" shape radiation pattern reveals the omnidirectional radiation behaviour.

IV. Fabricated Antenna and Results

The simulated antenna using High Frequency Structure Simulator (HFSS) software was fabricated in single-side copper plated FR4 substrate with a relative permittivity of 4.4 and is depicted in Fig. 10. The overall dimension of the fabricated antenna was $0.13\lambda \times 0.083\lambda \times 0.0125\lambda$ mm^3, where "λ" is the lowest resonant frequency (2.35 GHz) of the operating band. The reflection coefficient and voltage standing wave ratio (VSWR) of the fabricated antenna was measured using an N9915A network analyser, which is shown in Fig. 8. The fabricated antenna provided dual band operation with a good reflection coefficient, ≤ –15 dB.

Reflection coefficient (S_{11}) is the parameter that indicates the impedance mismatch level in the antenna design. This in turn provides the evidence of VSWR. In terms of S_{11}, VSWR is given by $(1 + S_{11})/(1 - S_{11})$. The simulated and measured reflection coefficient is shown in Fig. 11(a). The minimum reflection coefficient was –17.904 and –26.5 dB for 2.36–2.4 GHz (LTE band-40) and 3.44–3.5 GHz (5G mid-band) frequency bands, respectively.

The measured minimum S_{11} value was –32.433 and –22.92 dB for the frequency bands of 2.23–2.35 GHz (LTE band-40) and 3.3–3.6 GHz (5G mid-band), respectively. The fabricated antenna operated in a wide band due to the soldering of an SMA connector or due to fabrication tolerance. The measured

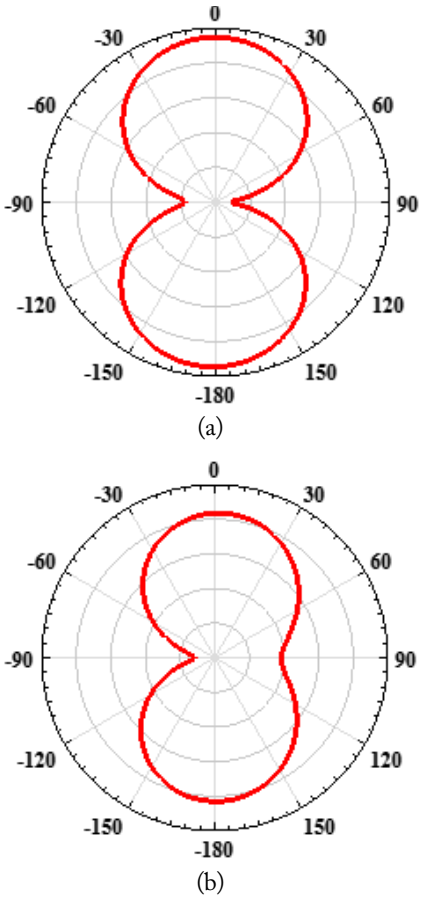

Fig. 9. Radiation pattern for $\phi = 0^o$ at (a) 2.35 GHz and (b) 3.5 GHz.

VSWR ranged between one and two for the operating frequency band and is depicted in Fig. 11(b).

The peak gain obtained for the simulated antenna was 1.05

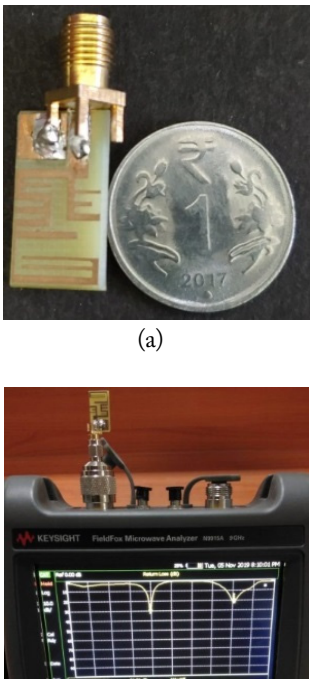

(a) (b)

Fig. 10. (a) Fabricated antenna and (b) Measurement setup.

dBi and 0.63 dBi for the LTE band-40 and 5G mid-band, respectively. Radiation efficiency is defined as the ratio of the power radiated to the amount of power accepted by the antenna at its input. Radiation efficiency (η) is based on the gain (*G*) and directivity (*D*) of the antenna and is given by $\eta = G/D$. The corresponding radiation efficiencies of the designed antenna for LTE band-40 and 5G mid band was 70% and 34.91%, respectively. The truncated ground and the insertion of small rectangular strips provided the desired operating frequency with comprise in the radiation efficiency in 5G mid-band. Table 2 shows the comparison of the proposed antenna with the existing designs in the literature. With compact size and ACS feed, the proposed antenna could operate in dual band, with a gain greater than 0.5 dBi.

V. Conclusion

Using simple rectangular radiating strips, a dual band operating antenna was proposed. The designed antenna could operate in LTE band-40 and 5G mid-band mobile communication applications. The use of particular length and width for a rec-

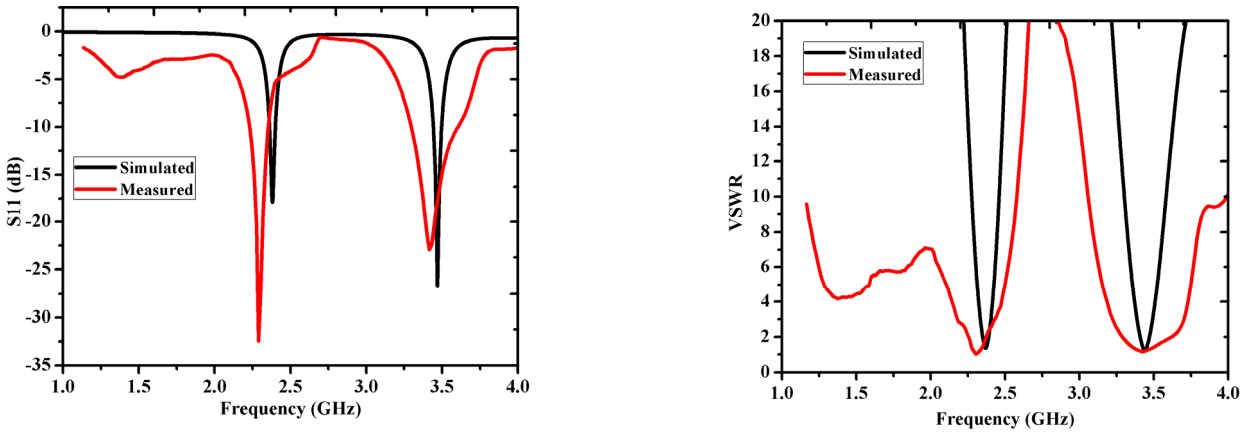

(a) (b)

Fig. 11. (a) Antenna reflection coefficient characteristics and (b) VSWR characteristics.

Table 2. Comparison of the proposed antenna size with state-of-the-art studies

Study (Ref.)	Year	Antenna size (mm^3)	Design structure	Operating resonant frequency (GHz)	Feeding mechanism
[1]	2014	21 × 7.35 × 1.6	L-shape	5.5	ACS
[4]	2019	10 × 19 × 1.6	Meander line	2.4, 5.5	ACS
[7]	2019	16 × 26 × 1.6	Mouse-shape	2.3, 3.5, 5.9	ACS
[8]	2018	25.8 × 20 × 1.6	F-shape	1.89, 3.5, 5.5	Microstrip
[9]	2019	40 × 30 × 1.6	Meander line conformal antenna	2.45, 3.5	Asymmetric CPW
[10]	2017	29 × 29 × 1.6	Square and circular slot	2.4, 5.5	Microstrip
[11]	2015	55 × 57 × 1.6	L-shape strip	2.4, 3.5	CPW
[12]	2019	40 × 40 × 1.6	Slit-loaded semi-circle	5, 8, 10	Asymmetric microstrip
Proposed antenna		19.25 × 10.5 × 1.6	Meander line	2.35, 3.6	ACS

tangular strip in the proposed design was discussed in detail. In terms of size, the proposed antenna geometry ($19.25 \times 10.5 \times 1.6$ mm^3) is compact and is designed in a low cost FR4 substrate. The designed antenna was fabricated and verified experimentally. The achieved frequency of operation was 2.23–2.35 GHz (LTE band-40) and 3.3–3.6 GHz (5G mid-band).

REFERENCES

[1] K. A. Ansal and T. Shanmuganatham, "ACS-fed wide band antenna with L-shaped ground plane for 5.5 GHz WLAN application," *Progress In Electromagnetics Research*, vol. 49, pp. 59-64, 2014.

[2] D. Sharma, "Asymmetric coplanar strip fed monopole," *International Journal of Electronics and Communication Engineering*, vol. 6, pp. 153-164, 2013.

[3] Y. Yang, Y. A. Liu, and F. Wu, "Compact ACS-fed quad-band antenna for LTE/WLAN/5G applications," in *Proceedings of the 2nd International Conference on Telecommunications and Communication Engineering*, Beijing, China, 2018, pp. 205-208.

[4] P. V. Naidu, A. Kumar, and R. Rajkumar, "Design, analysis and fabrication of compact dual band uniplanar meandered ACS fed antenna for 2.5/5 GHz applications," *Microsystem Technologies*, vol. 25, no. 1, pp, 97-104, 2019.

[5] Y. F. Liu, P. Wang, and H. Qin, "A compact triband ACS-fed monopole antenna employing inverted-L branches for WLAN/WiMAX applications," *Progress In Electromagnetics Research*, vol. 47, pp. 131-138, 2014.

[6] S. Weigand, G. H. Huff, K. H. Pan, and J. T. Bernhard, "Analysis and design of broad-band single-layer rectangular U-slot microstrip patch antennas," *IEEE Transactions on Antennas and Propagation*, vol. 51, no. 3, pp. 457-468, 2003.

[7] P. V. Naidu, A. Kumar, and R. Rengasamy, "Uniplanar ACS fed multiband high-gain antenna with extended rectangular strips for portable system applications," *International Journal of RF and Microwave Computer-Aided Engineering*, vol. 29, no. 10, article no. e21870, 2019.

[8] C. V. Anil Kumar, B. Paul, and P. Mohanan, "Compact-triband dual F-Shaped antenna for DCS/WiMAX/WLAN applications," *Progress In Electromagnetics Research*, vol. 78, pp. 97-104, 2018.

[9] R. Sahoo and D. Vakula, "Compact metamaterial inspired conformal dual-band antenna loaded with meander lines and fractal shaped inductor for Wi-Fi and WiMAX applications," *IET Microwaves, Antennas & Propagation*, vol. 13, no. 13, pp. 2349-2359, 2019.

[10] R. H. Patel and T. K. Upadhyaya, "Compact planar dual band antenna for WLAN application," *Progress In Electromagnetics Research*, vol. 70, pp. 89-97, 2017.

[11] M. T. Tan and B. Z. Wang, "A compact dual-band dual-polarized loop-slot planar antenna," *IEEE Antennas and Wireless Propagation Letters*, vol. 14, pp. 1742-1745, 2015.

[12] M. Midya, S. Bhattacharjee, and M. Mitra, "Triple-band dual-sense circularly polarised planar monopole antenna," *IET Microwaves, Antennas & Propagation*, vol. 13, no. 12, pp. 2020-2025, 2019.

[13] W. Ren, S. W. Hu, and C. Jiang, "An ACS-fed F-shaped monopole antenna for GPS/WLAN/WiMAX applications," *International Journal of Microwave and Wireless Technologies*, vol. 9, no. 5, pp. 1123-1129, 2017.

[14] A. Desai, T. Upadhyaya, and M. Palandoken, "Dual band slotted transparent resonator for wireless local area network applications," *Microwave and Optical Technology Letters*, vol. 60, no. 12, pp. 3034-3039, 2018.

[15] A. Ambika, C. Tharini, and M. T. Ali, "Novel D SRR-based dual band antenna for WiMAX/C applications," *Microwave and Optical Technology Letters*, vol. 61, no. 2, pp. 309-315, 2019.

[16] J. S. McLean, "A re-examination of the fundamental limits on the radiation Q of electrically small antennas," *IEEE Transactions on Antennas and Propagation*, vol. 44, no. 5, pp. 672-676, 1996.

[17] S. R. Best, "The performance properties of electrically small resonant multiple-arm folded wire antennas," *IEEE Antennas and Propagation Magazine*, vol. 47, no. 4, pp. 13-27, 2005.

Shine Let Gunamony

received her M.E. degree in Communication Systems from the SSN College of Engineering, Anna University, India in 2007. Her research interests are in wireless networks, multi-band antenna design, reconfigurable antenna design, and optimization techniques.

Josemin Bala Gnanadhas

received her bachelor's degree from Bharathidasan University, Tiruchirappalli, in 1996, and her master's degree from REC, Trichy in 1999. She was honored with a Ph.D. from Anna University, Tamilnadu in 2008. Currently she is working in the Department of Electrical and Computer Engineering, Karunya Institute of Technology and Sciences, Coimbatore as a professor. She is interested in research on RF systems and Communication Networks. Her works have been published in a number of proceedings and indexed journals. Recently, she was awarded for her excellence as a woman educator by NFED in 2017 for her contributions and achievements in the field of engineering. She is an IEEE Senior Member, an associate member of the Institution of Engineers (India) and a life member of ISTE.

Diana Evangeline Lawrence

received her B.E. degree in Electronics and Communication Engineering from Saranathan College of Engineering, Tiruchirapalli, India in 2018. She completed M.Tech. degree in Communication Systems at Karunya Institute of Technology and Sciences, Coimbatore, India in 2020. Her research interests include multiband antenna design and reconfigurable antenna design.

JOURNAL OF ELECTROMAGNETIC ENGINEERING AND SCIENCE, VOL. 20, NO. 3, 221~233, JUL. 2020

https://doi.org/10.26866/jees.2020.20.3.221
ISSN 2671-7263 (Online) · ISSN 2671-7255 (Print)

Hybrid Metamaterial for the Secondary Radar Antenna System

Peerasan Khamsalee* · Piyaporn Mesawad · Rangsan Wongsan

Abstract

This paper proposes the gain enhancement of dual-band and dual-polarized asymmetric horn antenna for the secondary radar system using hybrid metamaterial techniques. The hybrid metamaterial is comprised of the structures of woodpile electromagnetic bandgap (EBG) for gain enhancement of the primary main beam of the radar system at the operating frequency of 1,300 MHz with horizontal polarization; and the wire medium structure that is placed beside the EBG structure for gain improvement of the identification friend or foe (IFF) main beam, which is operated at the center frequency of 1,060 MHz with vertical polarization. Meanwhile, the cooperated structures have to function to control the directions of the primary and IFF main beams retaining at 0° and 6°, respectively, too. When the hybrid metamaterial structure is placed at the front of an asymmetric horn's aperture, with suitable parameters and optimized spacing, it is found to increase the gains of the two beams compared to the single asymmetric horn around 3 dB and retain the directions of original main beams. The comparison of the results between simulation and measurement, such as the reflected power (S_{11}), gain, and radiation patterns, are in good agreement.

Key Words: Gain Enlargement, Electromagnetic Band Gap, Horn Antenna, Secondary Radar, Wire Medium.

I. Introduction

Radio detection and ranging (RADAR) is a method of using electromagnetic waves to remotely sense the velocity, position, and identifying characteristics of targets [1]. The secondary radar system is another type of radar that is widely used for detecting distant targets. The secondary radar system has two main operating systems. The first deals with detecting and reporting the position of a target by transmitting a periodic pulse signal to the target and receiving the reflected signal back. The second is used to identify the detected target using the identification friend or foe (IFF) system, in which the IFF signal is transmitted to the target and the answered message is received back. To avoid interference between two adjacent frequency bands of the radar system, orthogonal polarization has been used in the rectangular horn antenna as a feeder of the reflector antenna that is commonly used in radar systems.

There are two ways to improve the radiated efficiency of the radar system: (1) increase the transmitting power or (2) enhance the gain of the antenna. In this paper, we focus on the gain improvement of the primary feeder of the reflector antenna as an alternative to enlarging the dimension of the reflector. The primary feeder of DR-172 ADV medium-altitude radar, which is our reference radar, uses one asymmetric rectangular horn for feeding electromagnetic waves to the reflector with the dual-frequency bands (1,215–1,365 MHz for target detection and 1,030–1,090 MHz for target identification), dual-polarization, and different main beam direction.

Manuscript received October 14, 2019 ; Revised April 10, 2020 ; Accepted July 16, 2019. (ID No. 20191014-086J)
School of Telecommunication Engineering, Suranaree University of Technology, Nakhon Ratchasima, Thailand.
*Corresponding Author: Peerasan Khamsalee (e-mail: d5840496@g.sut.ac.th)

In the current research, the methods for performance enhancement of the antenna were reported by using the new technology, which is called a metamaterial structure since it can increase the radiation efficiency of microwave antennas [2, 3]. The properties of the metamaterial result from the composition and the combination of materials, where the structural dimension is considerably smaller compared to the given wavelength. Furthermore, the permeability and permittivity of metamaterial are zero or near-zero, and the reflective index is a negative quantity [4, 5]. The electromagnetic bandgap (EBG) is a type of the metamaterials with a periodic structure; these materials are known as photonic crystals [6] or photonic bandgap materials. However, the EBG structures are usually realized by a periodic arrangement of dielectric material and metallic conductors. In general, the EBG can be classified into three groups according to a geometric configuration: one-dimensional transmission line, two-dimensional planar surface, and three-dimensional volumetric structure. The woodpile EBG is the selected technique for increasing the gain of an asymmetric rectangular horn in this paper since its 3D structure is very suitable for locating at the front of the horn's aperture to receive the EM energy from the aperture and pass through its own structure into space. The woodpile EBG structures were used as the resonator antennas by locating them above the ground plane of the different feeding antennas (i.e., the double slot and microstrip patch antennas). This paper reports that the woodpile EBG material was able to create highly directional patterns [7]. In addition, the woodpile EBG was designed as a cylindrical structure to cover the monopole antenna, resulting in an increase in the gain of the monopole antenna [8].

Furthermore, from [9, 10], the quadratic-shaped woodpile EBG structure was used to enhance the gain of any horn antenna by its placement at the front of the horn's aperture with optimized spacing. In 2016, Kamphikul and Wongsan [11] continued to develop the cavity of curved woodpile EBG structure for the enhancement of the gain of the slot array antenna instead of increasing the number of slots on the array. Nevertheless, the wire medium is another metamaterial that has a woodpile EBG-type structure [12, 13]. The electromagnetic properties of the wire medium structure designed at the plasma frequency are near zero permittivity or permeability [14]. Tomaz et al. [15] proposed the use of the wire medium structure for decreasing the sidelobe level of the radiation patterns and increasing the directivity of the traditional horn antenna by using five layers of wire embedded in the Styrofoam dielectric. The wire medium was also applied to the horn antenna to reduce the length of the horn, whereas the aperture size of the horn did not change [16]. Later studies [17, 18] reported on the influence of different wire medium structures placed at the front of the aperture of the horn antenna, resulting in higher gain and lower sidelobe level in traditional horns. From the literature review, we found that both metamaterial structures installed in front of the aperture can increase the gain of the horn antenna. Therefore, this paper proposes the gain enhancement of dual-band and dual-polarized asymmetric horn antenna for secondary radar system using a hybrid metamaterial technique. The proposed hybrid structure comprises woodpile EBG to encourage the first beam for the target detection of the radar system at operating frequency 1,300 MHz with horizontal polarization and a wire medium for improving the second beam for the IFF system at operating frequency 1,060 MHz with vertical polarization. Simultaneously, the proposed structure is capable of treating both main beam directions as the same as the original asymmetric horn provided.

First, the design and configurations of a horn antenna and the hybrid metamaterial are described in Sections II. Second, the simulated results and discussion of all parts of the structure are demonstrated in Section III. Third, the measured results of the established prototype antenna are shown in Section IV. Fourth, the simulated results of the horn antenna and the hybrid metamaterial with the reflector are shown in Section V. Lastly, the conclusions are given in Section VI.

II. Horn Antenna and Hybrid Metamaterial Configurations

1. An Asymmetric Rectangular Horn Antenna

Fig. 1 shows the structure of the asymmetric horn antenna, which was modelled from an original horn of DR-172 ADV radar system by Daimler-Chrysler Aerospace, Germany, and was designed to support the dual-frequency band and dual-polarization to function as a feeder of the main reflector antenna of this radar system. The first beam of the feeding horn was designed for target detection of the radar system at an operating frequency of 1,300 MHz with horizontal polarization. Simultaneously, the second beam of this horn was designed for transceiving the IFF signals between the radar station and targets (aircraft) with vertical polarization at frequencies of 1,030 MHz (Tx) and 1,090 MHz (Rx). Moreover, this feeding horn was also designed to control two main beams for target detection and IFF transceiving of the radar systems with different directions at 0° and 6°, respectively. It also provides the gain for target detection beam at 10.85 dBi, and the gains for the IFF beam at 12.39 dBi (Tx) and 12.51 dBi (Rx), respectively.

2. Hybrid Metamaterial Configurations

To improve the gains of this asymmetric horn antenna, we use the combination of woodpile EBG and wire medium structures, which is the hybrid metamaterial that controls the performance of the electromagnetic wave. However, to design the

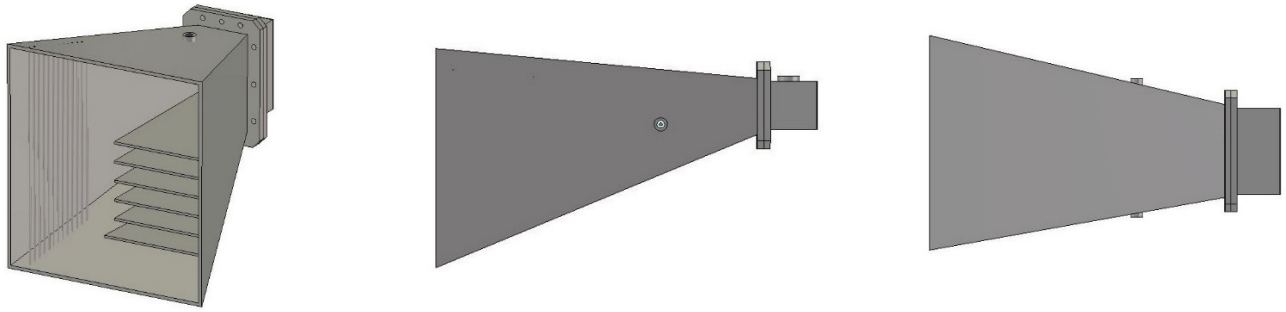

(a) (b) (c)

Fig. 1. Structure of asymmetric horn antenna: (a) perspective view, (b) top view, and (c) side view.

proposed hybrid metamaterial, we separated the structure into two parts, namely, structures of woodpile EBG and wire medium, respectively. First, the woodpile EBG structure is designed to be the 3D periodic structure made from the dielectric material (superlene rods with ε_r =3.3), as shown in Fig. 2, for the enhancement of the directive gain of the target detection beam at the operating frequency of 1,300 MHz. This EBG structure is placed at the front of an asymmetric horn with the suitable position and spacing to fully support the illumination of waves from the boresight of the target detection beam from the horn aperture. In Fig. 2, the given parameters of the unit cell of the woodpile EBG structure are the height of rods (h_1) in layer 1 and 3, the height of rods (h_2) in layer 2 and 4, the length of rods (a), the width of rods (w) and the total height of unit cell (b). These proper parameters of the unit cell are optimized and simulated using CST Studio Suite Software. In the first step, we simulate the impact of the length of rods (a) in a unit cell versus the reflected power (S_{11}) to consider the resonant frequency response, as shown in Fig. 3. It is found that the resonant frequency increases as the rod length increase. Fig. 4 shows the comparison of the simulated reflected power versus the different heights of two rods (h_1) in layers 1 and 3. We found that the resonant frequency increases as the rod height decreases. In addition, if the height of the other two rods (h_2) in layers 2 and 4 is decreased, the resonant frequency is shifted to a higher frequency,

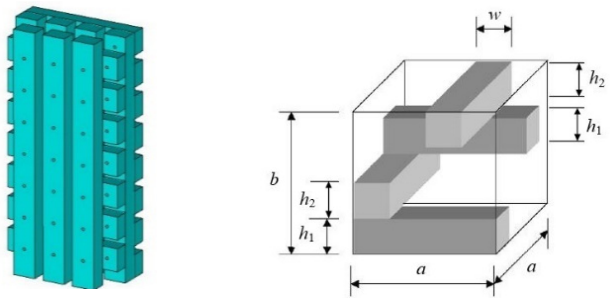

(a) (b)

Fig. 2. Structure of woodpile EBG: (a) periodic structure and (b) unit cell.

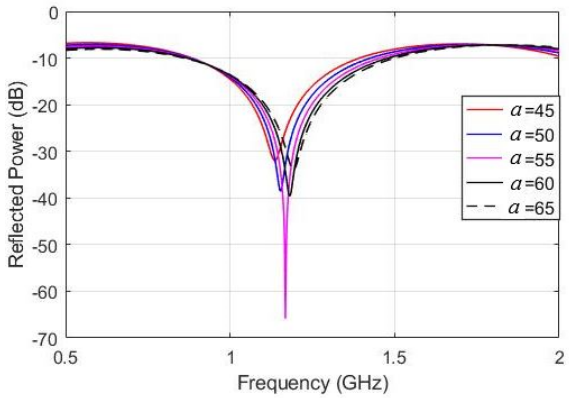

Fig. 3. The simulated reflected power (S_{11}) versus the different lengths (a) of dielectric rods.

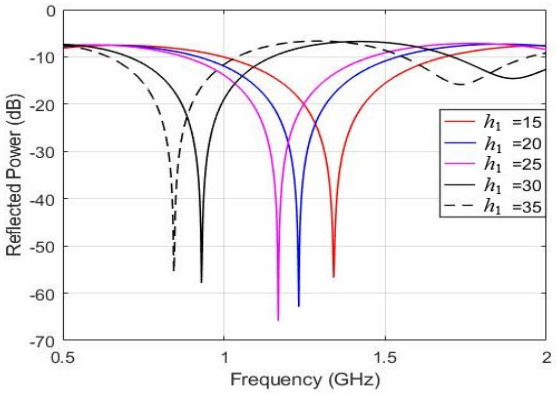

Fig. 4. The simulated reflected power (S_{11}) versus the different heights (h_1) of dielectric rods in layers 1 and 3.

as shown in Fig. 5. Next, the influence of the width on the resonant frequency is considered, as shown in Fig. 6. We found that the resonant frequency decrease as the rod width decreases. Lastly, the most appropriate parameters of a unit cell of the woodpile EBG structure are summarized as follows: a = 55 mm, h_1 = 25 mm, h_2 = 30 mm, b = 110 mm, and w = 40 mm.

From a single unit cell in Fig. 2(b), the 21 unit cells are assembled by arranging the dielectric rods in a 3 × 7 pattern, as shown in Fig. 2(a). With a 450 mm spacing between the EBG

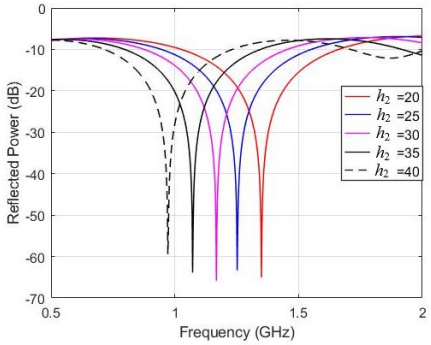

Fig. 5. The simulated reflected power (S_{11}) versus the different heights (h_2) of dielectric rods in layers 2 and 4.

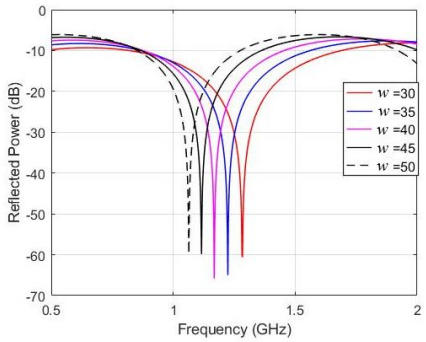

Fig. 6. The simulated reflected power (S_{11}) versus the different widths (w) of dielectric rods.

structure and horn aperture, we found that the structure yields a bandgap of 1.05 GHz to 1.37 GHz at $S_{11} = -15$ dB, covering the resonant frequency of 1,060/1,300 MHz and the overall bandwidth of the horn antenna (Fig. 7). However, we found that the directions of the two beams did not conform to the requirements.

Therefore, to compensate for the diffraction of waves on the left side of the EBG structure, we extended and varied the length of the dielectric rods (W_E) in layers 1 and 3, as displayed in Fig. 8, to control the different directions of the two beams, as illustrated in Table 1. We found that with the length of dielectric rods (W_E) at 105 mm, the direction of the target detection and IFF beams of radar are controlled at 0° and 6°, respectively.

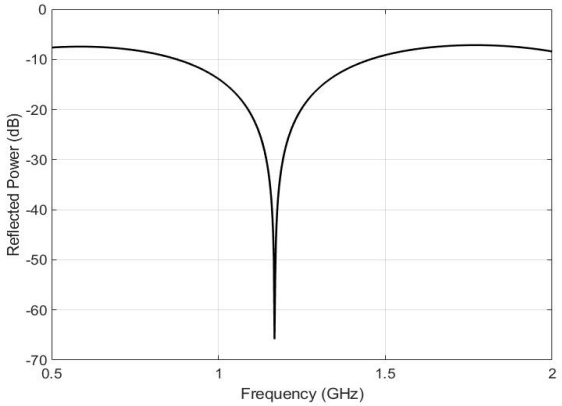

Fig. 7. The simulated reflected power (S_{11}) of woodpile EBG structure before extending the length of the dielectric rods.

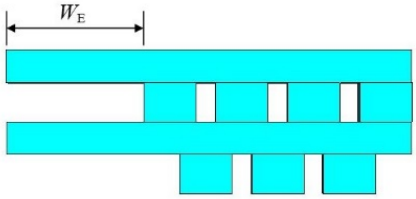

Fig. 8. Structure of woodpile EBG with 3 × 7 dielectric rods (top view).

Table 1. The 1st simulated results of radar beam directions

Length (mm)	Directions of radar beams (°)		
	1,030 MHz	1,090 MHz	1,300 MHz
50	6 (left)	6 (left)	6 (left)
100	6 (left)	6 (left)	3 (left)
105	6 (left)	6 (left)	0
110	4 (left)	5 (left)	1 (right)
115	4 (left)	5 (left)	2 (right)
120	4 (left)	5 (left)	3 (right)

To support the IFF beam operated at 1,030 MHz and 1,090 MHz frequencies with vertical polarization, the wire medium structure uses two layers of the dielectric rods installed at the right side of the EBG structure to improve the gain of the IFF signal (Fig. 9). The parameters of the wire medium structure are as follows: the rod width (W_w), the rod thickness (H_W), the rod height (W_L), the spacing of adjacent rods (W_S) in the same layer, and the spacing between two layers (H_S), which are optimized by CST simulation. From the simulation results, the appropriate parameters are following: $W_w = 45$ mm, $H_W = 30$ mm, $W_L = 535$ mm, $W_S = 16$ mm, and $H_S = 25$ mm.

In Fig. 10, the EBG and wire medium structures with the optimized dimension are combined and simulated to observe the beam behavior.

Table 2 illustrates the directions of radar beams for the IFF signal and target detection when located the combined structure at the front of the horn aperture. We found that the effect from an assembly of two structures causes the directions of both beams to change since the diffraction of waves that have different polarizations at the junction of arrangements are not truly isolated, as displayed in Fig. 11. Consequently, the beam direc-

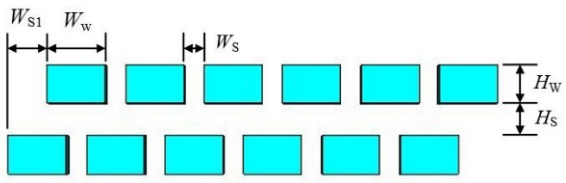

Fig. 9. Structure of wire medium (top view).

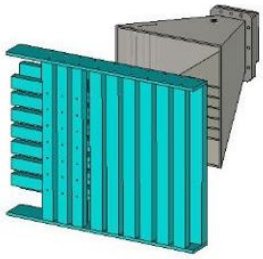

Fig. 10. Combination of EBG and wire medium structures.

Table 2. The 2nd simulated results of radar beam directions

Length (mm)	Directions of radar beams (°)		
	1,030 MHz	1,090 MHz	1,300 MHz
60	6 (left)	6 (left)	2 (right)
65	6 (left)	6 (left)	2 (right)
70	6 (left)	6 (left)	0
75	6 (left)	6 (left)	1 (left)
80	6 (left)	6 (left)	3 (left)

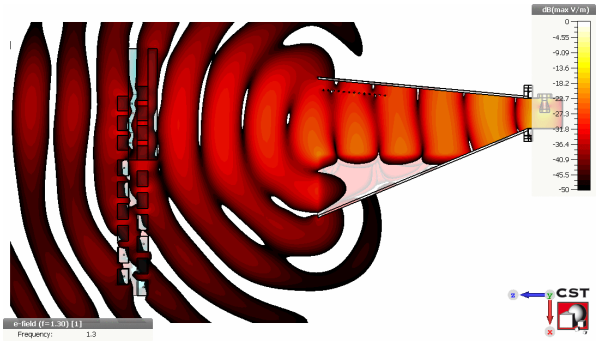

Fig. 11. Show the diffraction of the electric field (at 1,300 MHz) pass through some part of the wire medium structure.

tion of 1,300 MHz is shifted right from 0° to 3°. To reduce the diffraction of the electromagnetic waves from the target detection beam to the wire medium structure, we designed an array of 1 × 6 metallic rods with a 9.53 mm diameter lying in the horizontal line according to a polarization of 1,300 MHz beam with rod spacing (S_S). From the simulation, it is found that the proper spacing between the center of adjacent rods is 35.6 mm by placing the one ends of rods at the front of the horn aperture with suitable distance around 4 mm, as shown in Fig. 12. Furthermore, the length of metallic rods (L_S) is varied to meet the requirements for the directions of two different beams (Table 2). It is observed that the most suitable length (L_S) is 70 mm, providing the beam direction of the frequency of 1,300 MHz back to 0°. However, this rod array could not float in the air without the holder; therefore, we designed the metallic rod holder using the superlene sheet by forming a suitable shape and not obstructing the travelling waves from horn aperture, as shown in Fig. 12(b).

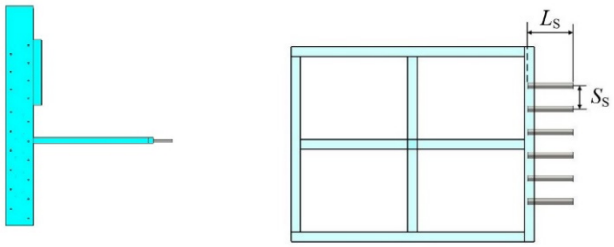

(a) (b)

Fig. 12. The 1 × 6 metallic rods with a dielectric holder: (a) top-view and (b) side view.

III. Simulated Results and Discussions

The configuration of an asymmetric horn antenna combined with a hybrid metamaterial structure is shown in Fig. 13. The essential parameters of the original asymmetric horn antenna and asymmetric horn antenna with the proposed hybrid metamaterial, such as the reflected power for 1,300 MHz (S_{11}) and 1,060 MHz (S_{22}), the radiation patterns and gain are simulated using CST software.

Fig. 14 shows the comparison for the reflected power of the target detection beam (S_{11}) and the IFF beam (S_{22}) at the center frequencies of 1,300 MHz and 1,060 MHz, respectively. The frequency responses of the asymmetric horn are still similar after adding the hybrid metamaterial structure with a bandwidth of 1,084–1,504 MHz and 1,026–1,098 MHz at $S_{11} = -15$ dB, as shown in Fig. 14(a) and (b), respectively.

The simulated results of the normalized radiation pattern at the operating frequencies of 1,030 MHz, 1,090 MHz, and

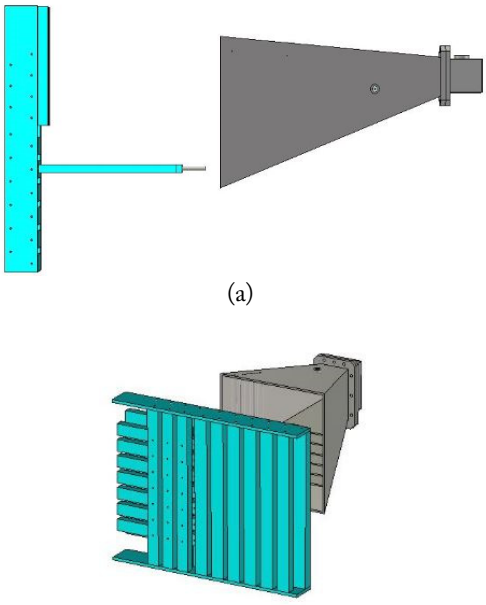

(a)

(b)

Fig. 13. The configuration of the proposed antenna: (a) top view and (b) perspective view.

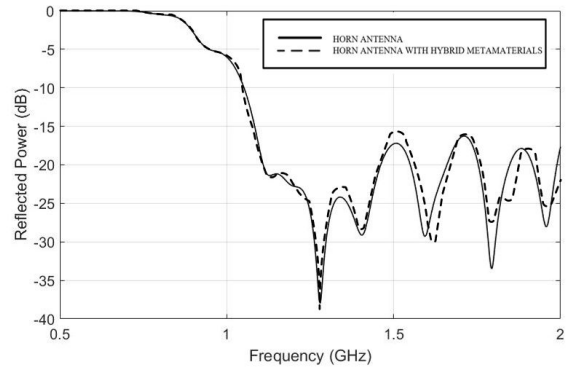

(a)

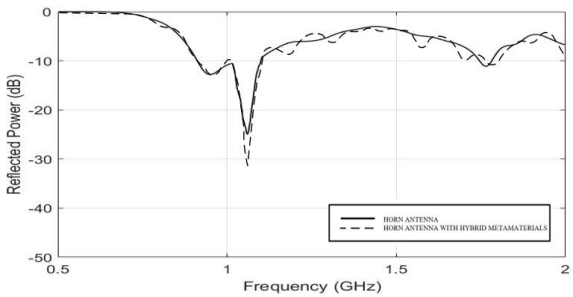

(b)

Fig. 14. The comparison of reflected power: (a) for target detection beam (S_{11}) and (b) for IFF beam (S_{22}).

Table 3. Simulation parameters of the single asymmetric horn without/with the hybrid metamaterial

	Parameter	Horn antenna		Horn antenna with hybrid MM	
		E	H	E	H
1,030 MHz	Gain (dBi)	12.39		15.64	
	Main beam dir. (°)	1	6	0	6
	HPBW (°)	36.5	49.2	25.2	28.2
1,090 MHz	Gain (dBi)	12.51		15.55	
	Main beam dir. (°)	1	6	0	6
	HPBW (°)	35.9	48.1	24.1	26.8
1,300 MHz	Gain (dBi)	10.85		14.04	
	Main beam dir. (°)	0	0	0	1
	HPBW (°)	62.0	43.9	32.0	26.4

MM = metamaterial, dir. = direction, E = E-plane, H = H-plane.

1,300 MHz in both E- and H-plane are compared and shown in Fig. 15. We found that the hybrid metamaterial can control the difference of beam directions of both systems, which was retained at 0° in the E-plane of the target detection beam and 6° in the H-plane of the IFF beam. However, the half-power beamwidths (HPBWs) obtained from the proposed hybrid metamaterial are somewhat narrower than those of the single asymmetric horn. As a result, the gains achieved from the hybrid metamaterial at the operating frequencies of 1,030 MHz, 1,090 MHz, and 1,300 MHz are 15.64 dBi, 15.55 dBi, and 14.04 dBi, respectively. It is shown that the hybrid metamaterial can increase the gains around 3 dB at all operating frequencies, as shown in Table 3. The simulated results of the radiation patterns of both cases are displayed in Fig. 15.

IV. Measured Results and Discussions

The prototype of an asymmetric horn antenna with a hybrid metamaterial was assembled and tested in the semi-anechoic chamber at Electrical and Electronic Products Testing Center (PTEC), Thailand, as shown in Fig. 16. The simulated and measured reflected powers (S_{11}, S_{22}) for the prototype are shown in Fig. 17. The measured and simulated results are in good agreement. The bandwidth of the given operating frequencies is retained according to the requirement. In Fig. 18, the normalized radiation patterns obtained from the simulation and measurement are compared. We found that the measured patterns are somewhat similar to the simulated results. It is also observed that the measured results of the beam directions are retained in the desired direction, as per the simulated results. In Table 4, we mention the obtained parameters from simulation and measurement for comparison. The measured gains obtained from an asymmetric horn with the proposed hybrid metamaterial are higher than that of a single horn around 3.05 dBi, 3.03 dBi, and 3.25 dBi. In contrast, the simulated gains are higher than approximately 3.25 dBi, 3.04 dBi, and 3.19 dBi at the frequencies of 1,030 MHz, 1,090 MHz, and 1,300 MHz, respectively. Moreover, we also compared the simulated and measured results of the sidelobe level and HPBW in both the E- and H-planes (Table 4).

In Fig. 18, the simulated and measured radiation patterns in E- and H-planes at the operating frequencies of 1,030 MHz, 1,090 MHz, and 1,300 MHz are compared and displayed. The shapes of the radiation patterns in each plane of each frequency are somewhat similar. Nevertheless, we found that the measured radiation patterns in some planes yielding the sidelobe level were slightly higher than that of the simulated results such as H-plane of 1,030 MHz, E-plane of 1,090 MHz, and H-plane of 1,300 MHz, as shown in Fig. 18(b), (c), and (f), respectively.

V. Horn Antenna and Hybrid Metamaterial with Reflector

To verify that the modified feeding antenna is assembled from an asymmetric horn and the proposed hybrid metamaterial using the CST simulation software. We modelled an offset-fed reflector by importing the structure of 8.3 m in diameter, and f/D ratio equals to 0.34 of the paraboloidal reflector with a horn feed at the position of its focal point (around 2.8 m from the

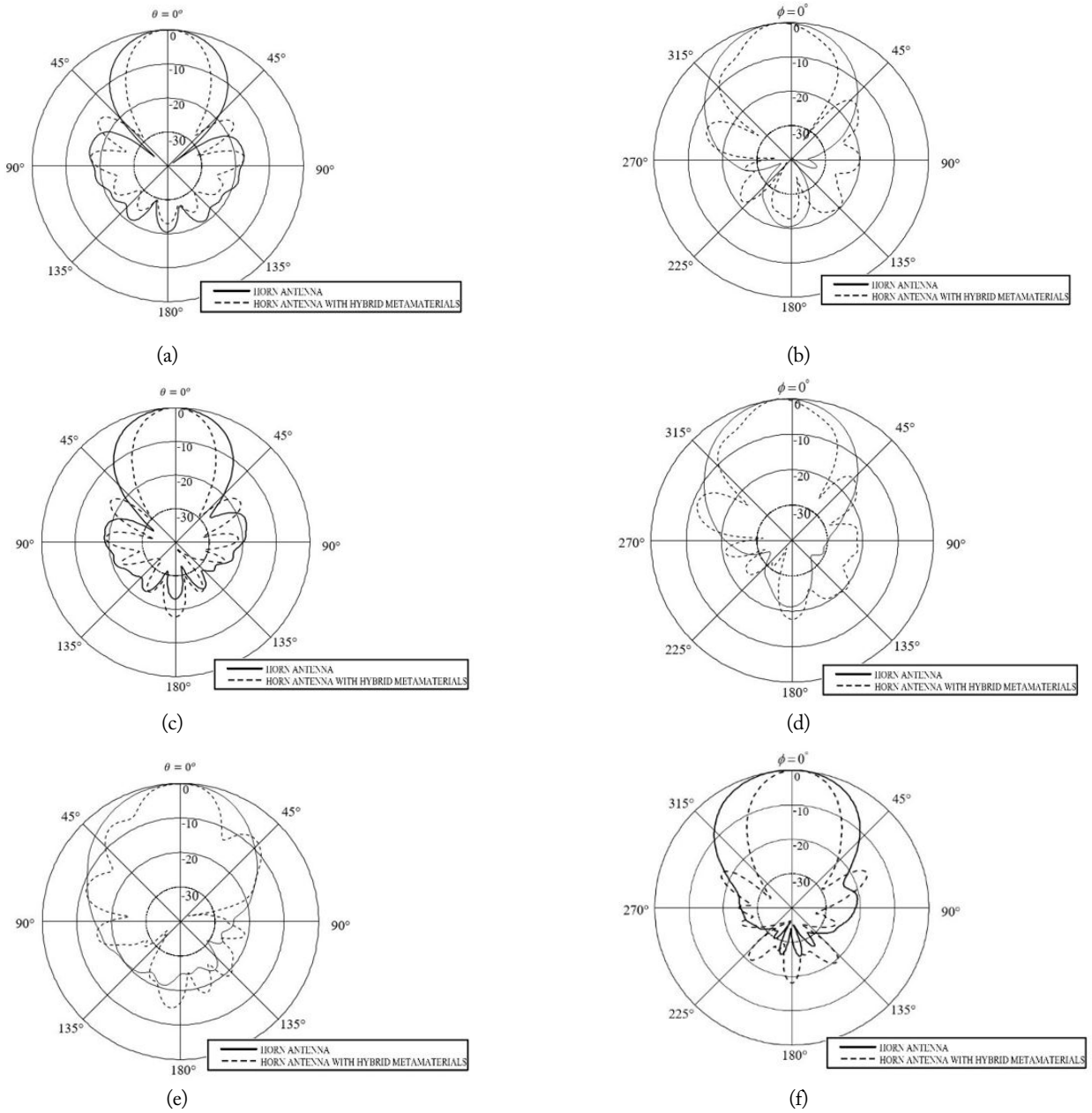

Fig. 15. Comparison of simulated radiation patterns of a single asymmetric horn without/with hybrid metamaterial: (a, c, e) E-planes and (b, d, f) H-planes at operating frequency of 1,030 MHz, 1,090 MHz, and 1,300 MHz, respectively.

Fig. 16. The measurement setup for fabricated hybrid metamaterial with an asymmetric horn antenna in anechoic chamber: (a) side view and (b) perspective view.

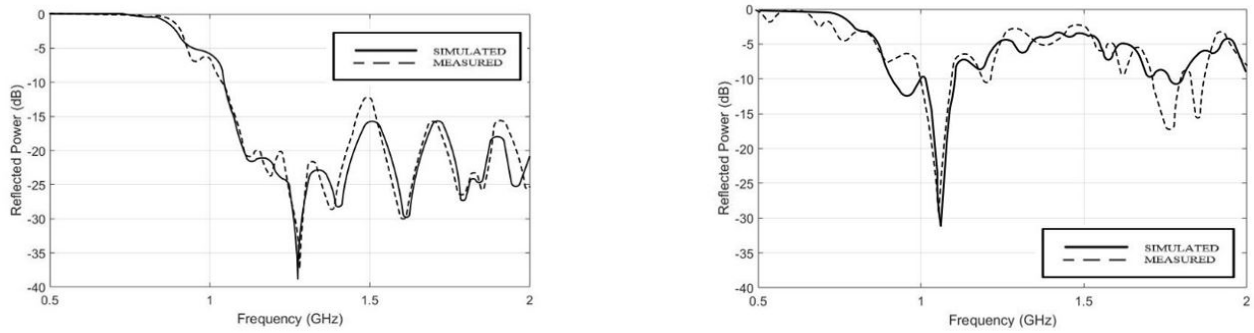

Fig. 17. The comparison of reflected power: (a) main radar (S_{11}) and (b) IFF systems (S_{22}).

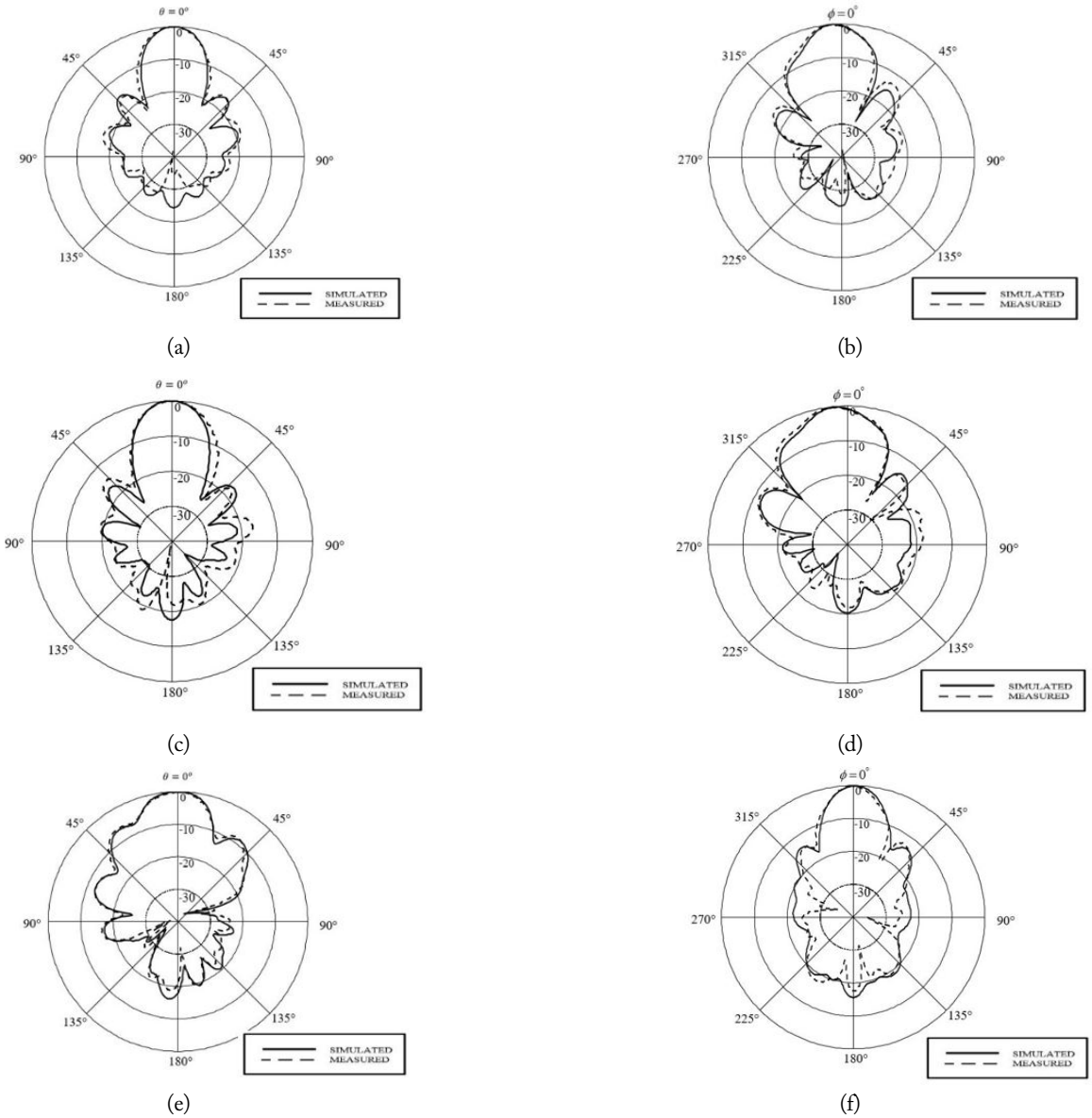

Fig. 18. Comparison of simulated and measured radiation patterns of an asymmetric horn with hybrid metamaterial: (a, c, e) E-planes and (b, d, f) H-planes at operating frequency of 1,030 MHz, 1,090 MHz, and 1,300 MHz, respectively.

vertex) from the CST library. Only the upper portion of the reflector is selected and modified by referring to the real structure of an offset-fed reflector of the DR-172 ADV radar system having the aperture dimensions of approximately 7.2 m and 3.5

Table 4. Comparison of simulated and measured parameters of single asymmetric horn without/with hybrid metamaterial

	Parameter	Horn antenna				Horn antenna with hybrid MM			
		Simulation		Measurement		Simulation		Measurement	
		E	H	E	H	E	H	E	H
1,030 MHz	Gain (dBi)	12.39		11.16		15.65		14.21	
	Main beam dir. (°)	1	6	0	6	0	6	0	6
	HPBW (°)	36.5	49.2	40.0	51.0	25.2	28.2	25.0	29.0
	SSLs (dB)	-18.4	-	-16.63	-24.48	-17.0	-15.5	-17.97	-13.32
1,090 MHz	Gain (dBi)	12.51		11.12		15.55		14.15	
	Main beam dir. (°)	1	6	2	6	0	6	0	6
	HPBW (°)	35.9	48.1	39.0	52.0	24.1	26.8	25.0	29.0
	SSLs (dB)	-18.2	-	-15.46	-	-16.8	-12.4	-14.95	-13.32
1,300 MHz	Gain (dBi)	10.85		10.50		14.04		13.75	
	Main beam dir. (°)	0	0	0	1	0	1	0	0
	HPBW (°)	62.0	43.9	65.0	40.0	32.0	26.4	29.0	23.0
	SSLs (dB)	-	-17.6	-	-29.79	-6.8	-13.9	-8.57	-13.71

MM = metamaterial, dir. = direction, E = E-plane, H = H-plane, SSL = sidelobe level.

m in width and height, respectively. The radiation pattern of an asymmetric horn with hybrid metamaterial is offset, as displayed in Fig. 19. Therefore, it illuminates only the upper portion of the reflector. Even though the metamaterial structure is installed at the front of the asymmetric and its top edge is over the top edge of the horn at approximately 0.49 m, the proposed feeder still is in a position that is well clear of the main beam. Therefore, no obstruction occurs [19]. However, in the process of simulating the performance of the offset-fed reflector antenna excited by an asymmetric horn with hybrid metamaterial, we can use one feature of CST simulation software. That is the far-field sources that are available as excitation for the integral equation solver instead of simulation by using a model of horn directly. Therefore, the far-field source data obtained from the simulated patterns, which are illustrated and explained in Section III, is imported and functions as the new source for the primary reflector, as described with graphic images in Fig. 19(b)–(g).

Even though the HPBWs obtained from the proposed hybrid metamaterial are somewhat narrower and the sidelobes occur more than those of the single asymmetric horn, they are still limited in the envelope of the original main beams obtained from a single horn. To verify that the appearance of the sidelobes does not affect the sidelobes resulting from waves reflection on the surface of the offset-fed reflector. The simulated results, as shown in Fig. 20, can be considered.

In Fig. 20, we found that the elevation beam angles with vertical polarization for 1,060 MHz of the center frequency for the IFF band are lifted at 10°, which is the same as that of the target detection beam at 1,300 MHz with horizontal polarization, as shown in Fig. 20(a) and (d), respectively. The beam directions in the azimuthal angle of the IFF and target detection systems are maintained at 6° and 0°, which followed the requirement, as shown in Fig. 20(b) and (c), respectively. Furthermore, the obtained sidelobes of all cases are in the standard of the Federal Communications Commission (≤–20 dB).

We found that the gains of a single asymmetric horn with the reflector are approximately 23.31 dBi, 23.56 dBi, and 21.74 dBi at the operating frequency of 1,030 MHz, 1,090 MHz, and 1,300 MHz, respectively. Once the hybrid metamaterial is added to the front of the horn aperture, we found that the reflector antenna provides higher gains of approximately 26.60 dBi, 26.76 dBi, and 25.43 dBi at frequencies of 1,030 MHz, 1,090 MHz, and 1,300 MHz, respectively. Therefore, we can summarize that the offset-fed reflector antenna for the radar system with the hybrid metamaterial can increase the gain of each frequency by approximately 3 dB (3.29 dB, 3.2 dB, and 3.69 dB at 1,030 MHz, 1,090 MHz, and 1,300 MHz, respectively).

VI. Conclusion

We proposed the gain enhancement of the dual-band and dual-polarized asymmetric horn antenna for the secondary radar system using original horn from the DR-172 ADV radar system as a reference. The hybrid metamaterial structure was designed for placing at the front of the horn aperture to increase the gains of this asymmetric horn. The proposed architecture consists of two types of metamaterials structure: the woodpile EBG structure and wire medium work together with the origin-

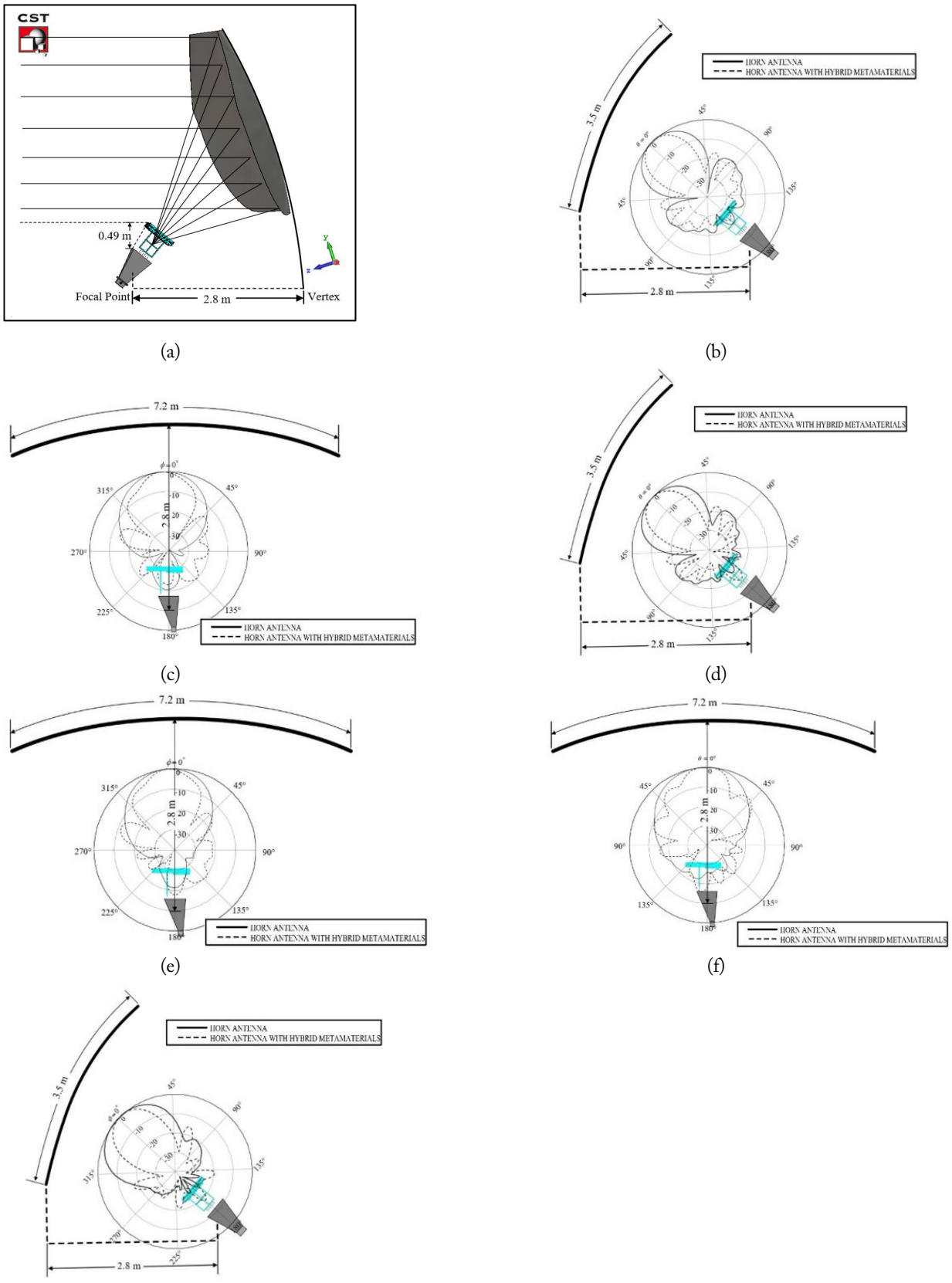

Fig. 19. Model and graphic images of the primary reflector with offset-fed asymmetric horn and hybrid metamaterial by exciting with the simulated far-field sources: (a) model of offset-fed reflector feed by the proposed feeder and (b–g) show excitation sources for the primary reflector in both planes at frequencies 1,030 MHz, 1,090 MHz, and 1,300 MHz. (a) Perspective view and (b, d, g) side views, and (c, e, f) top views.

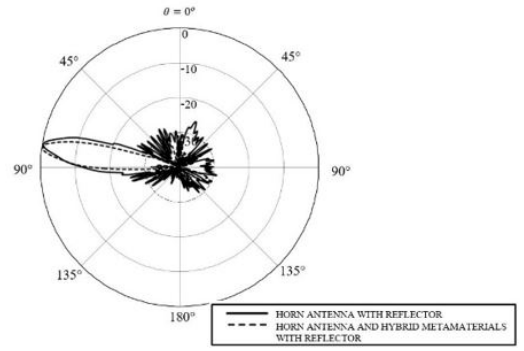

(a)

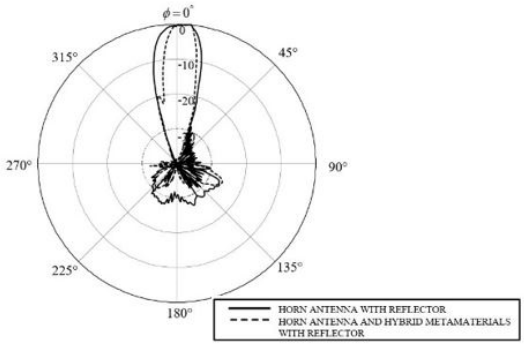

(b)

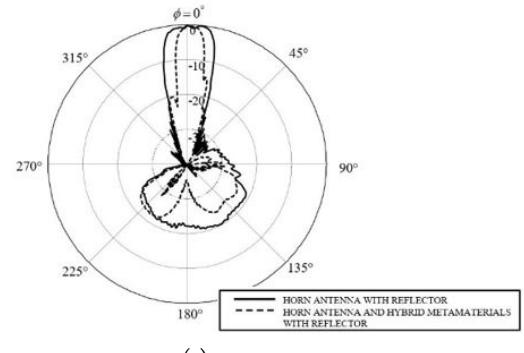

(c)

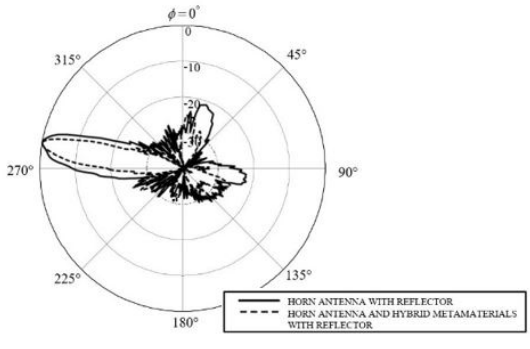

(d)

Fig. 20. Comparison of simulated radiation patterns of an offset-fed reflector antenna excited by an asymmetric horn without/with the hybrid metamaterial structure. (a) Elevation angle for E-plane of 1,060 MHz, (b) azimuthal angle for H-plane of 1,060 MHz, (c) azimuthal angle for E-plane of 1,300 MHz, and (d) elevation angle for H-plane of 1,300 MHz.

nal asymmetric horn. The gain enhancement of the target detection beam at the operating frequency of 1,300 MHz with horizontal polarization was achieved by using the property of the woodpile EBG structure. The wire medium structure improved the gain of the IFF beam at frequencies of 1,030 MHz (Tx) and 1,090 MHz (Rx), respectively, with vertical polarization. The simulated and measured results for the asymmetric horn without/with the proposed hybrid metamaterial structure, such as the gains, radiation patterns, and reflected power, were in good agreement. Importantly, the proposed hybrid metamaterial structure can improve the gains of both beams by slightly more than 3 dB and retain the direction of both beams with reference to the original beam directions obtained from the reference horn modelled.

This work was supported by the Research Department institute of Engineering, Suranaree University of Technology, Nakhonratchasima, Thailand.

REFERENCES

[1] B. Edde, *Radar: Principles, Technology, Applications*. Englewood Cliffs, NJ: Prentice Hall, 1993.

[2] Y. J. Lee, J. Yeo, R. Mittra, and W. S. Park, "Application of electromagnetic bandgap (EBG) superstrates with controllable defects for a class of patch antennas as spatial angular filters," *IEEE Transactions on Antennas and Propagation*, vol. 53, no. 1, pp. 224-235, 2005.

[3] F. Frezza, L. Pajewski, E. Piuzzi, C. Ponti, and G. Schettini, "Analysis and experimental characterization of an alumina woodpile-covered planar antenna," in *Proceedings of the 40th European Microwave Conference*, Paris, France, 2010, pp. 200-203.

[4] D. R. Smith, W. J. Padilla, D. C. Vier, S. C. Nemat-Nasser, and S. Schultz, "Composite medium with simultaneously negative permeability and permittivity," *Physical Review Letters*, vol. 84, no. 18, pp. 4184-4187, 2000.

[5] N. Fang and X. Zhang, "Imaging properties of a metamaterial superlens," in *Proceedings of the 2nd IEEE Conference on Nanotechnology*, Washington, DC, 2002, pp. 225-228.

[6] J. D. Joannopoulos, S. G. Johnson, J. N. Winn, and R. D. Meade, *Photonic Crystals: Molding the Flow of Light*. Princeton, NJ: Princeton University Press, 2008.

[7] A. R. Weily, L. Horvath, K. P. Esselle, B. C. Sanders, and T. S. Bird, "A planar resonator antenna based on a woodpile EBG material," *IEEE Transactions on Antennas and Propagation*, vol. 53, no. 1, pp. 216-223, 2005.

[8] Y. Lee, X. Lu, Y. Hao, S. Yang, J. R. Evans, and C. G. Parini, "Low-profile directive millimeter-wave antennas using free-

formed three-dimensional (3-D) electromagnetic bandgap structures," *IEEE Transactions on Antennas and Propagation*, vol. 57, no. 10, pp. 2893-2903, 2009.

[9] S. Kampeephat, P. Krachodnok, and R. Wongsan, "Gain improvement for conventional rectangular horn antenna with additional EBG structure," in *Proceedings of 2014 11th International Conference on Electrical Engineering/Electronics, Computer, Telecommunications and Information Technology (ECTI-CON)*, Nakhon Ratchasima, Thailand, 2014, pp. 1-4.

[10] R. Wongsan, P. Krachodnok, S. Kampeephat, P. Kamphikul, "Gain enhancement for conventional circular horn antenna by using EBG technique," in *Proceedings of 2015 12th International Conference on Electrical Engineering/Electronics, Computer, Telecommunications and Information Technology (ECTI-CON)*, Hua Hin, Thailand, 2015, pp. 1-4.

[11] P. Kamphikul and R. Wongsan, "Gain improvement for rectangular horn antenna by using curved-woodpile metamaterial," in *Proceedings of 2016 13th International Conference on Electrical Engineering/Electronics, Computer, Telecommunications and Information Technology (ECTI-CON)*, Chiang Mai, Thailand, 2016, pp. 1-4.

[12] P. Burghignoli, G. Lovat, F. Capolino, D. R. Jackson, and D. R. Wilton, "Directive leaky-wave radiation from a dipole source in a wire-medium slab," *IEEE Transactions on Antennas and Propagation*, vol. 56, no. 5, pp. 1329-1339, 2008.

[13] P. Burghignoli, G. Lovat, F. Capolino, D. R. Jackson, and D. R. Wilton, "Modal propagation and excitation on a wire-medium slab," *IEEE Transactions on Microwave Theory and Techniques*, vol. 56, no. 5, pp. 1112-1124, 2008.

[14] E. Forati and G. W. Hanson, "Scattering from isotropic connected wire medium metamaterials: three-, two-, and one-dimensional cases," *IEEE Transactions on Antennas and Propagation*, vol. 61, no. 7, pp. 3564-3574, 2013.

[15] A. Tomaz, J. J. Barroso, P. J. Castro, and A. J. F. Orlando, "Experimental investigation on the radiation pattern of a horn antenna loaded by a wire medium," in *Proceedings of 2013 IEEE Antennas and Propagation Society International Symposium (APSURSI)*, Orlando, FL, 2013, pp. 958-959.

[16] M. K. T. Al-Nuaimi, W. Hong, and Y. Zhang, "Design of high-directivity compact-size conical horn lens antenna," *IEEE Antennas and Wireless Propagation Letters*, vol. 13, pp. 467-470, 2014.

[17] P. Duangtang, P. Mesawad, and R. Wongsan, "Gain improvement of conical horn antennas by adding wire medium structure," in *Proceedings of 2016 13th International Conference on Electrical Engineering/Electronics, Computer, Telecommunications and Information Technology (ECTI-CON)*, Chiang Mai, Thailand, 2016, pp. 1-5.

[18] S. Kampeephat, P. Kamphikul, and R. Wongsan, "Gain improvement for conventional rectangular horn antenna with additional two-layer wire medium structure," in *Proceedings of 2017 Progress in Electromagnetics Research Symposium-Fall (PIERS-FALL)*, Singapore, 2017, pp. 2493-2497.

[19] D. J. Brain and A. W. Rudge, "Efficient satellite antennas," *Electronics and Power*, vol. 30, no. 1, pp. 51-56, 1984.

Peerasan Khamsalee

was born in Nakhonratchasima, Thailand, 1991. He earned his Bachelor of Engineering degree in Telecommunication Engineering from Suranaree University of Technology, Thailand, in 2013, as well as his Master of Engineering degree in Telecommunication Engineering at Suranaree University of Technology in 2015. He is currently working toward his doctorate in telecommunication engineering at Suranaree University of Technology. His research interests include electromagnetic theory, antenna engineering, and metamaterial technology.

Piyaporn Mesawad

received her Bachelor of Engineering degree in telecommunication engineering at Suranaree University of Technology, Thailand, in 1997, as well as her Master of Engineering degree in electrical engineering from Chulalongkorn University, Thailand, in 2001. She then received her Doctor of Engineering degree in telecommunication engineering at Suranaree University of Technology, Thailand, in 2008. She is a reviewer for the IEEE Conference. Her research interests are electromagnetic theory, antenna engineering, and the electromagnetic band gap. Associate Professor Dr. Piyaporn is a member of the Electrical Engineering/Electronic, Computer, Telecommunication, and Information Technology Association (ECTI) and the Institute of Electronics, Information, and Communication Engineers (IEICE).

Rangsan Wongsan

received his Bachelor of Engineering degree in electronics engineering at Rajamangala Institute of Technology (RIT) in 1989, as well as his Master of Engineering degree in electrical engineering from King Mongkut's Institute of Technology North Bangkok (KMITNB) in 1994. He then received his Doctor of Engineering degree in electrical engineering at King Mongkut's Institute of Technology Ladkrabang (KMITL) in 2003. He is currently a reviewer of many journals related to electromagnetic applications. His research focuses on antenna theory and electromagnetic applications. Currently, his research interests are the utilization of metamaterials for efficient improvement of conventional antennas and microwave devices. Associate Professor Dr. Rangsan is a member of the Electrical Engineering/Electronic, Computer, Telecommunication, and Information Technology Association (ECTI) and the Institute of Electronics, Information, and Communication Engineers (IEICE).

JEES Journal of
Electromagnetic Engineering and Science

Instructions for Authors

Journal of Electromagnetic Engineering and Science (*J. Electromagn. Eng. Sci*.; *JEES*) is an official English journal of the Korean Institute of Electromagnetic and Engineering Science (KIEES). The objective of *JEES* is to publish academic as well as industrial research results and foundings on electromagnetic engineering and science. The journal covers all aspects of researches and technology related to electromagnetics: Electromagnetic Compatibility/Electromagnetic Interference, Microwave and Millimeter-Wave Engineering, Antenna and Propagation, Electromagnetic Theory, Wireless Communication, Lightwave and Electro-Optics, Materials and Components, Software Defined Radar, Radar, Bioelectromagnetics, and etc.

I. Copyright and Creative Commons Attribution Licensing

The copyright and the transfer rights of the digital content of published papers and the journal is owned by the KIEES. All published materials are also assigned a Creative Commons Attribution License (http://creativecommons.org/licebses/by-nc/4.0/). The journal accepts manuscripts for consideration with the understanding that the manuscript has not been published previously and is not currently under consideration for publication elsewhere, and in addition, that the authors (or their employer, if it holds the copyright) are authorizing the transfer of the copyright to the Institute when the manuscript is submitted. Author should check the copyright transfer conditions and forms at http://www.jees.kr.

II. Research and Publication Ethics

Research published in *JEES* must have followed institutional, national, and international guidelines. For policies on research and publication ethics that are not stated in these instructions, please refer to the *Committee on Publication Ethics* (*COPE*) *Guidelines* (http://publicationethics.org/resources/code-conduct).

1. Originality and Duplicate Publication

A manuscript submitted for publication in *JEES* should be an original work with technical values. It must not have been previously published and is not under consideration for publication elsewhere. *JEES* assumes that the materials submitted for its publications are properly available for general dissemination for the readership of those publications. It is the responsibility of the authors, not *JEES*, to determine whether disclosure of their materials requires prior consent of other parties and, if so, to obtain it. If an author uses charts, photographs, or other graphics from any previously printed materials, he/she is responsible for obtaining written permissions from the publisher to use them in his/her manuscript. Responsibility for the contents of published papers rests upon the authors, not *JEES*.

2. Conflict of Interest

Authors are required to complete a declaration of conflict of interests. All conflict of interests that are declared will be listed at the end of published articles.

3. Authorship

Authorship should be restricted to those individuals who have met each of the following three criteria:
1) made a significant contribution to the conception and design of the project, or the analysis and interpretation of the data, or other substantial scholarly effort; 2) participated in drafting, reviewing and/or revising the work; and 3) approved the final version for publication. After the initial submission of a manuscript, any changes whatsoever in authorship (adding author(s), deleting author(s), or re-arranging the order of authors) must be explained by a letter to the editor from the authors concerned. The content of this

letter must be acknowledged and agreed upon by all of the authors of the paper.

If you accept the policies on research and publication issued by KIEES, authors must click the response of "The Code of Research Ethics" through online.

III. Submission of Manuscripts

Authors are expected to be members of the KIEES except for some special cases approved by the Editorial Board of KIEES. All manuscripts should be submitted electronically through the online submission and review site (https://mc03.manuscriptcentral.com/jees). For the first submission, you may be required to create an account on the submission site. A manuscript can be submitted at any time of the year. When submitting a manuscript, authors need to make sure that their manuscripts do not provide any of their identities such as authors' names and affiliations as the review is double-blinded. More detailed submission instruction is available in the upper right corner of the submission site. All manuscripts submitted to the Journal must comply with the instruction and the standard format of the Journal. Otherwise, it will result in return of the manuscript and possible delay in publication. For assistance, please contact us via e-mail (admin-jees@kiees.or.kr).

IV. Peer Review Process

The manuscript will be forwarded to three reviewers selected for their expertise in the field of the submitted manuscript. The acceptance criteria for all papers are based on the quality and originality of the research and its clinical and scientific significance. During the review process, the author is often asked to expand, rewrite, or clearly explain the specific contents of his/her paper. It is not uncommon that an author is asked to provide another draft with the suggested changes for further review. A revised manuscript should be submitted to the homepage within a month from the date on which any change of the manuscript is requested to the author. Once a manuscript has received the final approval of the reviewers and Editor-in-Chief, the author will be notified and asked to prepare the manuscript for final publication and to possibly complete an additional information form.

V. Publication Type

The papers are classified into five categories.

Regular Paper should be an original work that contributes to the academic interests of the KIEES members with technical values. The paper should also be written within 12 pages with A4 size including figures, charts, and tables (The main body of text consists of two columns).

Letter consists of reports of preliminary results or short reports on completed work that are of current interest to many researchers in the field. Comments on material previously published in the journal, suggestions for new directions, and errata could be included. Their length must be less than 3 pages (with a two-column format) including paper title, author affiliation, reference, etc.

Review Paper will be published by direct submission as well as from invited experts. In both cases, the work will be subject to editorial review. Review papers should critically review topics not only to inform the reader of the background, but also to communicate the state of the art and outstanding research problems.

Technical Report is on innovative technical achievements of interest to the community and usually a report of an extensive series of measurements. Report is often involving display in the form of tables or graphs, with text describing the conditions and procedures of measurement.

Editorial is a brief report of research findings adequate for the journal's scope and of particular interest to the community.

VI. Manuscript Preparation

All manuscripts must be written in MS-Word and adhere to the following guidelines:

1. A cover of each paper manuscript should include a title, authors' names (main author and co-authors), author's organizations, contact information (e-mail and phone number), and the author's area of expertise.
2. The first page of a main text should only contain title, abstract with a length of about 150 words, and key words with around five words.
3. The contents of the manuscript should be arranged in the order of abstract, main text, acknowledgments, references, and appendix.
4. The numbers corresponding to chapters in the manuscript should be written in Roman numerals (I, II, III, IV...) and the numbers corresponding to sections should be written in Arabic numerals (1, 2, 3, 4...).
5. Equation numbers should be given in Arabic numerals enclosed in parentheses on the right-hand margin. They should be cited in the text as, for example Eq. (1) or Eqs. (1)-(3).
6. All tables should be numbered consecutively with Arabic numerals. They should be referred to in the text and should be numbered according to their order of mention in the text. In addition, all tables should, not only list all abbreviations in the table in footnotes at the end, but also have a title that is concise and describes the table's contents. Vertical lines are not used. The table should be self-explanatory and supplement, not duplicate, the text. If the table or any data therein have been published, a footnote to the table must give permission information to the original source. The structure should be clear, with simple column headings giving all units. A table should not exceed one page when printed. Use lowercase letters in superscripts $^{a,b,c...}$ for special remarks.
7. All figures should be of high quality meeting with the publishing requirement with legible symbols and legends. In preparing the figures, authors should consider a size reduction during the printing process to have acceptable line clarity and character sizes. Use only figures that are necessary to illustrate the meaning of the text. Figures must be black and white of high contrast. All figures should be referred to in the text as, for example, Fig. 1, Fig. 2(a), or Figs. 1-3.
8. Only those references cited in the text should be listed in the references. Authors are responsible for the accuracy and completeness of their references and the correct text citations. In the text the reference should be numbered in bracket in ascending order (e.g., [1, 3], or [4-6]; Lee [2] and Kim and Park [5]; Jang et al. [7]). In case of the paper title, only the first letter is to be capitalized. However, in case of journal and book titles, the first letter of each word should be capitalized and all of the letters should be italicized. See the example below.

Books

[1] F. Giannini and G. Leuzzi, *Nonlinear Microwave Circuit Design.* NewYork, NY: John Wiley & Sons Inc., 2004.

Journals

[2] H. Ahn and B. Kim, "Equivalent transmission-line sections for very high impedances and their application to branch-line hybrids with very weak coupling power," *Journal of Electromagnetic Engineering and Science*, vol. 9, no. 2, pp. 85-97, Jun. 2009.

Report

[3] E. E. Reber, R. L. Michell, and C. J. Carter, "Oxygen absorption in the earth's atmosphere," Aerospace Corp., Los Angeles, CA, Tech. Rep. TR-0200 (4230-46)-3, Nov. 1988.

Conference Proceedings

[4] S. P. Bingulac, "On the compatibility of adaptive controllers," in *Proceedings of the 4th Annual Allerton Conference on Circuit and System Theory*, NewYork, pp. 8-16, 1994.

Papers Presented at Conferences

[5] J. G. Kreifeldt, "An analysis of surface-detected EMG as an amplitude-modulated noise," presented at the 8th International Conference on Medical and Biological Engineering, Chicago, IL, 1969.

[6] J. Arrillaga and B. Giessner, "Limitation of short-circuit levels by means of HVDC links," presented at the IEEE Summer Power Meeting, Los Angeles, CA, Jul. 1990.

Theses (M.S.) and Dissertations (Ph.D.)

[7] N. Kawasaki, "Parametric study of thermal and chemical nonequilibrium nozzle flow," M.S. thesis, Department of Electronic Engineering, Osaka University, Osaka, Japan, 1993.

[8] J. O. Williams, "Narrow-band analyzer," Ph.D. dissertation, Department of Electronic Engineering, Harvard University, Cambridge, MA, 1993.

Standards

[9] *IEEE Criteria for Class IE Electric Systems*, IEEE Standard 308, 1969.

Online Sources

[10] R. Bartle, "Early MUD History," Nov. 1990; www.ludd.luth.se/aber/mud-history.html.

9. When citing any paper published in JEES, it should be indicated the name of the journal as *Journal of Electromagnetic Engineering and Science* or *J. Electromagn. Eng. Sci*.

10. Acknowledgment, if needed, appears before the reference. Sponsorship or financial support acknowledgment should be included here.

11. Unit and Abbreviation:If the authors describe length, height, weight, and volume, they should use standard metric units. Temperature should be given in degrees Celsius. All other units should follow the International System of Units (SI). All units must be preceded by one space except percentages (%) and temperatures (°C).

Abbreviations must be used as an aid to the reader, rather than as a convenience of the author, and therefore their use should be limited. Generally, abbreviations that are used less than 3 times in the text, including tables and figure legends, should be avoided. Standard SI abbreviations are recommended. Other common abbreviations are as follows (the same abbreviations are used for plural forms): h (hour), min (minute), s (second), d (day), wk (week), mo (month), y (year), L (liter), mL (milliliter), μL (microliter), g (gram), kg (kilogram), mg (milligram), μg (microgram), ng (nanogram), pg (picogram), *g* (gravity; not g), nm (nanometer), μm (micrometer), mV (millivolt), mA (milliampere), mW (milliwatt), C (coulomb), μF (microfarad), mH (millihenry), n (samplesize), SD (standard deviation of the mean), and SE (standard error of the mean).

VII. Accepted Manuscript

Once the review process has been completed with a decision of acceptance, the final manuscript accommodating all of the reviewers' comments should be submitted along with photos of the authors and their brief biographies (including major research areas). The accepted papers will be published, in principle, in the order of initially submitted dates subject to decision of the Editorial Board.

1. Page Proofs

Authors will be given an opportunity to review the laser printed version of their manuscripts before printing. One set of page proofs in PDF format will be sent by e-mail to the corresponding author. The review should be solely dedicated to detecting typographical errors.

2. Publishing Charge

The publishing charge for general publishing is KRW 150,000 (US$150) for up to the first 6 pages. For 7 to 8 pages, an extra charge of KRW 30,000 (US$30) per page, and for 9 pages or more, an extra charge of KRW 40,000 (US$40) per page. Furthermore, the KIEES charges extra KRW 100,000 (US$100) for the paper acknowledging a financial support from an institution, in addition to the above mentioned page charge. Twenty reprints without a cover will be supplied without an additional charge.

Contact Us

Editorial office of the Korean Institute of Electromagnetic Engineering and Science
217, Saechang-ro, Yongsan-gu, Seoul, 04376, Korea
Tel: +82-2-337-9666/332-9665 Fax: +82-2-6390-7550
http://www.jees.kr, E-mail: admin-jees@kiees.or.kr

Wireless Power Week 2020

WPTC

IEEE PELS Workshop on Emerging Technologies: Wireless Power 2020

IEEE MTT-S Wireless Power Transfer Conference 2020

AirFuel™ Alliance

AirFuel Developers Forum

Nov 15 – 19, 2020

Seoul, Korea

wpw2020.org

Call for Participation

Pre-registration due on Aug 16, 2020

Keynote Speakers

Naoki Shinohara
Kyoto University

Jenshan Lin
Univ. of Florida

Joungho Kim
KAIST

Chris Mi
San Diego State University

Ron Hui
The U. of Hong Kong/ Imperial College London

Sanjay Gupta,
President,
AirFuel Alliance

IEEE

pels IEEE POWER ELECTRONICS SOCIETY Powering a Sustainable Future

MTT-S®

KIEES Korean Institute of Electromagnetic Engineering and Science

LIG Nex1

TELEDYNE LECROY Everywhereyoulook™

DYMSTEC

η electronics

RFHIC

HIOKI

EMAG TECH

KOREA TOURISM ORGANIZATION www.visitkorea.or.kr

SEOUL METROPOLITAN GOVERNMENT

JEES Journal of Electromagnetic Engineering and Science

pISSN : 2671 - 7255 / eISSN : 2671 - 7263
http://www.jees.kr
SCOPUS Journal
SCIE Journal

Call for Paper

JEES, a quartely journal in English, is published by the Korean Institute of Electromagnetic Engineering and Science. It currently registered with the National Research Foundation of Korea and also indexed in Scopus, CrossRef, EBSCO, DOI/Crosref, Google Scholar, and Web of Science Core Collection as Science Citation Index Expanded(SCIE) Journal.

The objective of JEES is to publish academic as well as industrial research results and discoveries in electromagnetic engineering and science. We look forward your submisiion in JEES.

Topics

- Antennas
- Passive Components and Circuits
- Active Devices and Device Modeling
- RF/Wireless Systems and Applications
- Electromagnetic Interference/Compativility/Environment
- Other areas

Sub - Topics :

- Antennas : Planar (mictostrip antenna etc.)
- Antennas : 3-Dimnesional
- Passive circuits and components : filters / other than filters
- Active circuits and componets: amplifiers / mixers and oscillators
- Wireless communication theory and systems
- Communication signal processing
- Radio resource management and policy
- Electromagnetic wave absorbing material
- Electromagnetic field theory and numerical analysis
- Electromagnetic wave scattering and imaging
- Radar and system appliciations

Submission Information :

- Online Site : www.jees.kr (E-SUBMISSION : https://mc03.manuscriptcentral.com/jees)
- Type of manuscripts : Regular Paper, Letter, Invited Paper

Editorial Office :

- #706 Totoo Valley, 217 Saechang-ro, Yongsan-gu, Seoul 04376, Korea
- Tel : +82-2-337-9666 Fax: : +82-2-6390-7550
- E-mail : admin-jees@kiees.or.kr

KIEES Korean Institute of Electromagnetic Engineering and Science

AUTHOR CHECKLIST

Title : _____

General

☐ This paper has not been and will not be published in any other journal.

☐ This paper follows the format of the KIEES paper submission guideline, is less than 12 pages long, including figures and tables (3 pages for a letter), and has a two-column layout.

☐ This paper includes a cover page, an abstract, keywords, main text, appendix, and references in the correct order. Each page has a consecutive page number.

Cover page

☐ The cover page includes the title, authors, affiliation of all authors, identifier of the corresponding author, and provides contact information for the corresponding author (phone number, e-mail address, and mobile number).

Abstract and key words

☐ An abstract is provided and is less than 500 words long.

☐ Fewer than 5 keywords are provided.

Main text

☐ The reference number is written next to the quote.

☐ The chapter numbers are written in Roman numerals (I, II, III, IV…) and subheading numbers are written in Arabic numerals (1, 2, 3, 4…).

References

☐ Sufficient Korean as well as international literature is referenced in the paper.

☐ Only the references used in the main text are included in the reference list and these are numbered according to their order of appearance.

☐ All reference citations follow the correct format indicated in the submission regulations.

Figures and tables

☐ For the figures and tables, the first letter of the very first word is capitalized.

☐ All figure legends include both a title and a detailed explanation to help in understanding what the figure depicts.

☐ All tables are self-explanatory and do not repeat the content from figures or sources included in the main text.

* Check each box after confirming that the statement is true.

The authors of this paper have confirmed the above items, following the paper submission regulations of *the Korean Institute of Electromagnetic Engineering and Science (KIEES)*, and are requesting publication of this paper.

_____/_____/ 2020

Representative author: _____ (signature)

Journal of Electromagnetic Engineering and Science

http://www.jees.kr

JEES
Volume 20, Number 3,
July, 2020

REGULAR PAPERS